Department of Physics and Astronomy

University of Heidelberg

Diploma thesis

in Physics

submitted by

Victoria E. Wagner

born in Darmstadt

2012

Investigation of Pulse Shape Performance

of the First

GERDA Phase II Detectors

This diploma thesis has been carried out by Victoria E. Wagner

at the

Max-Planck-Institut für Kernphysik

under the supervision of

Prof. Manfred Lindner

Pulsformstudien der ersten GERDA Phase II Detektoren:

Das GERDA Experiment sucht nach dem neutrinolosen doppelten Betazerfall. Broad Energy Germanium (BEGe) Dioden wurden als neues Detektor-konzept für Phase II des Experimentes gewählt, um die Sensitivität durch zusätzliche Masse sowie verbesserte Energieauflösung und Pulsform-Diskriminierungs-Eigenschaften (PSD) zu erhöhen.

Im Rahmen der Diodencharakterisierung im Vakuumkryostaten wurden die PSD Effizienzen der Detektoren bestimmt. Zwei der Detektoren zeigten dabei eine Diskriminierungseffizienz von $5.4\,\%$ in der Einzel-Escape-Linie (SEP) der ^{208}Tl-Linie bei $2.6\,$MeV, welche vorwiegend aus Ereignissen mit mehrfacher Energiedeposition (MSE) besteht. Fünf der neuen Detektoren zeigten jedoch mit $10.5\,\%$ eine niedrigere Effizienz im SEP. Um die Verschlechterung der PSD besser zu verstehen, wurden detaillierte Oberflächenscans mit ^{241}Am durchgeführt. Darin wurde eine verstärkte Positionsabhängigkeit des Pulsformparamters Amplitude-zu-Energie für Dioden mit niedrigerer PSD festgestellt. Dies sowie weitere Untersuchungen führen zu dem Schluss, dass die Pulsform teilweise durch Oberflächeneffekte beeinflusst wird.

Zum Schluss wurden fünf der neuen Dioden in den GERDA Flüssig-Argon-Tank eingebaut. Die Detektoren zeigen allgemein eine gute Leistung. Mit ihnen ist es möglich Untergrund von MSE γ-Ereignissen, sowie Betateilchen von ^{42}K und Alphateilchen von ^{210}Po zu unterdrücken. Für vier Dioden wurde in einem Energiefenster um den Interessensbereich (2039 ± 400) keV ein vorläufiger Untergrundindex (BI) bestimmt. Durch Anwendung der Pulsformanalyse sinkt der BI zu $(0.089 - 3.544) \cdot 10^{-2} \frac{Ereignisse}{kg \cdot yr \cdot keV}$. Dies liegt im angestrebten BI von $10^{-3} \frac{Ereignisse}{kg \cdot yr \cdot keV}$ für GERDA Phase II.

Investigation of Pulse Shape Performance of the First GERDA Phase II Detectors:

Broad Energy Germanium diodes (BEGe) enriched in ^{76}Ge have been selected as the new detector design for the Phase II of the neutrinoless double beta decay experiment GERDA. These diodes will improve the sensitivity of the experiment by additional target mass, an improved energy resolution and enhanced pulse shape discrimination (PSD) properties. The PSD efficiencies of the new enriched BEGe detectors were studied in vacuum cryostat in the framework of the diode characterization. Two of them showed a survival probability of $5.4\,\%$ for events of the single escape peak (SEP) of the ^{208}Tl γ-line at $2.6\,$MeV which consists mainly of multi-site events. However, five BEGe diodes showed lower PSD efficiencies around $10.5\,\%$ in the SEP. For a deeper understanding of the deteriorated PSD detailed ^{241}Am surface scans were performed. They showed unexpectedly high position-dependence of the pulse shape parameter Amplitude-over-Energy for the five diodes with lower PSD efficiency. This and further investigation indicate that the PSD is partly influenced by surface effects.

Finally, five of the enriched BEGe diodes were installed in the GERDA liquid argon cryostat. They show a good performance and are able to reject efficiently multi-site γ-events as well as β-particles from ^{42}Ar and α-particles from ^{210}Po. A preliminary background index (BI) for four enriched BEGe diodes in the energy region of interest at (2039 ± 400) keV is deduced. With applied PSD cuts the BI becomes $(0.089 - 3.544) \cdot 10^{-2} \frac{counts}{kg \cdot yr \cdot keV}$ which is within the design specifications of $10^{-3} \frac{counts}{kg \cdot yr \cdot keV}$ of GERDA Phase II.

Contents

Chapter 1

Introduction

Neutrinos are one of the most interesting elementary particles. Yet, their characteristics are not fully understood as they imply new physics beyond the Standard Model. Therefore, neutrinos are a current subject of research in elementary particle physics.

Neutrino physics   In 1930 W. Pauli introduced a neutral particle in order to conserve energy and momentum in the beta decay. Later, E. Fermi gave the hypothetical particle the name "neutrino". However it took about 26 years until the discovery of the first neutrino.

In the last five decades neutrinos have been studied carefully for their characteristics. The Standard Model of Particle Physics describes neutrinos as mass-less neutral leptons, thus elementary particles which underlie the weak force only. Three different neutrino flavor exist: electron-, muon- and tau-neutrinos. They are identified by the charged lepton they interact with. The Standard Model requires the conservation of the total lepton number and the lepton flavor number.

In 1970 the Homestake Chlorine Detector measured less solar neutrinos than predicted by Standard Model calculations: The so-called "solar neutrino problem" was the first hint that the description of neutrinos in the Standard Model was incomplete. Later experiments confirm the observation of a reduced solar neutrino flux. The solution to the puzzle was "lepton flavor oscillation". Electron neutrinos released in the fusion process in the sun change their flavor while traveling to the earth. The SNO experiment was sensitive to all neutrino flavors and confirmed that the net neutrino flux is as predicted. This, among many other neutrino experiments including atmospheric and reactor neutrinos, confirmed the neutrino flavor oscillation. Neutrino flavor oscillation is only possible if neutrinos have masses. Therefore, the oscillation implies already that two assumptions in the Standard Model concerning neutrinos are incorrect: Flavor lepton number is violated and neutrinos are not mass-less.

Investigation of the neutrino flavor oscillation casts light on the neutrino mixing and the mass separation of neutrinos, but not on the absolute mass of neutrinos. Furthermore, experiments dedicated to neutrino oscillation are not able to determine the exact mechanism of how neutrinos obtain mass.

1.1 The Neutrinoless Double Beta Decay and the GERDA Experiment

The **GER**manium **D**etector **A**rray (GERDA) experiment searches for the lepton number violating neutrinoless double beta $(0\nu\beta\beta)$decay [Col04].

1.1.1 Experimental Approach to the Neutrinoless Double Beta Decay

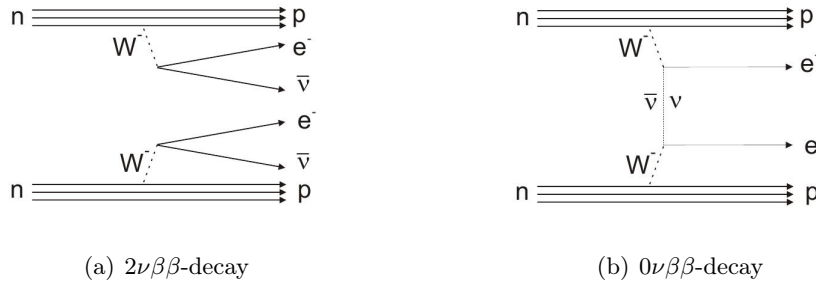(a) $2\nu\beta\beta$-decay   (b) $0\nu\beta\beta$-decay

Figure 1.1: Feynman diagram of the two neutrino double beta $(2\nu\beta\beta)$ decay and the neutrinoless double beta $(0\nu\beta\beta)$ decay

A regular beta decay is is described by

$$(A, Z) \rightarrow (A, Z + 1) + e^- + \bar{\nu}_e \ , \tag{1.1}$$

whereas A is the mass number and Z the charge of the decaying nucleus.
Some nuclei cannot decay as described in Equation (1.1) as the binding energy of the daughter nucleus, $(A, Z + 1)$, is higher than the binding energy of the parent nucleus, (A, Z). However, the nuclei might disintegrate into $(A, Z + 2)$ by the simultaneous decay of two nucleons. The so-called two neutrino double beta decay $(2\nu\beta\beta)$ is described by

$$(A, Z) \rightarrow (A, Z + 2) + 2e^- + 2\bar{\nu}_e \ . \tag{1.2}$$

The corresponding Feynman diagram is shown in Figure 1.1 (a). So far the $2\nu\beta\beta$ decay has been detected in about ten isotopes with half-lives typically of $10^{19} - 10^{21}$ yr [Bar11].
In neutrinoless double beta decay $(0\nu\beta\beta)$

$$(A, Z) \rightarrow (A, Z + 2) + 2e^- \ , \tag{1.3}$$

no neutrinos are present in the final state. In the standard interpretation, this decay process is realized by light massive left-handed Majorana neutrinos. In the following this simplest case of the Majorana nature is considered only[1]. Figure 1.1 (b) shows the Feynman diagram of the $0\nu\beta\beta$. As the neutrino is identical to its antiparticle, the one antineutrino emitted in beta-decay is absorbed as an neutrino by the other nucleus disintegrating via inverse beta decay.
The discovery of the $0\nu\beta\beta$ would

---

[1]For further reading of alternative processes of the neutrinoless double beta decay see [Rod11]

- prove lepton number (L) violation: The initial state has no leptons, the final state has two electrons $\rightarrow \Delta L = 2$

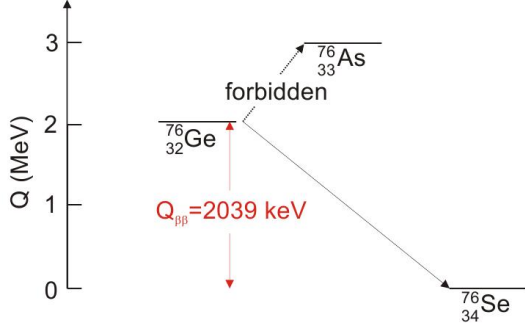- measure the effective Majorana neutrino mass [2]

- access the "hierarchy problem" [2]

Figure 1.2: Decay scheme of ^{76}Ge into ^{76}Se
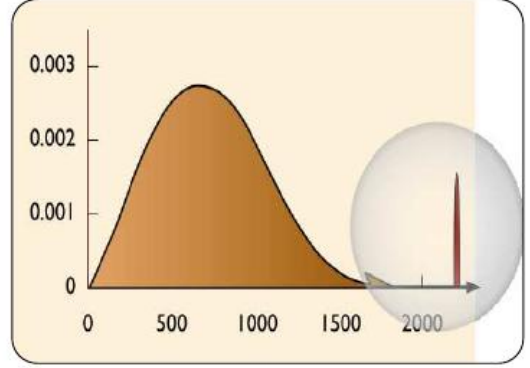
Figure 1.3: Schematic spectrum of the double beta decay with enlarged region of the $0\nu\beta\beta$-peak at $Q_{\beta\beta}$

A possible candidate isotope for neutrinoless double beta decay is ^{76}Ge. Figure 1.2 shows the decay scheme of ^{76}Ge into ^{76}Se. The Q value of the process, i.e. the total amount of energy released in the decay process, is 2039 keV.

Figure 1.3 shows the spectrum of the double beta decay: The $2\nu\beta\beta$-decay has a typical β-spectrum. In the $0\nu\beta\beta$ decay the total energy of the process is carried by the two electrons in the final state. Thus, assuming $0\nu\beta\beta$ exists, a peak at the $Q_{\beta\beta}$ value, i.e. 2039 keV, is present. Experiments searching for the $0\nu\beta\beta$ aim for a signal which is naturally small in comparison to background signals. The neutrinoless double beta decay is a second order process and even rarer than the two neutrino double beta decay. Therefore, even larger half-lives are expected for $0\nu\beta\beta$ than those found for the $2\nu\beta\beta$-decays. The signal is given by the decay rate, which in turn is determined by the half-life $T_{1/2}$: With increasing $T_{1/2}$, the rate and thus the signal decreases.

In the presence of background the sensitivity of the lower limit of the half life scales as

$$T_{1/2} \propto \epsilon a \sqrt{\frac{Mt}{BI\Delta(E)}} \tag{1.4}$$

whereas,

- ϵ is the detection efficiency

- a is the abundance of the isotope under investigation for the ($0\nu\beta\beta$)

- M is the mass $[kg]$

---

[2]we assume the Majorana nature of neutrinos.

- t is the exposure time $[yr]$

- BI is the background index $[\frac{counts}{keV \cdot kg \cdot yr}]$

- $\Delta(E)$ is the energy resolution in the region of interest (ROI) $[keV]$

In order to reach the experimental goal, a very low background, a high energy resolution, a long exposure time, a high mass and a high detection efficiency are aimed for.

Recent Limits on the $T_{1/2}$ of $0\nu\beta\beta$

So far the best limits on the half-life of the neutrinoless double beta decay are obtained by the Heidelberg-Moscow (HdM) experiment. The collaboration determined the lower limit on $T_{1/2}$ of the $0\nu\beta\beta$ of ^{76}Ge to $>1.9 \cdot 10^{25}\, yr$ at 90 % C.L. with a background index of $\sim 0.11\, \frac{counts}{keV \cdot kg \cdot yr}$ and a total exposure of $71.1\, kg \cdot yr$ [KKea01].

Part of the HdM collaboration claims for a $4.2\,\sigma$ evidence of the $0\nu\beta\beta$-decay [KKea04]. However, the result is hotly disputed and need to be clarified by several independent experiments [Aea02a].

1.1.2 Status of the GERDA Experiment
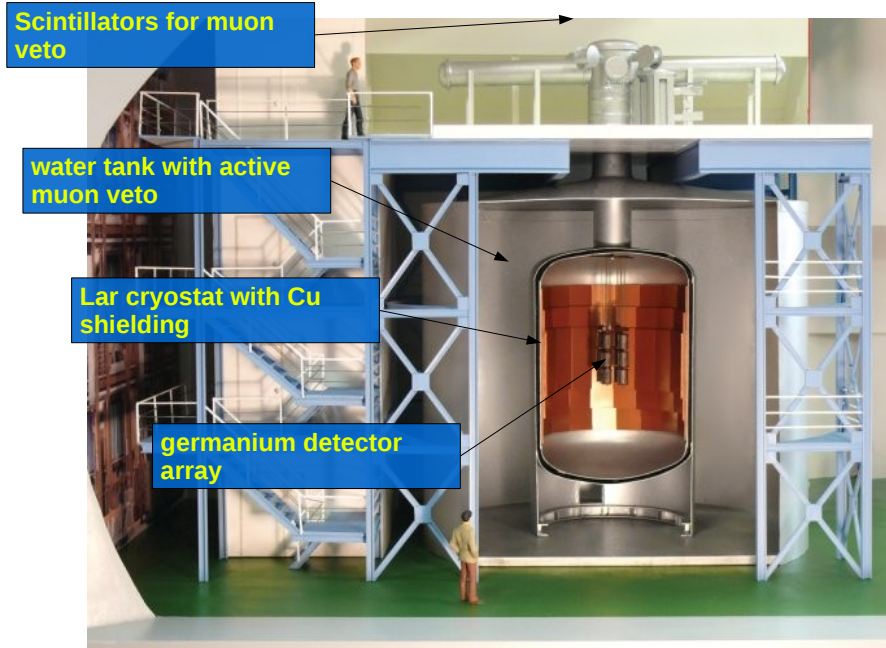
Figure 1.4: An artist model of the GERDA experiment

The GERDA experiment [Col04] was designed to probe the neutrinoless double beta decay in ^{76}Ge with a sensitivity up to $T_{1/2} >2 \cdot 10^{26}\, yr$ and scrutinize the claim of evidence of the observed $0\nu\beta\beta$ decay in [KKea04].

The collaboration chose to build the experiment as an array of germanium detectors isotopically enriched in ^{76}Ge, i.e. to search for the intrinsic $0\nu\beta\beta$ decay within the germanium detectors themselves. This way, the detectors serve simultaneously as source and the efficiency

ϵ in Equation (1.4) is maximized. Furthermore, germanium detectors have an excellent energy resolution. Moreover, the germanium crystals can be isotopically enriched in ^{76}Ge.

The GERDA Setup

The GERDA experiment (Figure 1.4) aims to reduce any background, external and internal, especially in the region of interest (ROI) at the $Q_{\beta\beta}$ value of ^{76}Ge, 2039 keV. Most dangerous for the identification of the $0\nu\beta\beta$ signal are decays with Q values above 2039 keV as they can deposit energy in the ROI, thus might mimic a $0\nu\beta\beta$ decay.

The experiment is located in the Laboratori Nazionali del Gran Sasso (LNGS). The experimental site holds a shielding against cosmic radiation itself with 3500 m w.e. which reduces the muon flux by six orders of magnitudes with respect to the Earth's surface. The muon-induced neutron flux is negligible in GERDA.

The germanium detectors are well shielded by a passive shielding. However, each material introduced into the vicinity of the detectors for shielding is an additional radioactive source. Therefore, all built-in materials of the experiment must be of low activity and screened prior to the installation.

The detector array is operated in a liquid argon (LAr) cryostat. The cryogenic liquid serves simultaneously as cooling medium and as passive shielding against α- and β-particles as well as γ-rays from the surrounding material. The cryostat has an additional internal copper shielding for further external background suppression. The LAr cryostat is embedded in a water tank which moderates and absorbs neutrons.

To complement the passive shielding, active background suppression techniques are applied. Muons in GERDA are detected by the water cherenkov detector as well by plastic scintillators on the top.

Preparations are ongoing, to use the LAr as scintillation medium for active background suppression of γ-rays (see Phase II description in this Section). Furthermore, background identification by enhanced pulse shape analysis discrimination techniques will be applied to the data acquired.

Intrinsic Contamination of the Ge Diodes

Besides the background from cosmic radiation and the surrounding material, the germanium diodes can hold an intrinsic contamination themselves [Hei09]. Above ground, e.g. during transport and detector production, the germanium can be activated cosmogenically. The most important process is the spallation of nuclei by high energetic neutrons which produce ^{68}Ge or ^{60}Co. ^{60}Co can deposit energy in the ROI via the summation of its two γ-rays with a total Q value of 2.5 MeV. ^{68}Ge disintegrates via electron capture into ^{68}Ga which decays by positron emission or electron capture into ^{68}Zn. The Q value of ^{68}Ga is 2.9 MeV, i.e. above $Q_{\beta\beta}$.

Therefore, it is important to keep the exposure of the germanium crystals to cosmic radiation minimal. The most efficient shielding against high energetic neutrons is an overburden of solid rock. The detectors, and the germanium they are made of respectively, is stored underground at any time possible.

GERDA Phase I

The GERDA physics data taking will take place in two phases. In November, 2011, the
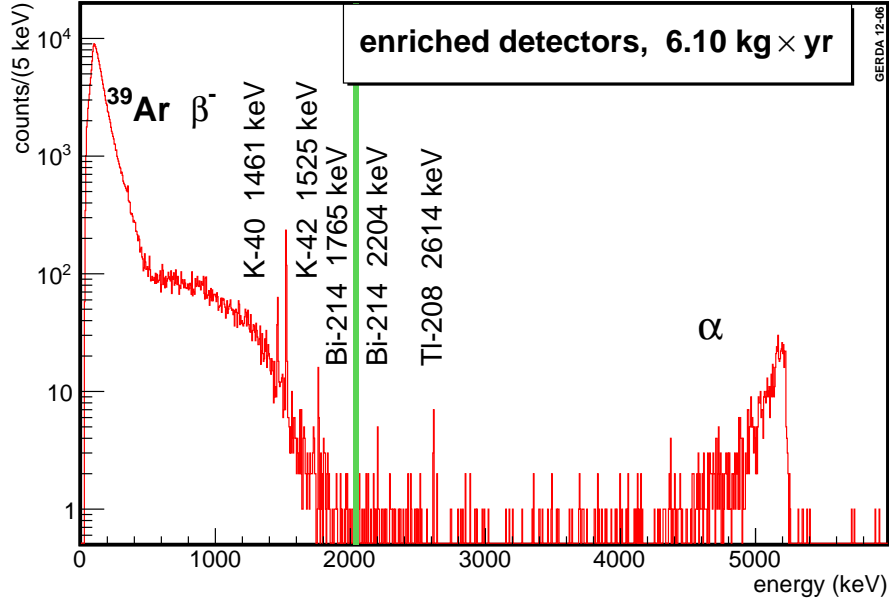
Figure 1.5: Spectrum measured with enriched germanium detectors in Phase I. The main background contributions are ^{39}Ar, ^{40}K, ^{42}K, ^{214}Bi, ^{208}Tl and α-particles from ^{210}Po. Data in the region (2039±20) keV are blinded, marked in green.

GERDA Phase I physics data taking started with about 18 kg of coaxial germanium detectors previously used in the HdM [KKea01] and IGEX [Aea02b] experiments. The detectors are isotopically enriched to 86 % in ^{76}Ge. In addition, detectors with a natural abundance of ^{76}Ge from the Genius TF R&D program [Bea00] are used in GERDA.

The main goal of Phase I [Col04] is to give a statistically unambiguous statement concerning the observation of of the neutrinoless double beta decay claimed by [KKea04].

Furthermore, Phase I is used to establish the quality cuts on the data acquired in GERDA. In order to chose the cuts independently from the $0\nu\beta\beta$ signal, the region (2039±20) keV is blinded, i.e. events in this region are not available for analysis. The data will be unblinded in spring 2013 (the end of Phase I).

Figure 1.5 shows the energy spectrum measured with enriched germanium detectors in GERDA Phase I. The main background contribution is:

1. ^{39}Ar, a beta source with a Q value around 0.565 MeV, thus does no contribute to the background in the ROI

2. ^{42}Ar which decays into ^{42}K. ^{42}K decays under beta particle emission into ^{42}Ca. The decay is identified by the γ-line observed at 1524.7 keV which might occur with the beta decay. The Q value of the ^{42}K decay is 3525.4 keV

3. ^{214}Bi which originates from ^{222}Rn has a γ-line at 2204 keV. Thus, the ROI lies within the Compton region of this line.

4. ^{208}Tl out of the thorium decay chain which has a γ-line at 2614 keV. Thus, the ROI lies within the Compton region of this line.

5. α-particles from the ^{210}Po decay, which has a Q value of 5.3 MeV.

The average background index in the region of (2039 ± 100) keV minus the blinded 40 keV region is

$$BI = 0.020^{+0.006}_{-0.004} \frac{counts}{keV \cdot kg \cdot yr} \tag{1.5}$$

The design value for GERDA Phase I, $BI = 0.01 \frac{counts}{keV \cdot kg \cdot yr}$, is almost reached and already better than a factor of 5 compared to the background index achieved in HdM.

GERDA Phase II Preparations

While data are acquired in Phase I, the preparations of GERDA Phase II are ongoing. Phase II aims to probe the $0\nu\beta\beta$ decay of ^{76}Ge up to a sensitivity of $T_{1/2} > 2 \cdot 10^{26}$ yr. This will be achieved by

- increasing the target mass by additional 20 kg of germanium enriched to 86 % in ^{76}Ge

- an enhanced energy resolution of the new detectors in comparison to Phase I detectors (coaxial HPGe detectors)

- reducing the background index to $\lesssim 0.001 \frac{counts}{keV \cdot kg \cdot yr}$ with

  - enhanced pulse shape discrimination properties to identify background events (see Section 1.2)

  - anticompton veto by collecting scintillation light produced in LAr by background events

The final design for the LAr instrumentation is still under discussion.

The new detectors for Phase II are being currently produced. The germanium used for production of the Phase II diodes was isotopically enriched to 86 % in ^{76}Ge by the Electrochemical Plant in Zelenogorsk in Krasnoyarsk, Russia. The crystals were grown by Canberra Industries Inc. in Oak Ridge, USA. Afterward, the germanium slices were shipped to Europe and transformed into working detectors by Canberra Semiconductor NV in Olen, Belgium.
The production of the new enriched diodes was divided into two parts: First, in December 2011 seven slices out of two grown crystals were cut and sent to Canberra in Belgium for the production of seven diodes in vacuum cryostats. Afterward the detectors were fully characterized in the HADES underground laboratory in Mol, Belgium (see Section 2.1.5) giving acceptable results. Than, the second and longer production phase of new enriched diodes started. The crystal production in Canberra, Oak Ridge was completed in July, 2012. The production of 23 new diodes started in Belgium the end of August, 2012, and are currently characterized in HADES as well. The production and characterization is still ongoing and scheduled to be finished by December 2012.
In order to test the reliability of the new diodes in LAr and to find possible surface contamination, five of the seven new diodes were installed into the GERDA cryostat in July, 2012.
The installation of Phase II is planned to start in spring 2013 when the physics data taking of Phase I is complete.

1.2 Broad Energy Germanium (BEGe) Detectors

Broad **E**nergy **Ge**rmanium (BEGe) detectors, as they are commercially available from the semiconductor manufacturer Canberra, were selected for the GERDA Phase II detector design. These high purity germanium (HPGe) detector type owes its name to its excellent energy resolution in a large energy range, from 3 keV to 3 MeV [Inc12]. Furthermore, the diode has a special geometry that allows for enhanced discrimination of events with single or multiple energy deposition within the crystal. As a consequence, an active background technique can be applied off-line to the recorded data in order to discriminate background events depositing energy in several sites (so-called multiple-site events – MSE) from single-site events (SSE), such as $0\nu\beta\beta/2\nu\beta\beta$-events.

The following description of the basic principles of a germanium detector are partly borrowed from [Kno89]. See the reference for further details.

1.2.1 Basic Principle of Semiconductor Detectors

Semiconductors are characterized by their small band gap between the energy of the valence and the conduction band. In the case of germanium the size of the band gap is 0.67 eV. The energy necessary for an electron to migrate from the valence band to the conduction band can be gained by sufficient thermal energy or by adding energy via interaction of ionizing radiation.

If an electron is excited into the conduction band, a vacancy in the valence band is left behind - a *hole* - which represents a net positive charge. As the electron in the conduction band and the hole in the valance band occur as a pair they are called an *electron-hole pair*.

p-type Semiconductors

P-type semiconductors have predominantly holes as free charge carriers, it is said that the holes are the majority charge carriers. This state can be achieved e.g. by doping the material , i.e. by introducing impurities such as boron atoms into the germanium crystal. Bo atoms have one fewer valence electron compared to the surrounding germanium. Therefore, one covalent bond is left unsaturated, representing a hole. As an electron filling the vacancy in the crystal is slightly less bound than an electron participating in a covalent bond of two germanium atoms, the vacancies create energy levels within the forbidden energy gap close to the valence band.

This additional energy level within the band gap is filled by electrons via thermal excitation. As the energy level is always occupied by electrons from the usual covalent bonds of the germanium atoms, holes are left behind. The filled additional band in the band gap represents fixed negative charges, whereas the holes are the free charge carriers dominating the conductivity of the material. Electrons are the minority charge carriers in the p-type material.

Respectively, in n-type semiconductors, electrons are the dominating free charges and holes the minority charge carriers.

p-n Junction

In order to read out an electron-hole pair created in interaction with ionizing radiation as a signal, an electrical potential difference must be applied that attracts the charges. Furthermore, to prevent fluctuations in the electric current that might overpower the signal itself,

all free charge carriers have to be removed from the detector material. This is achieved most efficiently by creating a p-n junction.

If p-type and n-type semiconducting material is in contact (= a diode) the free negative charges from the n-type diffuse into the p-type material. Thus, the conduction electrons are captured by the holes in the p-type material, whereas in the n-type material ionized impurities are left behind. Consequently, a positive space charge is created in the n-type material, a negative space charge in the p-type material, respectively. The built-up electric field prevents further charges to diffuse. The region devoid of free charge carriers is called *depletion region*.

By applying a positive HV to the n-type material, the potential difference which builds up near the p-n junction is enhanced. This is called a reverse bias. Consequently, the width of the depleted region can be made significantly larger.

Highly doped material is signed n^+- or p^+-type. This layer shows a very high conductivity. In order to extend the depletion region much further into one side of the junction, a combination of highly doped and less-doped material is used. E.g. considering a p-n^+ junction: Due to the higher concentration of free electrons in the n^+ layer, the electrons tend to diffuse a larger distance into the p-type material.

Depletion of High Purity Germanium (HPGe) Diodes

The *depletion region* or *active volume* is the volume sensitive to ionizing radiation. It's thickness d is described by

$$d \propto \left(\frac{V}{eN} \right)^{1/2} \tag{1.6}$$

whereas V is the applied reversed bias and N the impurity concentration of the less-doped junction side. Equation 1.6 implies that the thickness of the depletion region increases with decreasing impurity concentration. In order to reach the order of several centimeters of depletion thickness – which is needed for γ-spectroscopy – the impurity concentration of the material needs to be as low as 10^{10} atoms/cm^3. Germanium detectors with such a reduced impurity concentration are called high-purity germanium (HPGe) detectors.

1.2.2 HPGe Diodes as Radiation Detectors

The energy to create an electron-hole pair in germanium is 2.96 eV. γ-rays emitted in radioactive decays have typical energies between several hundred keV and a few MeV. Thus, the amount of charge carriers produced in germanium by γ-ray interaction is high. More charge carriers in the signal means enhanced energy resolution: The signal to background ratio enhances, and the statistical fluctuations (which is given by the square root of the number of charge carriers) decreases in comparison to the total number of charge carriers in the signal. Therefore, HPGe diodes are very suitable for γ-spectroscopy.

Leakage Current

When applying a reverse bias voltage the minority charge carriers (e.g. in p-type material the electrons) will cause a steady-state current. However, this contribution is small. In addition, the thermal production of electron-hole pairs, i.e. of free charge carriers in the depleted region, causes a significant leakage current. Due to the small band gap of germanium, the Ge detectors can only be operated at cryogenic temperatures. Therefore, germanium detectors are usually

operated in vacuum cryostats which are in thermal contact to a liquid nitrogen bath (at 77 K) which is kept insulated in a dewar.

Furthermore, surface leakage currents can occur. They appear at places of large voltage gradients, namely the edges of the junction. Contamination of the surface enhances the production of surface leakage current.

Fluctuations in the leakage current can lead to noise, thus influences the energy resolution wherefore the leakage current of a detector is currently monitored during its operation as a change in leakage current usually indicates a change in the detector performance.

Gamma-ray Interaction in Germanium
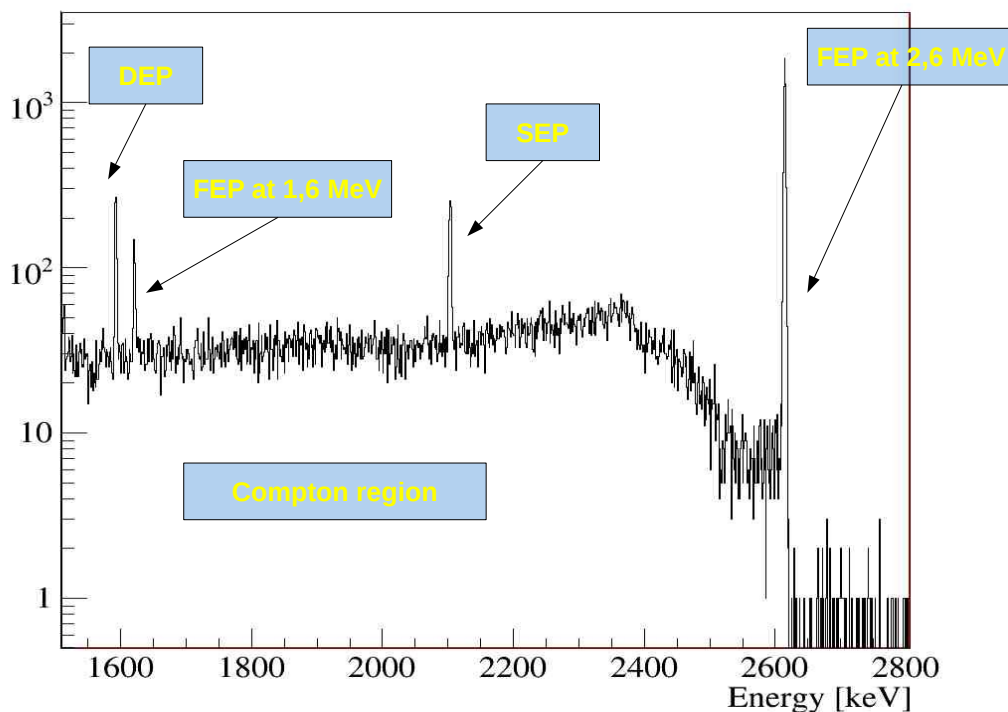
Figure 1.6: A typical γ-spectrum measured with a ^{228}Th source. The spectrum is dominated by the decay of the daughter nuclide ^{208}Tl which has a strong γ-line at 2614.5 keV. The single escape peak (SEP) as well as the double escape peak (DEP) of the 2614.5 keV-line are shown.

In the interaction of ionizing radiation with a germanium detector, fast electrons are created which in turn loose their energy via ionization and excitation of the atoms of the detector material, or the emission of bremsstrahlung. The main interaction mechanisms of γ-rays with matter are

1. photoelectric absorption: The incident γ-ray transfers its entire energy to an electron of the detector material. The process is dominant at γ-energies up to a few hundred keV.

2. Compton scattering: The incident γ-ray is scattered at an electron, only part of the

energy is transferred.

3. pair production: The incident γ-ray is converted into an electron-positron pair. The minimum γ-ray energy is 1.02 MeV.

Consequently, γ-rays can interact at multiple-sites within the detector until they are fully absorbed or escape the detector.

Figure 1.6 shows the γ-spectrum of a ^{228}Th source. The daughter nuclide ^{208}Tl has a strong γ-line at 2614.5 keV which dominates the shown spectrum. The full energy peak consists of γ-rays that are completely absorbed within the detector whereas in the Compton region γ-rays are represented that translate only a fraction of their energy to the detector. The ratio of events in the Compton continuum to FEP depends on the detector geometry (and size) and the source position.

If the incident γ-ray has enough energy, an electron-positron pair can be produced. After thermalization the positron annihilates with an electron of the detector material into two photons, each with an energy 511 keV. The annihilation photons can undergo further Compton scattering and/or photoelectric absorption until their energy is completely transferred to the electrons of the detector's material. However, one of the annihilation photons might escape the detector, resulting in a single escape peak (SEP) at an energy of 511 keV below the full energy peak. If both annihilation photons escape a double escape peak (DEP) is seen 1022 keV below the full energy peak.

The Electrical Signal

The charge Q induced by a charge carrier q in the active detector volume at the read-out electrode is described by the Shockley-Ramo theorem [He01]:

$$Q = -q \cdot W(x) \tag{1.7}$$

$W(x)$ is the so-called *weighting potential* for the charge q at the position x. The weighting potential is equal to the electric potential at the position x if

- the read-out electrode is at unitary potential, i.e. $W = 1$,

- all other electrodes are at zero potential, i.e. $W = 0$ and

- all space charges are removed from the diode.

Equation 1.7 describe the signal development as an electrostatic problem. The movement of the charge cluster, created in an interaction of ionizing radiation with the detector, move along the electric field inside the diode. Consequently, the induced charge Q, i.e. the read-out signal, variates in time.

The signal development in time, i.e. the pulse shape, is given by the weighting potential $W(x)$. The signal increases as the charge cluster reaches a position of strong weighting potential within the diode. By requiring $W = 0$ at all electrodes except for the signal read-out, only the charges collected at the read-out electrode contribute to Q.

With increasing position-dependence of the weighting potential the resolution of the development of the signal in time increases. This is the principle of the pulse shape discrimination: Events with multiple energy deposition in the diode show a different development of the signal in time compared to single energy deposition.

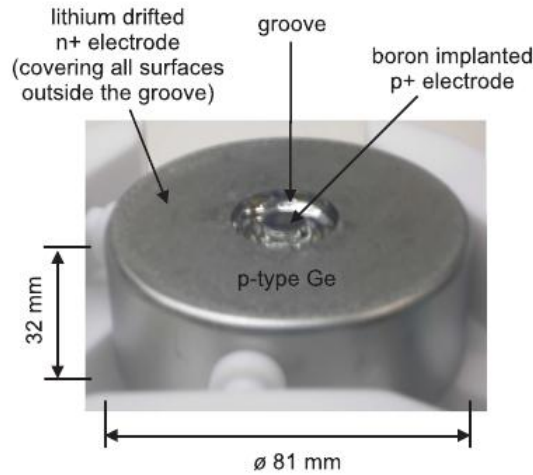### 1.2.3 BEGe's as the GERDA Phase II Detectors

Figure 1.7: Picture of a BEGe detector, taken from [Hea10]

Figure 1.7 shows a *Broad Energy Germanium* (BEGe) detector: It is a standard p-type HPGe detector. The surface is a Li diffused n^+ electrode except for the boron implanted p^+ contact on one of the flat surface where the signal is read-out. The electrical contacts are separated by a circular groove. When the detector is operated in vacuum cryostat, the groove is passivated with GeO_2 in order to prevent leakage current. Positive high voltage is applied to the n^+ electrode for reverse biasing.

The read-out electrode is small-sized which

- enhances pulse shape discrimination by a strongly position-dependent weighting potential,

- improves energy resolution by its lower capacitance, thus lower noise, and

- lowers the energy threshold.

The Dead Layer

At operational bias voltage the "active volume" of the detector corresponds to the depleted region between the n^+ and p^+-contact of the detector (see Figure 1.7). Most of the electrons in the n^+ contact remain in the conduction band, thus the anode forms a "dead layer" which is insensitive to any ionizing radiation depositing energy. For a BEGe type detector, the typical dead layer thickness is about 0.5 mm. As the range of α-particles in germanium is $\sim 2\,\mu m$, α-particles, partly β-particles (with a range of ~ 1 mm) and low energy γ-rays below 3 keV are absorbed by the dead layer.

Thus, for GERDA the dead layer represents a shielding against possible surface contamination of the detector.

Slow Pulses

The border between active and dead volume of the detector is not strictly sharp, a "transition layer" is in-between [Sal12] where the detector is not completely insensitive to interaction.

The electric field is zero inside this "transition layer", wherefore charge carriers created in this region slowly diffuse instead of drifting directly towards the read-out electrode. This leads to charge losses and the signal will rise significantly slower than signals generated by events in the active volume. The deeper the event happens inside this "transition layer" the longer the rise time of the pulse and the larger the energy loss.

The Electric Field
In Reference [Aea11b] the internal electric field was calculated in order to simulate the pulse
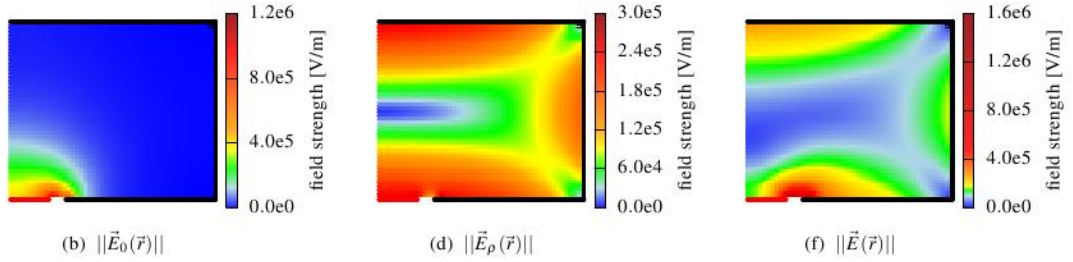

Figure 1.8: The electric field strength created by the electrode potential only, $\vec{E}_0(\vec{r})$, (left) and the space charges in the active detector volume , $\vec{E}_\rho(\vec{r})$, (middle). The resulting total electrical field strength by the superposition of both contributions is shown on the right. Each picture shows half a vertical slice cut through the middle of the detector. Extracted from [Aea11b].

shapes generated in the active volume of a BEGe detector. The following discussion is derived from this article.

The internal electrical field $\vec{E}$ can be understood as a superposition of the potential created by the space charge distributions in the active volume, $\vec{E}_\rho$, and the electric field generated by the electrode potential only, $\vec{E}_0$:

$$\vec{E}(\vec{r}) = \vec{E}_0(\vec{r}) + \vec{E}_\rho(\vec{r}) \tag{1.8}$$

The simulated electric field strength is shown in Figure 1.8:

1. The electric field created by the electrodes only, $\vec{E}_0$, is weak in the detector but in the vicinity of the small read-out electrode

2. whereas $\vec{E}_\rho$ is strongest at the surface and weak in the middle slice of the diode

The resulting internal electrical field $\vec{E}(\vec{r})$ is shown on the right in Figure 1.8. As the charge clusters follow the electrical field, the holes are collected in the middle slice of the detector, mainly by the contribution from $\vec{E}_\rho$, and finally funneled towards the read-out electrode by $\vec{E}_0$. This is addressed as the "Funneling Effect" in the following sections. Figure 1.10(a) shows exemplarily the resulting trajectory of such charge clusters.

The signal induced at the read-out electrode by the charge carriers in active detector volume is described by Equation (1.7). Figure 1.10 shows the corresponding weighting potential from the calculation of a BEGe detector done in [Aea11b]: The weighting potential is weak but in
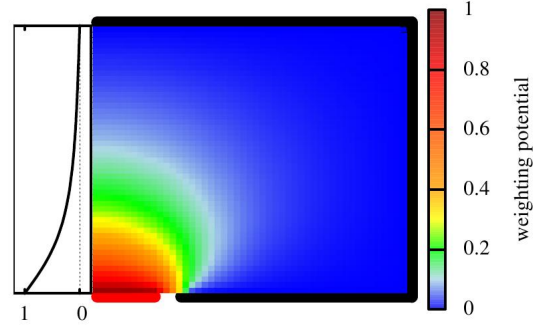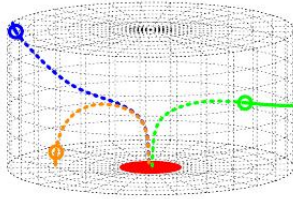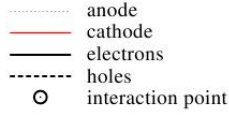
Figure 1.9: Simulated trajectories of charge carriers starting from different positions inside the bulk of the diode to the read-out electrode (red) [Aea11b].

Figure 1.10: Weighting potential of half a vertical slice cut through the middle of the detector [Aea11b].
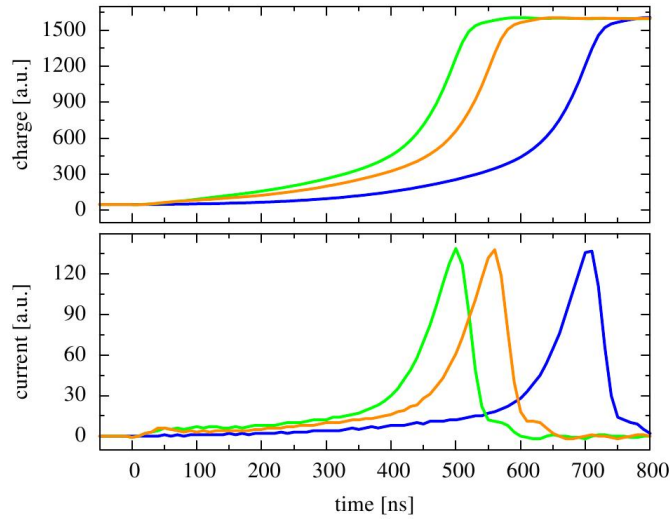
Figure 1.11: The pulse shapes corresponding to the trajectories in Figure 1.10. The top picture shows the charge pulse, the bottom picture the corresponding current pulse – i.e. the differential of the charge pulse.[Aea11b]

the vicinity of the read-out electrode.

Figure 1.11 shows the corresponding charge pulses induced at the read-out electrode: The signal stays compatibly flat until the charge carriers drift through the region of strong weighting which is seen as the sharp rising edge in the pulse.

As the charge carriers are collected in the middle plane of the detector, they drift along similar paths in the strong weighting potential. Therefore, the rising edges of the pulses, i.e. the dominant part, are similar. Pulses originating at different positions are shifted in time due to differently long drift paths through the crystal.

1.3 Pulse Shape Discrimination Method
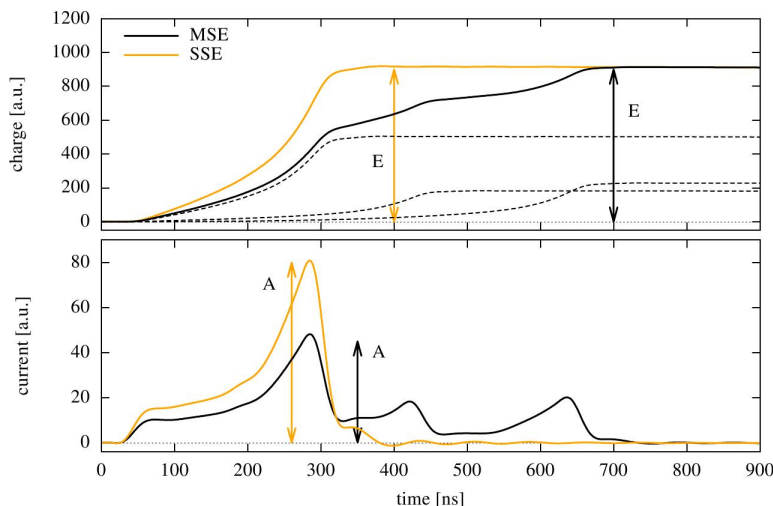
Figure 1.12: Typical signal created by a single- and multi-site event [Aea11b]

Figure 1.12 shows a typical signal generate by a single-site event (SSE) compared to a multiple-site (MSE) event in a BEGe type detector. The pulse shapes of single-site events (SSE) are very similar, apart from a shift in time of the rising edge of the pulse according to longer or shorter distances of the energy deposition to the read-out electrode. The charge clusters created in MSE arrive most likely time-displaced at strong weighting potential, which is seen in the structure of the rising edge of the pulse.

1.3.1 The A/E Analysis

For the pulse shape discrimination (PSD) of MSE and SSE, the ratio of the amplitude of the current signal A and the energy E, i.e. A/E, turned out to be an excellent parameter[Bud09]. Figure 1.12 compares the charge (top) and current (bottom) signal of an SSE and an MSE. Both events deposit the same energy within the crystal. However, the A values are different for MSE and SSE. According to the discussion about pulse shapes in Section 1.2.2, pulses of SSE in the bulk of the detector have similar pulse shape and consequently similar A/E values. In MSE, the energy is transferred to several smaller charge clusters that arrive separated in time at the read-out electrode. Therefore, the MSE has a smaller maximum amplitude of the current signal (thus smaller A/E). Furthermore, the current signal shows more than one peak, as in principle each charge cluster induces such a current peak at its arrival in the strong weighting potential.

The A/E cut is determined in pulse shape analysis (PSA) of a ^{228}Th spectrum. The ^{228}Th daughter nuclide ^{208}Tl has a γ-line of strong intensity at 2614.5 keV which has a high probability to interact via pair-production in the germanium crystal. Furthermore, the annihilation photons created in the positron annihilation, are likely to escape the detection in the crystal. Thus, the ^{228}Th spectrum shows a prominent DEP and SEP.
Figure 1.13(a) shows the A/E distribution vs energy of a ^{228}Th measurement:

(a)　　　　　　　　　　　　　　(b)
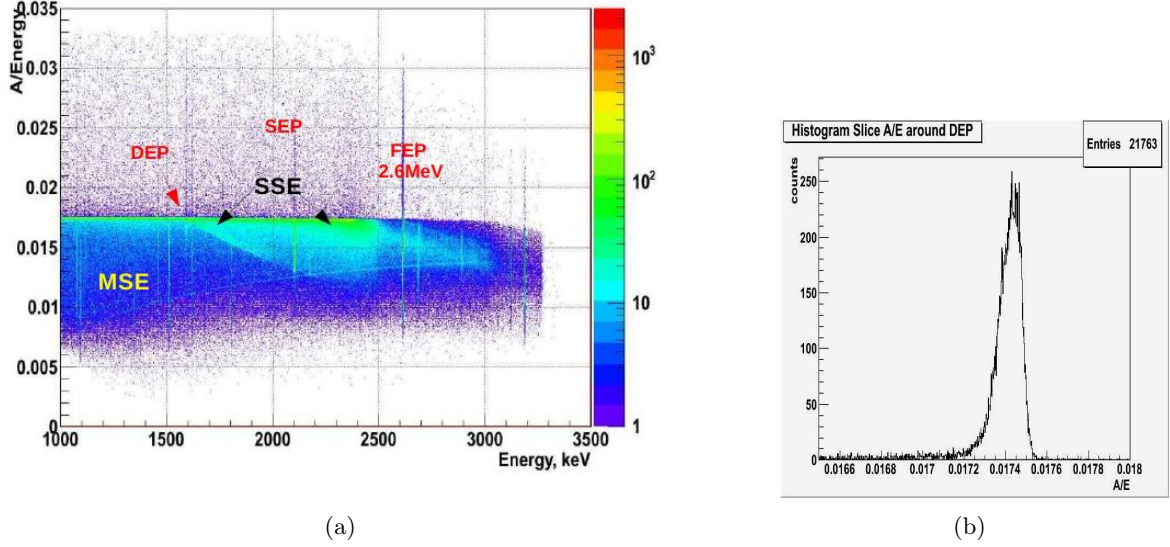
Figure 1.13: A/E vs energy and A/E distribution in the DEP measured with a depleted prototype BEGe, ^{depl}DD, in the Low Level Laboratory (LLL) at MPIK, Heidelberg

- SSE are located on a horizontal line, called the SSE-line

- MSE are found below the SSE-line

- the DEP, containing a large fraction of SSE, shows a high density of A/E values at the SSE-line

In Figure 1.13(b) the profile of the A/E distribution in the DEP region of the 2614 keV γ-line. SSE events are assumed to be Gaussian distributed, whereas MSE events produce a tail towards lower A/E values. The same assumption (Gaussian function plus tail) holds for the Compton regions as well.

The SSE-line is slightly energy dependent. This dependence can be approximated at high energies (above 1 MeV) by a linear function. In order to determine the slope of the SSE-line the A/E distribution in different Compton regions is fitted. The mean A/E value of the Gaussian function represents the SSE-line. The shape of the SSE-line is then determined by fitting the mean values of the single Compton regions with a linear function

$$m = a_{SSE} \cdot E - b_{SSE} \qquad (1.9)$$

where a_{SSE} is the slope of the SSE line and b_{SSE} the offset respectively.

The same energy dependence as for the SSE-line is expected for the cut. The A/E cut is represented by the linear function

$$c(E) = a_{SSE} \cdot E - b_{cut} \qquad (1.10)$$

whereas a_{SSE} is the slope in Equation (1.9) and b_{cut} is the A/E cut value. The cut is usually chosen such that 90 % of the events remain in the DEP, it is said "the A/E cut at 90 % acceptance in the DEP". All events with a specific energy E and $A/E < c(E)$ are rejected.
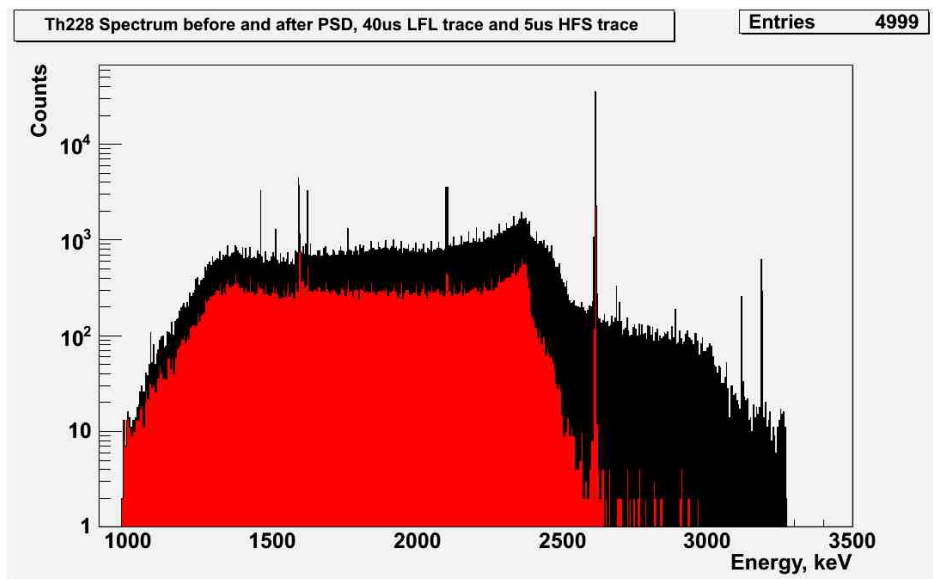
Figure 1.14: ^{228}Th spectrum with and without PSD cut acquired with the ^{depl}DD BEGe detector in the Low Level Laboratory of the MPIK

1.3.2 Application of the PSD Cut in Vacuum Cryostat

Figure 1.14 shows a ^{228}Th spectrum with and without PSD cut acquired with the prototype BEGe detector (called DD) in the Low Level Laboratory (LLL) of the MPIK in preparation of the HEROICA project (see Chapter 2.1.5). The black spectrum is without, the red spectrum with applied PSD cut. A clear reduction of the spectrum is achieved.

Table 1.1 summarizes the fraction of events that remain after the A/E cut, which is called the pulse shape discrimination (PSD) efficiency, in different energy regions:

1. In the DEP the acceptance of SSE DEP is $(90.0 \pm 2.7)\,\%$.

2. The SEP of the 2.6 MeV peak – which contains mostly MSE events – is suppressed to $(5.4 \pm 1.3)\,\%$.

3. The FEP 1.6 MeV and 2.6 MeV are suppressed by more than a factor 10

4. The average discrimination efficiency in two different-sized Compton regions around the $Q_{\beta\beta}$ value of ^{76}Ge, at 2039 keV, is $(36.7\pm3.5)\,\%$

In Table 1.1 two uncertainties are given: A statistical uncertainty simply calculated by the statistical fluctuation of the number of events before and after the cut. The second additional statistical uncertainty takes into account fluctuations in the A/E cut due to insufficient statistics in the DEP. In the example shown in Table 1.1 the acceptance in the DEP is 0.900 ± 0.027. The additional statistical uncertainty is given by the mean difference of PSD efficiencies in the specified energy regions if the acceptance fluctuates by $\pm\ 0.027$ in the DEP [Bud12a]. For small fluctuations in the DEP acceptance the estimation is satisfactory. However, for very low statistics, the uncertainties obtained by this method are overestimated.

Energy region	PSD efficiency
DEP of the 2.6 MeV peak	0.900 ± 0.027
FEP 1.6 MeV	$0.094 \pm 0.012 \pm 0.008$
SEP of the 2.6 MeV peak	$0.054 \pm 0.007 \pm 0.005$
FEP 2.6 MeV	$0.065 \pm 0.001 \pm 0.009$
2004-2074 keV	$0.367 \pm 0.007 \pm 0.028$
1989-2089 keV	$0.366 \pm 0.006 \pm 0.028$

Table 1.1: Pulse shape discrimination efficiencies obtained by the A/E cut applied to a ^{228}Th measurement with a prototype BEGe detector ^{depl}DD at LLL, MPIK. The first uncertainty takes into account the statistical fluctuation of the number of events, the second uncertainty takes into account fluctuations in the A/E cut due to low statistics in the DEP
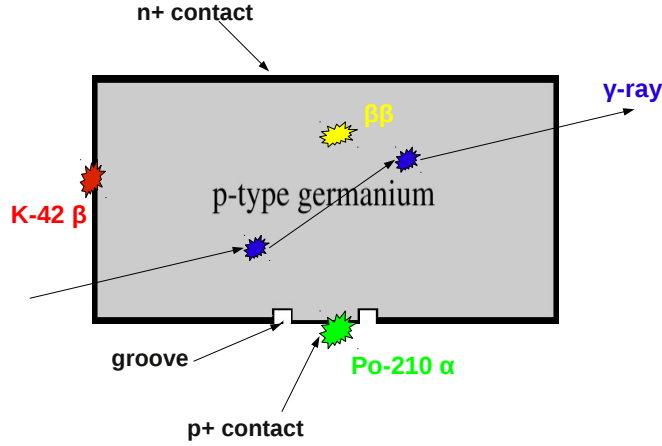
Figure 1.15: Schematic drawing of the main background contribution in GERDA interacting with a BEGe diode

1.3.3 Application of the PSD Cut in LAr Cryostat

In Section 1.1.2 the main background contribution in GERDA was introduced.

Figure 1.15 shows a simplified model of the different background interaction with the detector as well as the signal of the (neutrinoless) double beta decay.

Due to their short range in germanium, the two electrons released in the double beta decay of ^{76}Ge are SSE.

If a γ-ray interacts only once with the crystal the event has the same topology as an event from double beta decay, thus is not rejected by the PSD cut. However, if the γ-ray interacts with the detector via multiple Compton scattering the event is can be rejected by the A/E cut.

Since the diodes in GERDA are operated in LAr, β-particles might reach the n^+-surface [Bud12b]. As pointed out in Section 1.2.3, such n^+ surface events produce slow pulses, thus show a significantly lower A/E value. Consequently, such events can be rejected by the PSD cut as well.

α-particle cannot penetrate the dead layer of the crystal but might enter the diode through the region of the p^+-contact [Bud12b]. In interaction very to the read-out electrode, both electrons and holes are created in strong weighting potential, thus, contribute both to the signal. Thus, the signal rises sharply from the very beginning and such events near the p^+-contact have high A/E values. In order to reject events from the p^+ contact the A/E cut in Equation (1.10), $c(E)$, is mirrored at the SSE-line from Equation (1.9). All events with A/E values higher than this p^+-contact cut, are rejected.

Furthermore, the A/E is able to reject background event from cosmogenic activation which produces ^{60}Co or ^{68}Ge [Bud09]. ^{60}Co might deposit energy only by the sum of two γ-rays that are detected simultaneously, thus such events are highly multi-site. The ^{68}Ge decays into ^{68}Ga, which in turn is a β^+ emitter. The positron annihilates with an electron of the detector material into two photons. Therefore, the positron is detected by the energy deposited by the two annihilation photons which is a clear MSE.

The A/E cut based on pulse shape analysis is a very promising active background suppression technique for BEGe detectors.

1.4 Aim of this Work

This diploma thesis is written in the framework of the preparation for GERDA Phase II. The aim is to compare the enhanced pulse shape discrimination properties of the newly produced enriched BEGe detectors and non-enriched prototypes.

The pulse shape performance of the first seven enriched Phase II BEGe detectors was determined within the HEROICA project at HADES underground laboratory (Section 2.1.5) and is presented in Section 3.1.

Two enriched diodes were further tested in the Germanium Detector Laboratory (GDL) at LNGS for investigation of the pulse shape performance in LAr with removed passivation layer. The results are presented in Section 3.2.1.

Five diodes were installed in the GERDA LAr cryostat for testing their performance. The result of the PSA performance in comparison to the results obtained in the framework of the HEROICA project are discussed in Section 3.2.2.

Finally, the pulse shape cut was determined for the first month of data taking with the five enriched BEGe detectors in GERDA. To show the improvement in background suppression obtained by pulse shape analysis, a preliminary background index for the five BEGe detectors with and without applied pulse shape discrimination is deduced in Section 3.2.3.

The Experimental Setup

2.1 BEGe Characterization: The HEROICA Project

The **H**ades **E**xperimental **R**esearch **O**f **I**ntrinsic **C**rystal **A**ppliances [And12], HEROICA, project is dedicated to carry out a full characterization of the enriched BEGe detectors before they will be installed into the GERDA cryostat. In addition, the HEROICA project provides a unique possibility for a close study of a large number of BEGe detectors.
The project is run by the BEGe acceptance test team within the GERDA Collaboration. About 30 people are involved in the installation and maintenance of the infrastructure in the HEROICA site and the characterization of the enriched BEGe detectors.

2.1.1 The Location: HADES Underground Laboratory

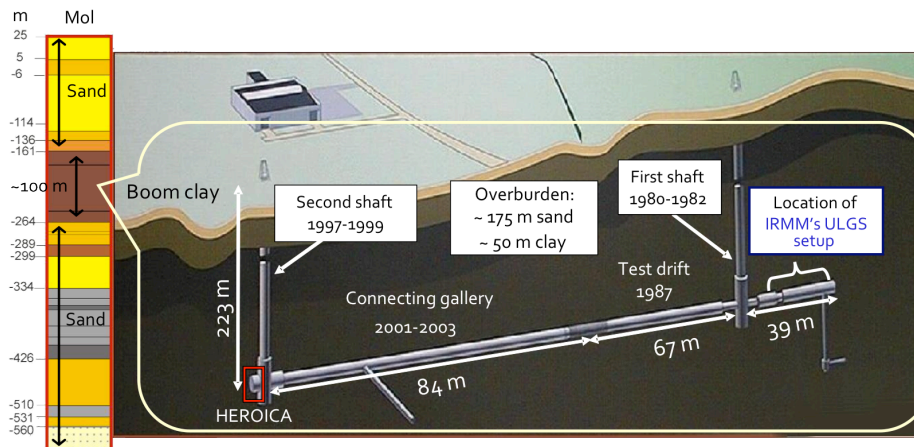**Figure 2.1:** Drawing of HADES underground laboratory. The HEROICA experimental site is located next to the second shaft on the left side in the drawing.

The HEROICA experimental site is located in the HADES (High Activity Disposal Experimental Site) underground laboratory at the Belgium Nuclear Research Center SCK-CEN in Mol, Belgium. The laboratory is situated 223 m underground in a boom clay layer which

corresponds to about $500\,\text{m}$ w.e. This reduces the muon flux by a factor of about 10^4 with respect to the Earth's surface.

The HADES laboratory in Mol is located about $30\,\text{km}$ from the diode manufacturer Canberra Semiconductor NV, Olen, Belgium. The close location of the laboratory to the manufacturer ensures that the diodes can be stored underground during the diode production phase. As pointed out in Section 1.1.2, it is important to keep the exposure to cosmic radiation minimal, in order to prevent the intrinsic contamination of the germanium by ^{68}Ge or ^{60}Co.

2.1.2 The First Seven Enriched BEGe Detectors
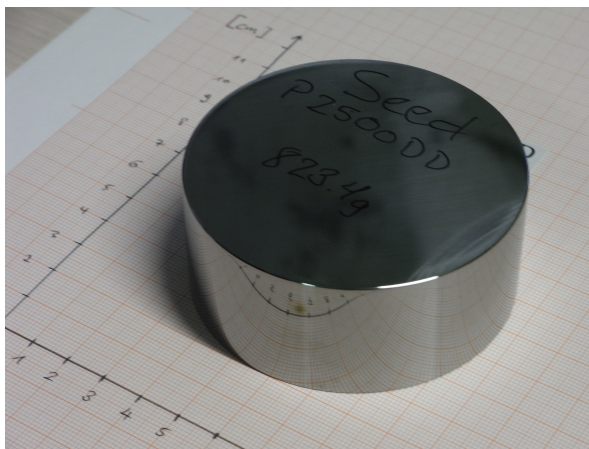
Figure 2.2: Example of a bare untreated enriched germanium crystal slice

Figure 2.3: Delivery of the first two enriched BEGe detectors mounted in vacuum cryostats ready for characterization.

The diode production at Canberra Semiconductor NV started at the end of January 2012. Figure 2.2 shows exemplarily a bare enriched germanium crystal which was converted into a diode. In February 2012, the first seven enriched BEGe detectors were delivered. They were produced out of two crystals. The data sheet of the first seven enriched detectors can be found in the appendix D.

Figure 2.3 shows the delivery of the first two enriched BEGe detectors in vacuum dip stick cryostats and LAr dewar to the GERDA Collaboration, collected for the collaboration at Canberra by M. Hult and the author of this thesis.

In August 2012 a second production and characterization phase of up to 23 diodes started.

2.1.3 The Infrastructure in HADES

Figure 2.4 shows schematically the HEROICA infrastructure installed in HADES. The main parts are:

- Two "Heidelberg tables" which were produced at the MPIK, Heidelberg
- three scanning tables, produced at INFN Padova/LNGS, MPIK and Tübingen, and
- the DAQ system with analog MCA and digital FADC modules.
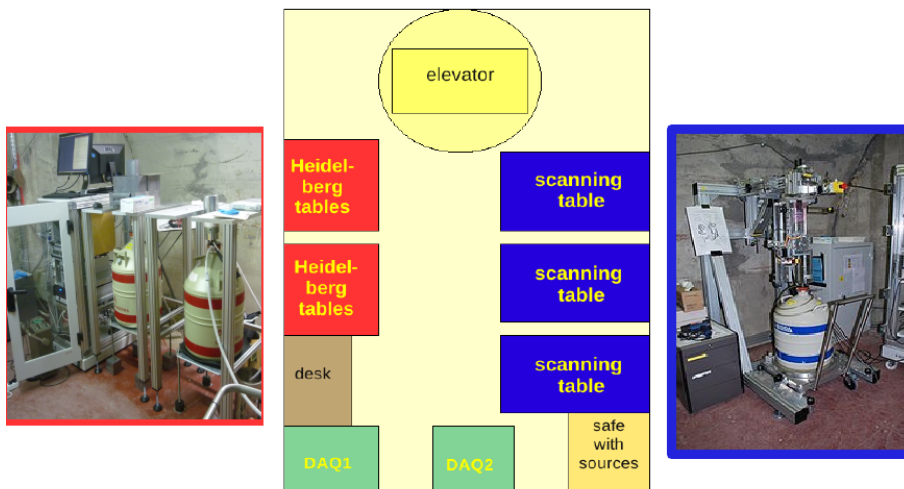
Figure 2.4: Schematic top view of the HEROICA site with two fixed scanning tables (red) and three automatized scanning tables (blue)

With these test-stands up to five detectors can be screened in parallel.

The Heidelberg Tables

 The Heidelberg (HD) tables in Figure 2.5 are used to perform measurements with radioactive calibration sources in a fixed position. Therefore, special source holders were designed as the knowledge of the exact source position is crucial for Monte Carlo simulations. To reduce the background from the environment the test stands are provided with a lead and copper shielding.

The Scanning Tables

The scanning tables (see Figure 2.6) allow to perform automatic scans of the lateral and top surface of the detector. All measurements are performed with collimated ^{241}Am sources of about $5.0\,\mathrm{MBq}$[1]. A $25.6\,\mathrm{mm}$ copper collimator with a hole diameter of $1\,\mathrm{mm}$ was used to ensure irradiation of small regions on the detector surface. The ^{241}Am scans were performed with up to 600 positions on top and 700 on the lateral surface of the BEGe diodes.
In the top scan circles are drawn around the center position of the crystal. The individual measurements are identified by their radial and angular position which is given relative to an arbitrary starting position – the "home" position of the source.
The vertical scans are performed from the top surface to the bottom surface of the crystal whereas the top surface of the detector corresponds to $0\,\mathrm{mm}$ height. With increasing height the source is positioned nearer towards the bottom end of the crystal, i.e. nearer to the read-out electrode. The individual measurements are identified by their difference to the top detector surface and angular position relative to the source "home" position. The "home" position of the source in the lateral scan is shifted by $180\,^\circ$ with respect to the top scan's "home" position.

---

[1]Reference date March 1, 2012

Figure 2.5: The Heidelberg table for fixed calibration source measurements with positioned detector in vacuum cryostat. The lead and copper shieldings are opened, the plastic source holders are shown left to the shielding.

The Front-End Electronics and DAQ Systems

All test stands are equipped with similar front-end electronics and DAQ modules as shown in Figure 2.7:

1. The Electronics consist of

   - a two channel ISEG HV power supply, module 246L,

   - a power supply module for the preamplifiers and

   - a charge-sensitive preamplifier (Canberra 2002CLS) mounted in the vacuum cryostat.

2. The DAQ System consists of

   - a non shaping amplifier, Genius Shaper, connected with a Struck FADC module read-out with a VME-CPU and

   - a spectroscopy amplifier connected with a Multi Channel Analyzers (MCA) module from Canberra and Ortec.

   the residual material from the enrichment process of the germanium

The MCA module saves energy spectra only whereas the FADC modules can be used to save the observed pulses in addition to the spectra. The pulses are saved in so-called calibration

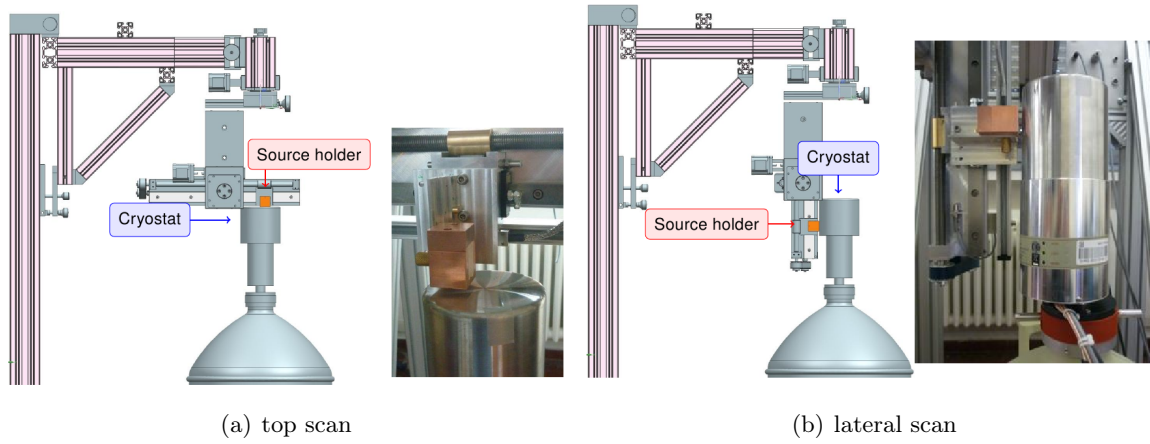(a) top scan   (b) lateral scan

Figure 2.6: Left: Top scan with collimated ^{241}Am source on the automatized scanning table. Right: The corresponding lateral scan. Taken from [Gar12].
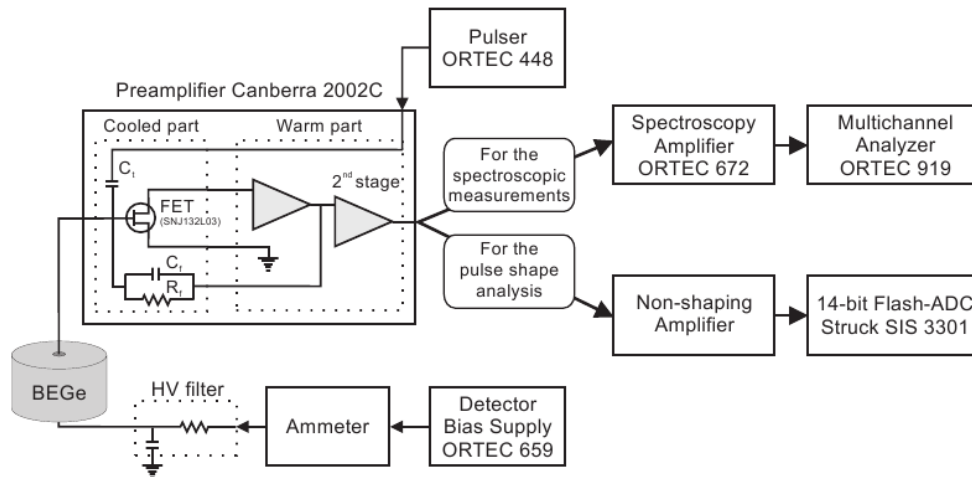
Figure 2.7: Schematic drawing of the front-end electronic and DAQ system used in HADES. The drawing is taken from [Hea10]

mode with a 160 μsec or 40 μsec long trace sampled at 25 MHz, the Low Frequency Long (LFL) trace. The A value is determined by using the High Frequency Short (HFS) trace which is sampled at 100 MHz, beginning 3 μsec before the trigger position and stopping 2 μsec after the trigger.

2.1.4 The HEROICA Standard Test Protocol

The test protocol covers all measurements that are needed in order to determine the most important characteristics of the diodes for operation in GERDA Phase II:

1. The operational parameters such as

   - the depletion voltage of the diode,

   - the energy resolution and

   - the leakage current determination.

2. The charge collection characteristics such as

   - the average top surface dead layer,

   - the active volume and

   - the charge collection efficiency in different positions.

3. The pulse shape performance.

The typical measurement parameters used for the first seven enriched BEGe detectors are summarized in Table 2.1.

The depletion voltage, i.e. the bias voltage required for a full depletion of the diode, is determined in ^{60}Co high voltage scans. This is done by monitoring the count rate as a function of applied high voltage: As soon as the diode is fully depleted the count rate does not increase any further.

The energy resolution is determined in ^{60}Co measurements: All seven enriched BEGe detectors have an energy resolution better than 2.3 keV at the 1332 keV line of ^{60}Co. The energy resolution is given as the FWHM of the peak.

The leakage current of the diodes is continuously read out during operation with voltage loggers at the test point of the preamplifiers.

The average dead layer is determined in uncollimated ^{241}Am and ^{133}Ba. The idea is that the charge efficiency for a certain energy depends on the dead layer thickness. Hence, the ratio of detected counts in peaks with different energies depends on the dead layer thickness which is finally determined by comparing Monte Carlo simulations to the measurements.

The active volume is determined using a ^{60}Co calibration source and comparing the measurements to Monte Carlo simulations. From the active volume an effective dead layer can be derived. The active volume is in contrast to the average dead layer sensitive to dead regions inside the crystal. Thus, the effective dead layer has not to coincide with the averaged dead layer estimated with ^{241}Am and ^{133}Ba sources.

The charge collection efficiency (CCE) scans are performed with a collimated ^{241}Am source using the automatized scanning tables. They are performed to check if the charge collection is deteriorated in some positions, e.g. by a non-uniformity of the dead layer or undepleted regions in the crystal. Therefore, the position-dependence of the count rate in the 59.5 keV of ^{241}Am is investigated.

Furthermore, the detector geometry as well as the diode position within the vacuum cryostat for input of the Monte Carlo simulations is checked in surface scans by monitoring the count rate.

The pulse shape performance and the PSD efficiencies as described in Section 1.3 are determined with a ^{228}Th calibration source centered directly on top of the detector's endcap. In addition, the position-dependence of the pulse shape performance is investigated with a collimated ^{241}Am source using the automatized scanning tables. In both measurements the data are acquired with the Struck FADC in order to save the charge pulses.

Cross-check with prototype depleted enriched BEGe diodes

Two prototype BEGe diodes ^{depl}DD and ^{depl}Ge-9 were brought to HADES for the optimization of the infrastructure, the test protocol and the measurement analysis. The diodes are isotopically depleted in ^{76}Ge, as they were produced from residual material of the enrichment process of the germanium for the new Phase II detectors. The diodes have been studied carefully in the past and show a very good performance in terms of energy resolution and pulse shape discrimination. Therefore, the prototype detectors are used to cross-check the HEROICA setup and to compare the diode's performance.

In addition to the measurements specified by the HEROICA standard test protocol, further tests concerning pulse shape analysis were performed such as high voltage scans with ^{228}Th and ^{241}Am, see Sectionsec:Vacuum-Cryo.

2.1.5 A Typical Shift at HADES

To manage the large amount of measurements required for the full characterization of all new enriched BEGe detectors, the measurements are taken in on-site shifts lasting about two weeks. The author of this thesis spent about 6 weeks on-site during the acceptance tests.

In principle all measurements can be started remotely, but the exchange of sources and arrangements of the setup, as well as the daily transports during diode production are left to the shifters on-site. The restricted access to the HADES underground laboratory from 4.30 a.m. to 4.00 p.m. requires a well prepared measurement schedule and organized transports to the manufacturer Canberra. Therefore, at least two on-site shifters are needed in HADES.

Twice per week, a discussion is held among the Acceptance Test Working Group in order to discuss the following measurement-schedule, analysis results and issues related to problematic diodes.

Measurement	Source Details			Source Position	Setup	DAQ
	Nuclide	Activity [kBq]	available sources			
Resolution High Voltage Scan Active Volume	^{60}Co	3-15	5	centered $\sim$ 20 cm above endcap	HD	MCA spectra + FADC spectra
Average Dead Layer	^{241}Am	100-500	5	centered $\sim$ 20 cm above endcap	HD	MCA spectra
Average Dead Layer	^{133}Ba	3-45	5	centered $\sim$ 20 cm above endcap	HD	MCA spectra
Charge Collection Efficiency Pulse Shape Analysis	^{241}Am	5000	3	centered $\sim$ 1 cm above endcap	Scanning tables	MCA spectra + FADC pulses
Pulse Shape Analysis	^{228}Th	1	1	centered directly on endcap	HD	FADC pulses

Table 2.1: Summary of the measurements performed with the first seven enriched BEGe detectors according to the HEROICA test protocol

2.2 BEGe Tests in GDL
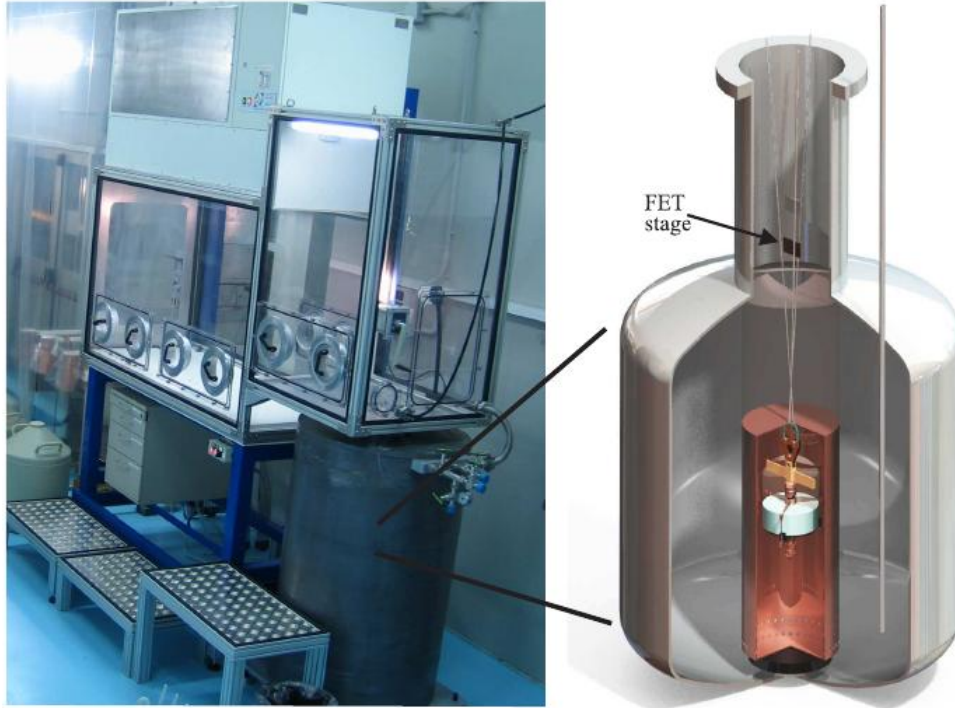
Figure 2.8: The test bench in GDL and the 70 l dewar for cryogenic liquid [Hea10].

After the characterization in HADES, two of the newly produced enriched BEGe detectors were prepared and tested in Germanium Detector Laboratory (GDL) by D. Budjas and K. Gusev. The GDL is located in the Laboratori Nazionali del Gran Sasso in close proximity to the GERDA experimental site. The laboratory is a clean room of level 10000 designed for testing germanium detectors prior to their installation in the GERDA LAr cryostat. For more detailed information about the experimental setup and infrastructure in GDL see [Hei09].
The measurements were performed in the test bench in GDL shown in Figure 2.8 which is equipped with a glove box for preparation of the test in an ultra clean bench. The bare detectors were operated in the 70 l dewar filled with LAr.

2.3 BEGe Tests in GERDA
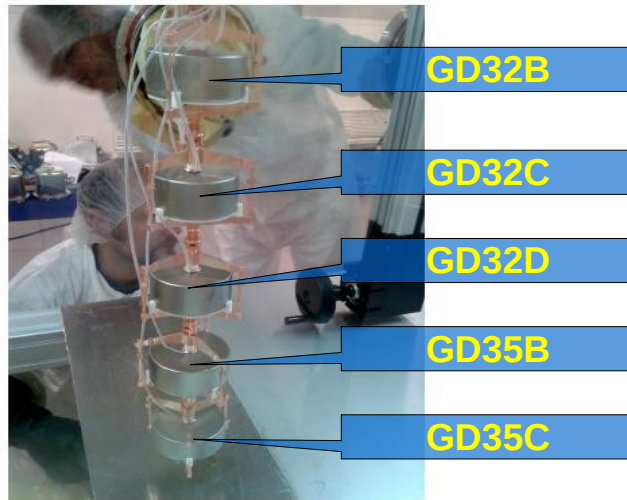
Figure 2.9: The string setup with the five enriched BEGe detector

As mentioned in Section 1.1.2 five enriched BEGe detectors were installed into the GERDA LAr cryostat in June, 2012. Figure 2.9 shows the string configuration: GD32B is the top-most diode, GD35C the bottom-most diode in the string. The total mass of the BEGe detectors is 3.63 kg. The applied high voltage for all five detectors is 3.5 V. GD35B and GD35C are connected to the same HV line.

2.2 summarizes the five calibrations that will be used for investigation of the PSA performance in Section 3.2.2 and 3.2.3.

Calibration no	1	2	3	4	5
	Run 35				Run 36
Date	07.07.12	08.07.12	23.07.12	27.07.12	10.08.12
Duration	1.9 h	5.5 h	3.1 h	2.9 h	1.4 h
Statistics accumulated in 10 keV- region around DEP					
GD32B	872	3634	915	833	443
GD32C	890	3951	720	928	502
GD32D	639	1678	1148	797	341
GD35B	1335	1138	3597	2082	618
GD35C	770	862	1573	1440	625

Table 2.2: Summary of calibration data taken in GERDA cryostat until 10.08.12. Run 36 began on July 27, 2012.

Chapter 3

Pulse Shape Performance

For the first 7 isotopically enriched in ^{76}Ge BEGe detectors a series of measurements in three test facilities were performed:

- In the framework of the acceptance tests at HADES – measurements of BEGe diodes in vacuum cryostats with passivation layer

- In GDL – measurements in LAr of BEGe diodes without passivation layer

- In the GERDA LAr cryostat – measurements in LAr of BEGe diodes with passivation layer

In the following section the results on pulse shape performance and discrimination efficiency of the new enriched BEGe detectors obtained in the different configurations will be compared. The following analysis has been performed with the software framework GELATIO [Aea11a].

3.1 Performance in Vacuum Cryostat

Investigation of the PSD efficiency of the first 7 enriched GERDA BEGe detectors were performed at HADES underground laboratory in the HEROICA test area. As a reference, measurements with two prototype BEGe detectors which are isotopically depleted in ^{76} Ge, Ge-9 and DD, were taken.
In addition to conventional pulse shape measurements with a ^{228}Th source, pulse shape studies with collimated ^{241}Am sources were performed. In an attempt to improve the discrimination efficiency two non-well performing diodes were sent to the manufacturer for reprocessing.

3.1.1 Pulse Shape Discrimination Efficiencies

A/E **distributions in the DEP**
Figure 3.1 shows the normalized A/E distributions around the DEP of ^{228}Th at 1592.5 keV of the 7 enriched BEGe diodes in comparison to ^{depl}Ge-9 which represents the A/E distribution observed so far with prototype detectors (compare the results with the ^{depl}DD BEGe diode obtained in LLL at MPIK in Section 1.3.2). The selected energy region is 1590 - 1595 keV. The corresponding ^{228}Th measurements are found in Table A.1 in Appendix A. Table 3.2 compares corresponding A/E resolutions in the DEP.

Unexpectedly, a different behavior of the A/E distribution in the DEP as previously observed with BEGe detectors was found:

1. Two enriched BEGe detectors, GD32B and GD35B, have an A/E distribution compatible to the ^{depl}Ge-9 (see Figure 3.1 (a)).

2. Three enriched BEGe detectors, GD32A, GD32D and GD35A, have a broadened A/E distribution (see Figure 3.1 (b)).

3. Two enriched BEGe detectors, GD32C and GD35C, show a clear double structured A/E distribution (see Figure 3.1 (c)).

In the following we will refer to unusual A/E distribution as "A/E Anomaly".

Pulse Shape Discrimination Efficiencies

Table 3.3 summarizes the pulse shape discrimination efficiencies as introduced in Section 1.3 for the 7 enriched BEGe detectors and the ^{depl}Ge-9. As for the prototype BEGe detectors Ge-9, the A/E parameter analysis for pulse shape discrimination is an efficient method for background suppression.

However, only GD32B and GD35B show a compatible discrimination efficiency to the ^{depl}Ge-9 in the SEP and the ROI, i.e. around 2039 keV. The remaining five enriched BEGe detectors show a deteriorated PSD performance in comparison to GD32B, GD35B and the depleted detectors. GD32D and GD32A deviate the most in discrimination efficiency from ^{depl}Ge-9. With 12.1 % of surviving events in the SEP, GD32A has a significantly worse performance compared to the depleted BEGe.

The deterioration in pulse shape discrimination efficiency is correlated to the "A/E Anomaly": GD32B and GD35B show both a narrow A/E distribution in the DEP as well as good discrimination efficiency, such as the prototype BEGe diode, whereas the detectors with a broader or double-structured A/E distribution show a deteriorated PSD performance in comparison to ^{depl}Ge-9.

In the case of deteriorated PSD performance, a stronger cut would be necessary to achieve a compatible discrimination efficiency in the ROI to the depleted detectors . The PSD efficiencies for different level of acceptance in the DEP has been evaluated. The results are shown in Table 3.4 [1]. for example, a 31 % survival probability is obtained with GD32C by accepting only 70 % of the events in the DEP. This means a loss in sensitivity of about 20 %.

---

[1] evaluated by Alexey Lubashevskiy

(a) single structure

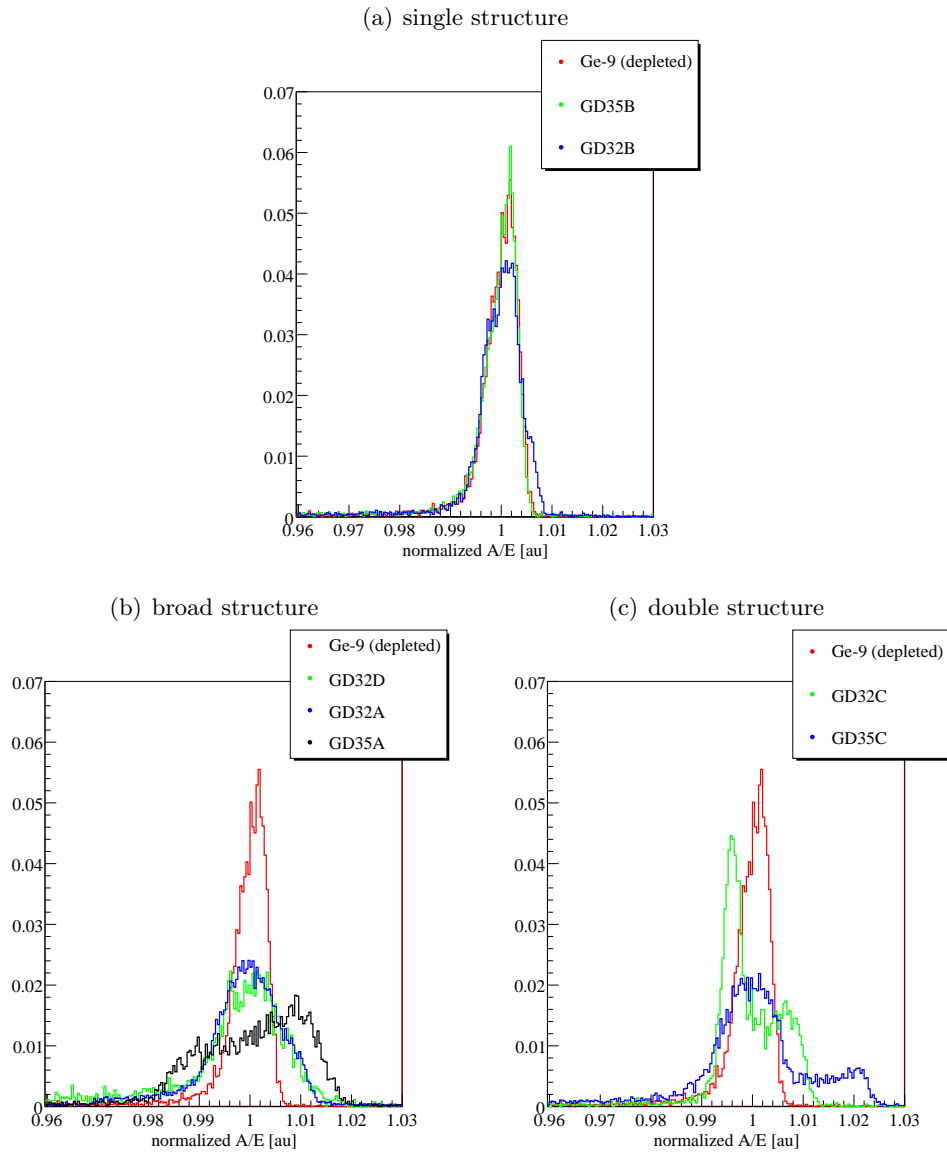(b) broad structure

(c) double structure

Table 3.1: A/E distributions of the first 7 enriched BEGe detectors compared to the depleted Ge-9 detector. The selected energy region around the DEP is 1590 - 1595 keV. A/E mean values and integrals are normalized to unity.

| Detector | Energy resolution (FWHM) in | | Resolution in DEP |
	DEP [keV]	FEP 2.6 MeV[keV]	[FWHM/A/E mean]
GD35A	1.87 ± 0.03	2.39 ± 0.01	2.20%
GD32C	1.86 ± 0.04	2.44 ± 0.01	1.27%
GD32A	1.88 ± 0.02	2.44 ± 0.01	1.46%
GD32D	1.86 ± 0.04	2.41 ± 0.02	1.64%
GD35C	1.81 ± 0.03	2.41 ± 0.01	1.70%
GD35B	1.84 ± 0.03	2.45 ± 0.01	0.61%
GD32B	1.90 ± 0.03	2.41 ± 0.01	0.80%
Ge-9 (depleted)	1.85 ± 0.03	2.41 ± 0.01	0.48%

Table 3.2: The relative resolution of the A/E distribution, i.e. FWHM over A/E peak position in the DEP is shown for the seven enriched BEGe detectors measured in vacuum cryostat at HADES. FWHM and mean of A/E are estimated by a Gaussian fit. Uncertainties from fits are negligible. However, the A/E distribution are not purely Gaussian, such that the given resolution can be regarded only as a first order approximation.

Energy region	GD35A	GD32C	GD32A	GD32D
DEP	0.900 ± 0.023	0.900 ± 0.026	0.900 ± 0.013	0.900 ± 0.027
FEP 1.6 MeV	0.128 ± 0.013	0.112 ± 0.026	0.180 ± 0.020	0.181 ± 0.036
SEP	0.078 ± 0.013	0.080 ± 0.017	0.121 ± 0.012	0.142 ± 0.032
FEP 2.6 MeV	0.132 ± 0.012	0.117 ± 0.013	0.163 ± 0.012	0.217 ± 0.035
2004-2074 keV	0.400 ± 0.021	0.403 ± 0.030	0.427 ± 0.019	0.464 ± 0.036
1989-2089 keV	0.395 ± 0.020	0.404 ± 0.029	0.427 ± 0.018	0.466 ± 0.033
Lifetime	5.0 h	5.0 h	14.0 h	2.7 h
energy region	GD35C	GD35B	GD32B	^{depl}Ge-9
DEP	0.900 ± 0.017	0.899 ± 0.018	0.900 ± 0.020	0.901 ± 0.029
FEP 1.6 MeV	0.159 ± 0.019	0.104 ± 0.016	0.106 ± 0.015	0.099 ± 0.025
SEP	0.106 ± 0.023	0.056 ± 0.010	0.051 ± 0.011	0.057 ± 0.016
FEP 2.6 MeV	0.157 ± 0.020	0.065 ± 0.010	0.082 ± 0.011	0.074 ± 0.014
2004-2074 keV	0.404 ± 0.028	0.325 ± 0.024	0.323 ± 0.022	0.327 ± 0.036
1989-2089 keV	0.405 ± 0.028	0.322 ± 0.024	0.323 ± 0.021	0.324 ± 0.035
Lifetime	8.0 h	8.0 h	7.0 h	6.0 h

Table 3.3: PSD efficiencies for the 7 enriched BEGe detectors compared to the efficiency of the depleted Ge-9 BEGe. The measurements were taken in vacuum cryostat at the HADES underground laboratory. The efficiencies were evaluated by Alexey Lubashevskiy, Alex Hegai and the author of this thesis

Energy region	Level of acceptance in DEP of 2.6 MeV		
	90%	80%	70%
DEP	0.900 ± 0.026	0.800 ± 0.023	0.702 ± 0.021
FEP 1.6 MeV	0.112 ± 0.027	0.087 ± 0.017	0.075 ± 0.014
SEP	0.080 ± 0.018	0.059 ± 0.011	0.050 ± 0.011
FEP 2.6 MeV	0.117 ± 0.013	0.097 ± 0.005	0.085 ± 0.004
2004-2074 keV	0.403 ± 0.030	0.350 ± 0.017	0.308 ± 0.013
1989-2089 keV	0.404 ± 0.029	0.350 ± 0.016	0.308 ± 0.012

Table 3.4: PSD efficiencies for different level of acceptance in the DEP evaluated for GD32C. Evaluation done by Alexey Lubashevskiy.
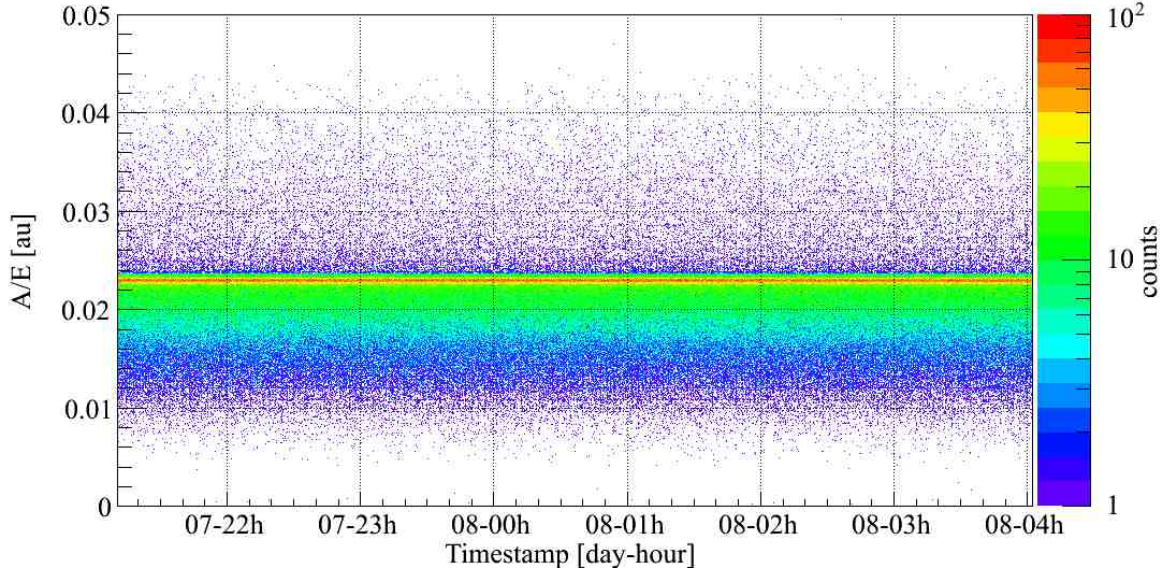

Figure 3.1: A/E distribution vs time measured for GD35C (measurement no 14 in Table A.1). The A/E values for all energy regions are shown such that the stability of the single-site event line is represented in red.

3.1.2 Investigation of the HEROICA Setup

In order to find the origin for the observed "A/E Anomaly" a full investigation of the measurement setup was carried out searching for problems arising from the electronics and DAQ during the measurements. Details about the electronics and DAQ systems can be found in Section 2.1.3.

The data quality, hence the pulse shape shape performance, could be influenced by

- instability of A/E in time or

- noise in the electronics and DAQ

A/E Stability in Time

A broadened or multi-structured A/E distribution could be explained by unstable A/E values in time. Figure 3.1 shows A/E as a function of time measured with GD35C. No cut on energy has been applied as events in the DEP have limited statistics. The red band represents the single-site event (SSE) line. Figure 3.1 demonstrates that A/E was stable during the measurement and cannot explain the observed double-structure in the A/E distribution in the DEP.
None of the ^{228}Th measurements analyzed in Section 3.1.1 showed instabilities in time.

The Electronics
As pointed out in Section 2.1.3, the characterization of all detectors was performed with the same electronics shown in Figure 2.7. Two enriched and both depleted BEGe detectors do not show a deteriorated PSD performance therefore it is unlikely that the "A/E Anomaly" arises from the HV module or the voltage supply of the preamplifier.
Recent measurements with new enriched diodes using the same vacuum cryostats and preamplifiers as the first batch of enriched BEGe detectors rule out that the unexpected A/E distribution originates from individual preamplifier properties.

The DAQ System
The signal is amplified by a non-shaping amplifier and data for pulse shape analysis are acquired with one FADC module only. In order to rule out that the DAQ system is the origin of the "A/E Anomaly" measurements in different configurations, with and without Genius Shaper module and different FADC channels, were taken: No change in PSD performance has been observed for different setup configuration.

Noise Studies
The A value is very sensitive to noise, as it is determined by the derivative of the read-out signal: The higher the noise, the harder to distinguish noise from the current pulse.
Studies of the dependence of energy resolution from shaping time do not give any hint that high noise was present in the measurements.
However, the A/E distribution is dominated by the resolution of A. Therefore, the dependence of the distribution of A from different shaping times was studied. In the analysis chain a MWA is applied before determination of the A parameter. The standard procedure applies

three times a 50 ns MWA. This application is intended to smooth the pulse but not so much as to loose information.

To further rule out a possible contribution of noise and problems in the analysis chain, pulse shape analysis was performed to the same measurement with and without MWA applied before determination of the A parameter. Table 3.5 compares the PSD efficiencies for three times 50 ns MWA and no MWA applied[2].

No improvement by applying a MWA to the pulse. If noise was present, the application of a MWA an improvement in the A resolution, thus an improvement in PSD efficiencies, was expected as the MWA works similar to a low-pass filter.

Energy region	Applied Moving Window Average	
	50 ns	without
DEP	0.900 ± 0.023	0.900 ± 0.029
FEP 1.6 MeV	0.128 ± 0.010	0.117 ± 0.010
SEP	0.078 ± 0.007	0.067 ± 0.007
FEP 2.6 MeV	0.132 ± 0.002	0.135 ± 0.002
2004-2074 keV	0.395 ± 0.005	0.404 ± 0.005
1989-2089 keV	0.395 ± 0.004	0.404 ± 0.004

Table 3.5: PSD efficiencies for three times 50 ns MWA and no MWA applied to the same measurement. The numbers give the fraction of events after applying the A/E cut in the indicated energy regions. Evaluation was performed by Alexey Lubashevskiy.

So far, no indication has been found that the "A/E Anomaly" originates in any problems with hardware installed in HADES or the applied software analysis procedures. Thus, the "A/E Anomaly" is likely to originate in the detectors themselves.

3.1.3 Working Hypothesis: Distortion of the Electric Field Inside Diodes

Section 1.2.3 describes the so-called "Funneling Effect" which ensures that events depositing energy in the bulk of the detector have similar pulse shapes, thus A/E values, which would be reflected in a narrow A/E distribution in the DEP (Section 1.3).

The broadened A/E distributions of GD32A, GD32C, GD32D, GD35A and GD35C could result from a superposition of position-dependent A/E values over the entire crystal. As pointed out by D. Budjas the most probable hypothesis explaining any change in the electric field distribution such that the "Funneling Effect" is destroyed are :

1. Surface effects

2. Local differences in impurity concentration inside the bulk of the diodes

Surface effects   could be a distortion of the internal electric field from the surface of the diode. This could be e.g. trapped charges in the groove: If there were charges inside the

---

[2]evaluated by Alexey Lubashevskiy

groove, the electric field distribution would be changed in such a way that bending towards the middle plane of the crystal would be prevented. Hence, charge collection would happen along different paths near the read-out electrode. The important last part of the collection path , i.e. through the strong weighting potential, would be different, resulting in a non-identical sharp rising part of the pulse. Therefore, A/E would be different for different interaction points inside the crystal.

Charges in the groove would result in a radial and vertical dependence of A/E from the interaction position. If the charge distribution was asymmetric, this would lead to an additional angular dependence.

Local differences in the impurity concentration would effect all charge collection paths in its vicinity. In this case an angular dependence of pulse shape is expected. Moreover, asymmetric A/E distributions could give a hint towards further intrinsic effects. Possible candidates are defects in the crystal structure and charge trapping inside the crystal.

Charge Collection Efficiency (CCE) Studies were performed at HADES in order to investigate the origin of the "A/E Anomaly. A collimated ^{241}Am was used for such investigation. ^{241}Am has a gamma line at 59.5 keV. For such energies Photoeffect dominates the energy deposition in the detector. Thus, mainly single-site events are expected in the γ-line. Furthermore, the interaction of such low energy γ-rays takes place near the crystal surface. As a consequence, all charge collection paths have maximum length. Any effect on charge carriers along their way towards the read-out electrode should be seen better than in the case of higher energetic gamma rays. Such gamma rays penetrate further into the crystal, hence have a shorter collection path on average.

It is to investigate if any unexpected A/E dependence on position is found to give hints towards the hypothesis of surface or intrinsic effects. Therefore, dedicated pulse shape studies to investigate the intrinsic properties of the diodes were performed. They will be discussed in Section 3.1.4, Section 3.1.5 and Section 3.1.6.

3.1.4 Investigation of the A/E Position-Dependence

To investigate if the A/E value is position-dependent, measurements were taken with a collimated ^{241}Am source located in different places on top of the endcap. Figure 3.2 shows the modified lead plate used for the investigation. The measurements were taken at different azimuthal angles near the crystal edges and in the center of the endcap.

In the analysis, the A/E distribution of the 59.5 keV peak was fitted with a Gaussian function in order to determine the A/E peak position. Table 3.6 summarizes the deviation in A/E peak position for different azimuthal angles compared to the center position. Uncertainties in deviation of A/E peak position from the fit are negligible.

In previous measurements with depleted prototype BEGe detectors it was found that the deviation in A/E peak position should be smaller than 1 % for all positions of the collimated ^{241}Am source[Bud12a]. The CCE measurement with ^{depl}Ge-9, GD32B and GD35B, confirms this expectation: The enriched diodes with a good PSD performance, show a deviation smaller than 1 % for all measured positions. GD35A and GD32C show only in one of the measured positions a deviation larger than 1 %. GD32D, GD35C and GD32A have larger deviations up to 4 % in all measured positions.

The geometrical CCE scans do confirm that the detectors with better pulse shape performance,

GD35A		GD32C		GD32A		GD32D	
azimuth	deviation [%]	azimuth	deviation [%]	azimuth	deviation [%]	azimuth	deviation [%]
$0\,^{\circ}$	-0.03	$0\,^{\circ}$	0.53	$0\,^{\circ}$	2.69	$0\,^{\circ}$	-
$90\,^{\circ}$	0.82	$90\,^{\circ}$	1.89	$90\,^{\circ}$	2.34	$90\,^{\circ}$	3.29
$180\,^{\circ}$	2.36	$180\,^{\circ}$	-	$180\,^{\circ}$	2.35	$180\,^{\circ}$	4.31
$270\,^{\circ}$	0.46	$270\,^{\circ}$	0.52	$270\,^{\circ}$	2.80	$270\,^{\circ}$	4.13
GD35C		GD35B		GD32B		^{depl}Ge-9	
azimuth	deviation [%]	azimuth	deviation [%]	azimuth	deviation [%]	azimuth	deviation [%]
$0\,^{\circ}$	2.88	$0\,^{\circ}$	0.35	$0\,^{\circ}$	0.35	$0\,^{\circ}$	0.04
$90\,^{\circ}$	2.25	$90\,^{\circ}$	0.65	$90\,^{\circ}$	0.82	$90\,^{\circ}$	0.08
$180\,^{\circ}$	1.85	$180\,^{\circ}$	-	$180\,^{\circ}$	-	$180\,^{\circ}$	0.04
$270\,^{\circ}$	2.78	$270\,^{\circ}$	0.34	$270\,^{\circ}$	0.19	$270\,^{\circ}$	0.08

Table 3.6: Deviation of the A/E peak position from the A/E peak position in the center of the diode measured for the first seven enriched and the ^{depl}Ge-9 BEGe. Measurements were performed with collimated ^{241}Am source at the indicated angle on the endcap of the vacuum cryostat. The A/E peak position for each measurement was estimated by a Gaussian fit of the A/E distribution in the 59.5 keV-line.

Figure 3.2: Picture of a detector's cryostat with the modified Pb plate used for the collimated ^{241}Am top scans to investigate the A/E position-dependence.

GD35B and GD32B, have similar behavior to ^{depl}Ge-9. The detectors with deteriorated PSD performance show a stronger position-dependence in A/E. However, so far no correlation between broadened or multi-structured A/E distributions and unexpected deviation in A/E peak position was found.

3.1.5 Investigation of the A/E Dependence from Bias Voltage

For further investigation of the origin of the position-dependence of A/E, high voltage scans with a collimated ^{241}Am source were performed.

Two effects with opposite expected high voltage dependence were in the focus of the investigation:

1. Undepleted regions in the detector above the depletion voltage which vanish with increasing applied high voltage. The A/E position-dependence becomes smaller the higher

the applied bias voltage is

2. The A/E position-dependence originates in the deterioration of the electric field inside the crystal and increases the higher the applied bias voltage is

As proposed by C. Cattadori, the observed "A/E Anomaly" might originate in undepleted regions inside the crystal where the electric field is zero, e.g. dead sub-volumes in the bulk of the diode. In such regions the charge carriers do not drift along the electric field lines. The drift is purely due to thermal diffusion. Thus, the time needed by the charge carriers to drift through undepleted spots is compatibly long. Correspondingly, charge carriers that partly drift through undepleted regions show decreased A/E values in comparison to those charge carriers that drift through depleted regions only.
The described effect caused by undepleted regions in the crystal should become smaller with increasing applied voltage as insufficient depleted spots inside the crystal vanish. Therefore, if the "A/E Anomaly" originates in undepleted regions inside the crystal, it is expected that any differences in the A/E peak position for different positions become smaller with increasing high voltage and vanishes completely for full depletion of the diode.

However, as pointed out by M. Agostini, if the "A/E Anomaly" originates in a deteriorated electric field inside the detector, e.g. by charges on the surface of the diode, and the diode is fully depleted, the opposite behavior is expected: The deviation in the A/E peak position for different locations of energy depositions become larger with increasing high voltage.
As described in Section 1.2.3, the charge carriers' movement towards the center of the crystal is driven by the electrical field built by the space charge distribution. From the middle plane of the detector the charge carriers drift towards the read-out electrode following the electric field according to the different potential of the electrodes. With increasing applied high voltage, the difference in the electrical potential of the electrodes becomes bigger. Hence, the electric field resulting from the applied bias voltage becomes stronger and weakens the funneling effect. The bending towards the center of the crystal becomes less strong with increasing high voltage. Thus, the A/E position-dependence increases as the charge carriers drift through different parts of the strong weighting potential near the read-out electrode. Therefore, the difference between A/E values for different positions is expected to become larger with increasing high voltage.

For investigation of the A/E bias dependence the same measurement setup as in Figure 3.2 was used. The HV scans were performed for the five detectors showing the "A/E Anomaly": GD32A, GD32C, GD32D, GD35A, GD35C and ^{depl}Ge-9 as a reference.
The bias voltage was changed approximately from $500\,\mathrm{V}$ below depletion voltage to $500\,\mathrm{V}$ above recommended bias voltage of the detector in question (see data sheets for comparison in Appendix D) in $100\,\mathrm{V}$ steps. The HV scans were performed for different positions on top and/or at the side of the detector. The center of the crystal was estimated by the center of the endcap of the detector. However, this must not be the exact center position of the diode. As in previous analysis, the A/E distribution of the $59.5\,\mathrm{keV}$ peak was determined by fitting a Gaussian function in order to extract the peak position.

Results on the bias-dependence of A/E
In Figure 3.4 the A/E peak position as a function of high voltage is shown for the five enriched

BEGe detectors with deteriorated pulse shape performance and for the ^{depl}Ge-9:

1. All enriched BEGe detectors with deteriorated pulse shape performance show well separated A/E values of the outer rings from the center A/E position.

2. The difference between A/E in the center to the outer positions grows with increasing applied voltage except for ^{depl}Ge-9.

3. The ^{depl}Ge-9 does not show such HV dependence of the A/E peak position: The A/E peak position is similar for all measured positions.

This gives reason to the assumption that the enriched BEGe diodes are fully depleted and that the "A/E Anomaly" does not originate from undepleted regions within the crystal.

Independent from the question whether the detector is fully depleted or not, the HV ^{241}Am scans might hold interesting information about the depletion process in a diode. A discontinuous jump is observed in the A/E peak position in Figure 3.4. This jump happens at the transition to the full depletion of the detector. However, the exact physics of the dynamics in the depletion process is not yet fully understood. This will be further investigated by Monte Carlo Simulations.

Beside the discontinuity, in a fully depleted detector the A/E of a single measurement point behaves as expected: A/E increases with increasing bias voltage. As soon as the detector is depleted the position of the energy peak depends only slightly from the applied bias, whereas, the time needed for the full charge collection decreases with increasing applied high voltage. Thus, the amplitude of the current pulse increases with the applied bias voltage, i.e. the A value increases.

Summary of High Voltage Dependence of PSD Performance

The ^{241}Am-HV scans confirm again that the five enriched BEGe detectors with deteriorated PSD performance show a position-dependence in A/E. This dependence becomes smaller with decreasing applied high voltage. However, no significant effect on the A/E distribution in the DEP was observed in ^{228}Th measurements at different applied bias voltages. Figure 3.3 shows the A/E distribution for different applied high voltages. No change in A/E resolution which would change significantly the PSD performance was observed.
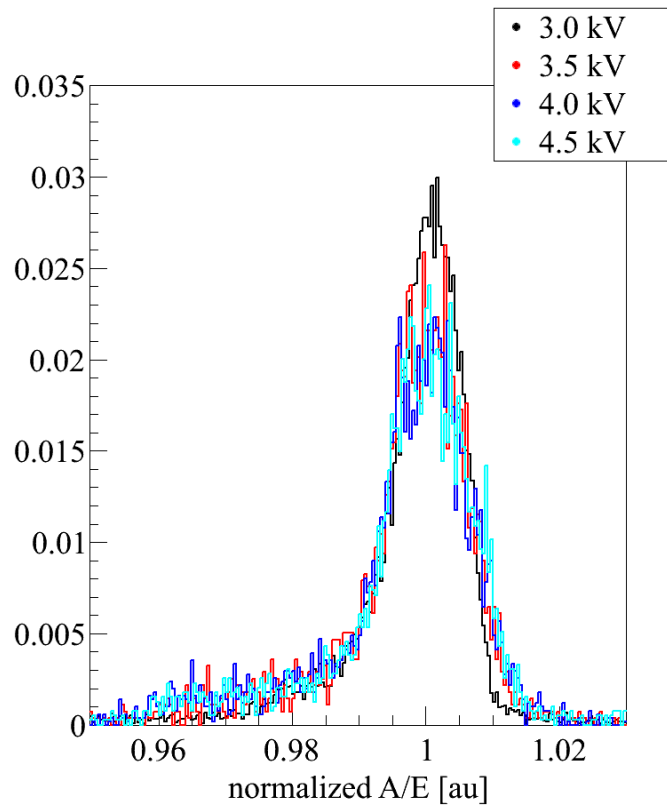
Figure 3.3: Normalized A/E distributions in the DEP measured with GD32D at different applied high voltages. The measurement at 3.0 kV has about four times as much statistics as the other three measurements, compare Table A.1. The bias voltage recommended by the manufacturer Canberra is 4.0 keV.
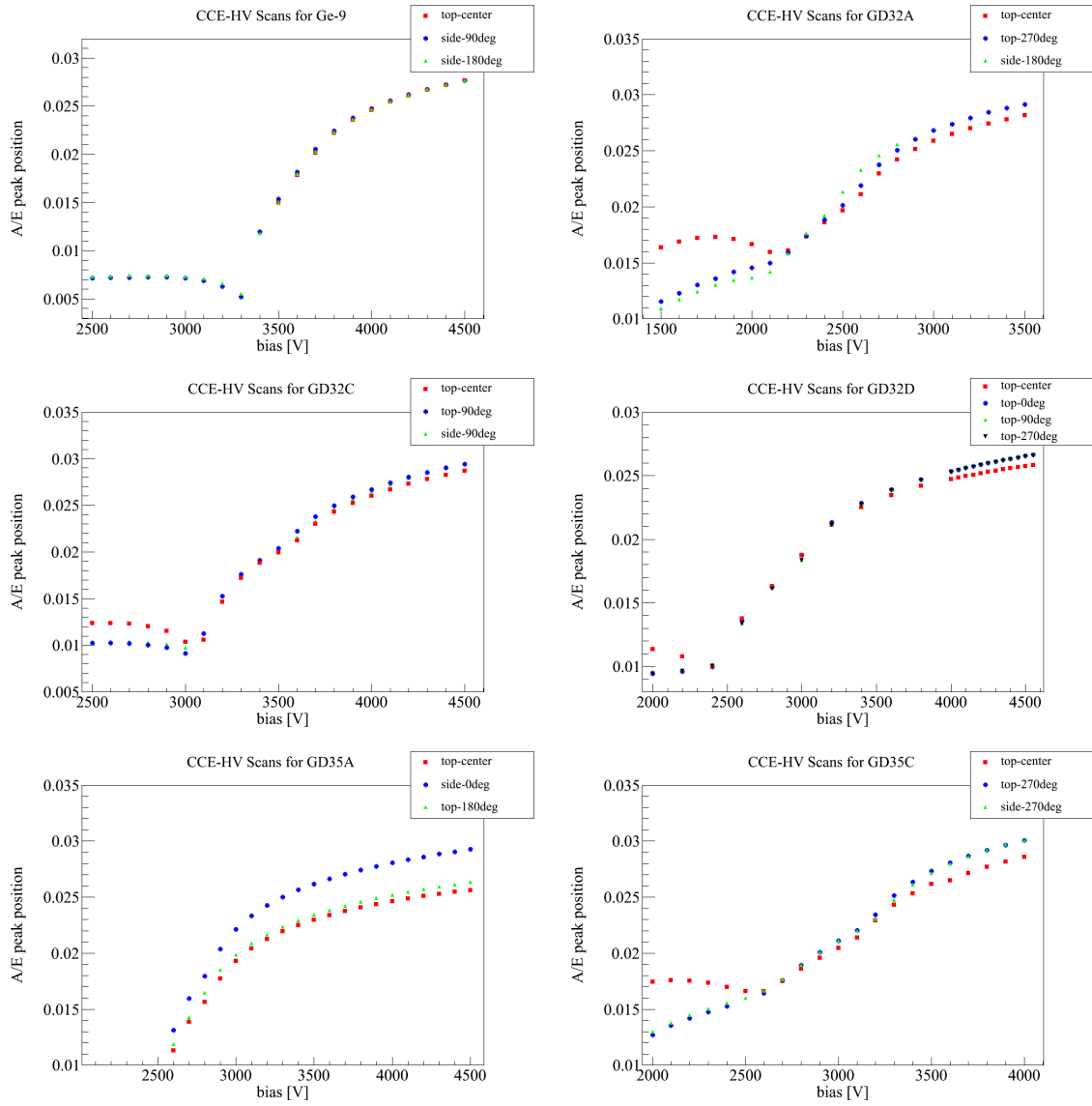
Figure 3.4: A/E peak position as a function of applied high voltage. The measurements were performed for 5 enriched BEGe diodes that show deteriorated PSD performance and the depleted Ge-9.
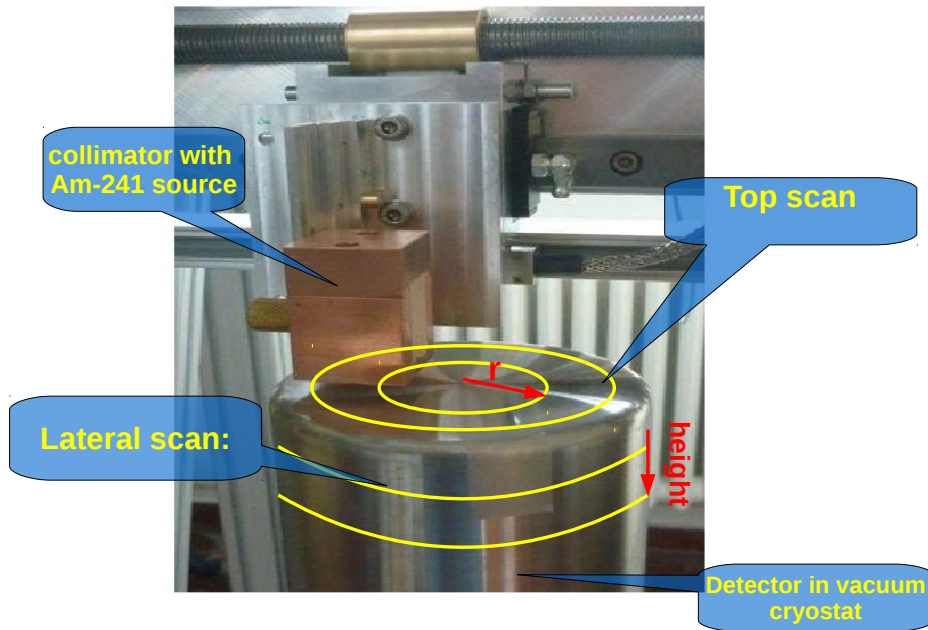
Figure 3.5: Demonstration of the performed collimated ^{241}Am scans. The detectors are scanned on the top and side surface in circles.

3.1.6 Investigation of A/E in Detailed Surface Scans

For further investigation of the "A/E Anomaly" more detailed surface scans were performed with the automatized scanning tables described in Section 2.1.3. In the top scan, the measurements were taken in circles around the center of the diode in steps of $5\,°$ to $30\,°$. The individual measurement points are addressed by their distance to the center of the diode, i.e. the radius of the drawn circle, and the angular position. In the lateral scans circles were drawn around the side of the detectors endcap at a certain height, i.e. the distance to the top surface of the diode. The individual measurement points are identified by the height and the angular position.

In the analysis, events in a $9\,\sigma$ (corresponding to $\sim$3.8 FWHM) region around the 59.5 keV peak were investigated. The A/E peak position was determined by fitting the distribution with a Gaussian. The indicated uncertainties take only the fitting error into account.

Measurements were performed with all enriched BEGe detectors but GD32A. As a reference ^{241}Am surface scans were performed with ^{depl}DD and ^{depl}Ge-9 BEGe detector. Figure 3.6 and 3.7 show the results of the A/E position-dependence. Most of the detector, including the ^{depl}Ge-9, show a position-dependence in A/E:

1. Except for the ^{depl}DD BEGe detector, all detectors show a sinusoidal dependence of the A/E peak position

2. The angular oscillation is smallest in the ^{depl}Ge-9. The maximum measured A/E peak positions differs less than $1\,\%$ from the minimal A/E peak position. This is in agreement with previous ^{241}Am measurements in Section 3.1.4

3. Among the enriched detectors, the spread of the A/E peak position is smallest for GD32B and GD35B, which are the detectors with the most narrow A/E distribution in the DEP. This is also in agreement with the ^{241}Am scans in section 3.1.4

4. GD32C shows a stronger angular oscillation than GD32B and GD35B

5. The enriched BEGe detector with the broadest A/E distribution in the DEP, GD35A, shows a large angular oscillation. The difference between maximum and minimum A/E peak position in comparison to the minimum value is estimated to 4.5 %.

In additional to the angular-dependence, two detectors show a strong radial-dependence in the A/E peak position:

1. GD32D shows a similar spread to GD32B and GD35B. However, the A/E values show a strong radial dependence, why the spread in A/E peak positions is expected to grow with decreasing radius which will be confirmed in a later measurement in Section 3.1.7. The same behavior is seen in the vertical scan: with decreasing distance to the read-out electrode A/E peak position becomes smaller.

2. GD35C shows the biggest spread in A/E peak positions. In the top scan the angular oscillation observed in a single ring is compatible to the oscillation observed in GD32B and GD35B. However, the A/E depends strongly on the distance to the center position: The resulting maximum A/E peak position differs about 5.6 % from the minimum observed A/E peak position. Yet, the vertical scan does not show a strong dependence on the measurement distance to the top surface.

The detailed surface scans with a collimated ^{241}Am source show very clearly that the two detectors, with compatible PSA performance than the prototype BEGe diodes, show the smallest A/E position-dependence among the enriched BEGe detectors. All scanned detectors with deteriorated pulse shape performance have a strong position-dependence in A/E. The observations are in agreement with previous ^{241}Am scans in Section3.1.4 and 3.1.5 and strengthen the result that the deteriorated PSD efficiency is connected to the position-dependence of A/E.
However, no correlation between the double-structure in the A/E distribution of the DEP and position-dependence of the A/E peak position can be drawn.
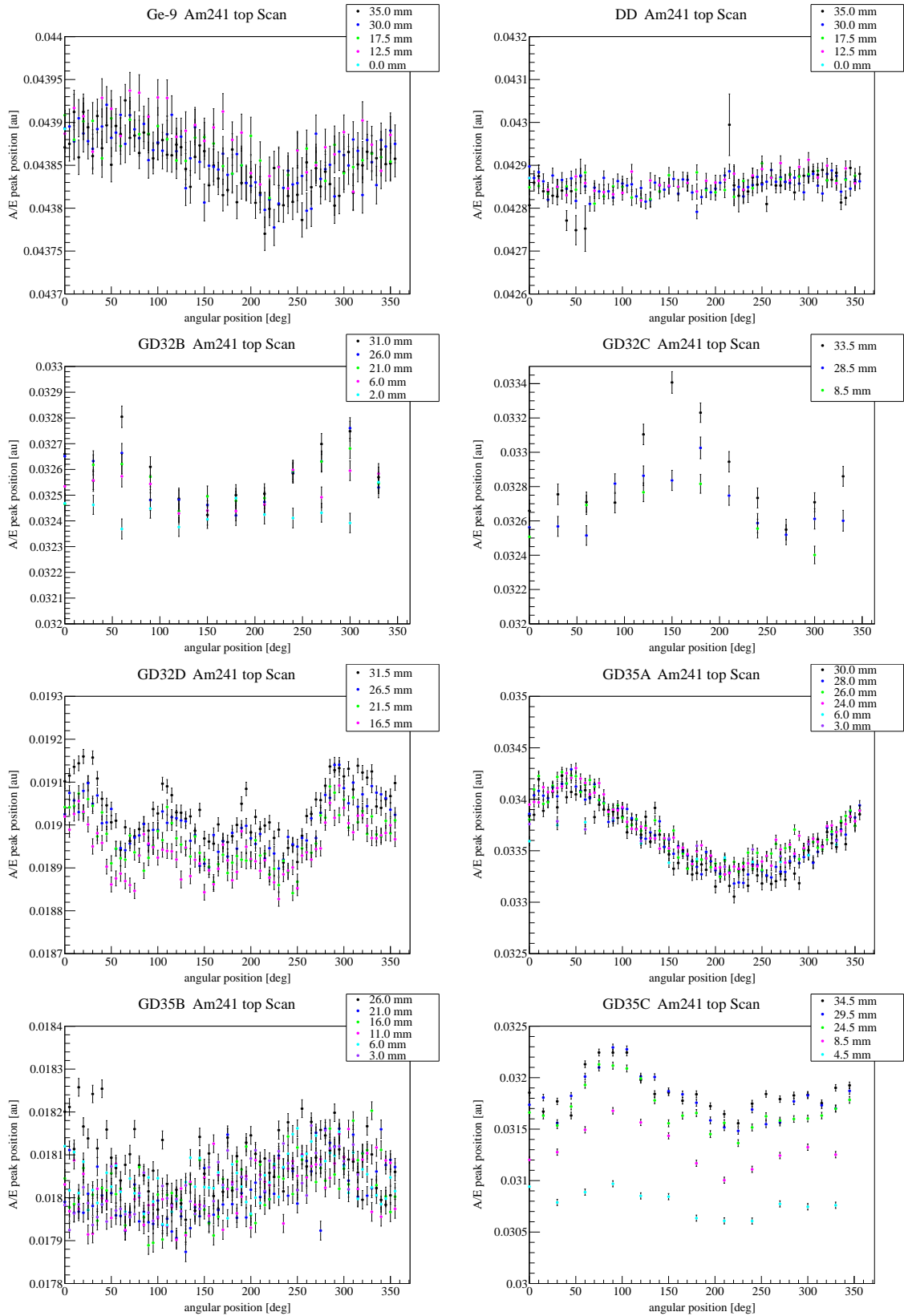
Figure 3.6: Results from the ^{241}Am top scans for six out of seven enriched, ^{depl}Ge-9 and ^{depl}DD BEGe detectors. The A/E peak position is shown as a function of angular position. The peak position is estimated by a Gaussian fit. Measurements were performed at different radii, which are indicated in color.
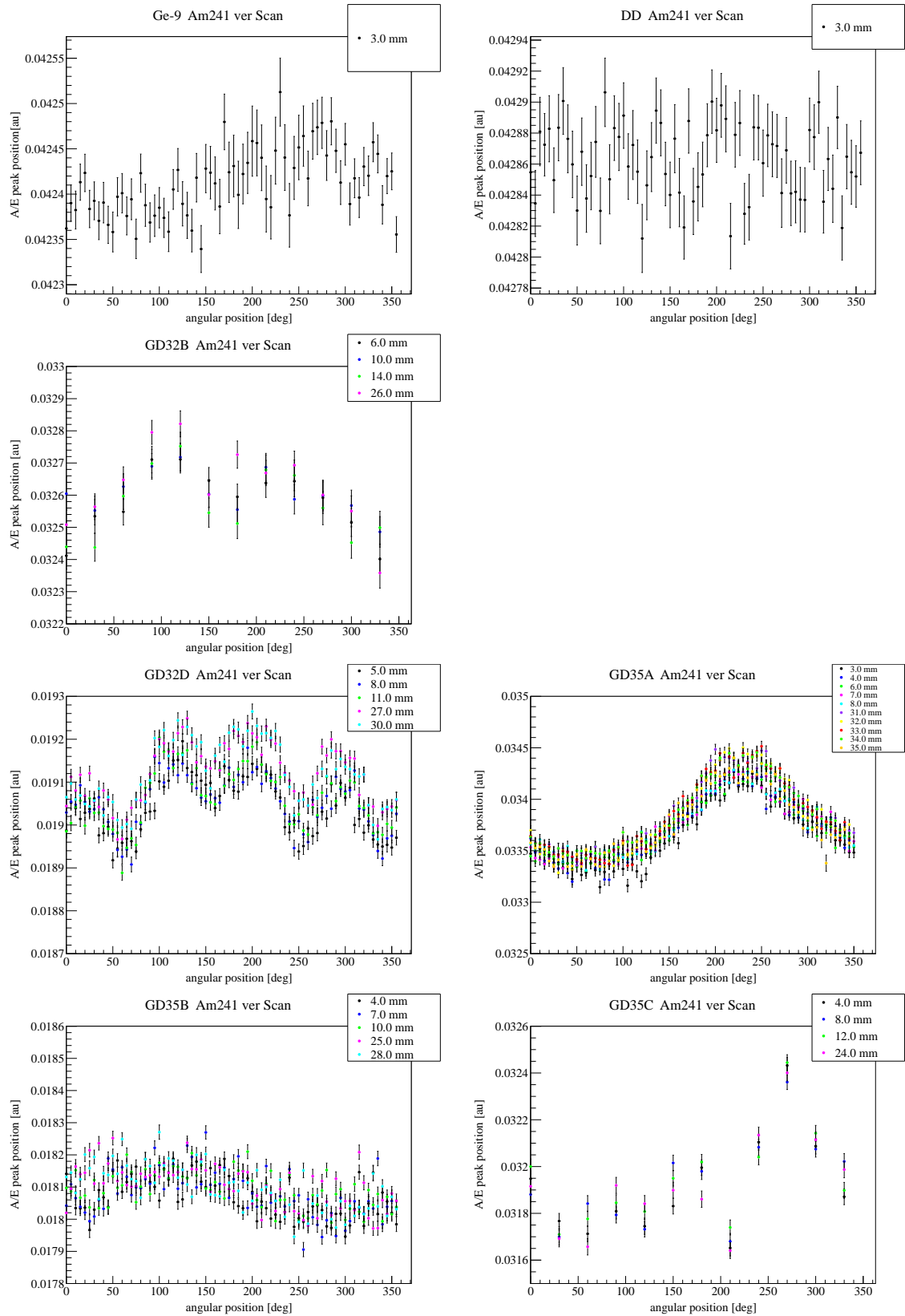
Figure 3.7: Results from ^{241}Am vertical scans six out of seven enriched, ^{depl}Ge-9 and ^{depl}DD BEGe detectors. No vertical scan was performed for GD32C. The A/E peak position is shown as a function of angular position. The peak position is estimated by a Gaussian fit. Measurements were performed at different distances to the top surface of the detector (corresponding to 0 mm), which are indicated in color. The angular position is shifted by 180° in comparison to the top surface scan

3.1.7 Reprocessing of Diodes

If the assumption is correction that the "A/E Anomaly" originates in surface effects the pulse shape performance should be influenced by a surface treatment and the pulse shape performance should enhance compared to the performance before the treatment. Therefore, two of the enriched detectors, GD32C and GD32D, were sent to Canberra, Olen, where the passivation layer was renewed. In the procedure Canberra removed the old passivation layer, re-etched the groove and put on a new passivation layer.

GD32D I refers to GD32D before reprocessing, and GD32D II to the BEGe after reprocessing, respectively. The same holds for GD32C I and II.

PSD Efficiencies

^{228}Th measurements for PSA were repeated with GD32D II. Figure 3.8 compares the A/E dis-
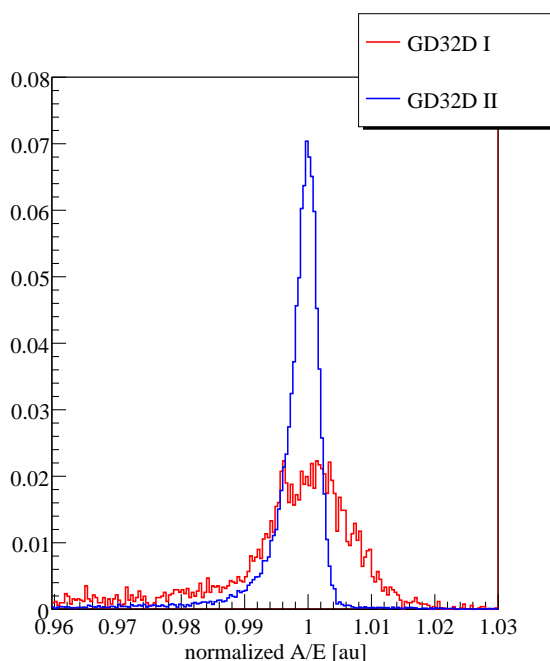

Figure 3.8: The normalized A/E distributions in the DEP for GD32D before (in red) and after (in blue) the mechanical and chemical surface treatment by Canberra, Olen.

tributions in the DEP before and after reprocessing. A significant improvement was achieved by the renewal of the passivation layer. The estimated resolution of the A/E distributions before the surface treatment was 1.6 % in the DEP, afterward 0.5 %. Table 3.7 summarizes the PSD efficiencies obtained before and after the surface treatment of GD32D. An improvement was achieved in discrimination efficiency although the number of surviving events before and after reprocessing are consistent within $2\,\sigma$ of the quoted uncertainties.

^{241}Am Surface Scans

The detailed ^{241}Am surface scans were repeated after the treatment of the detector groove. Figure 3.9 compares the angular distribution of A/E before and after reprocessing of GD32D: The A/E angular-dependence changed, before renewing the passivation layer the A/E peak

Energy region	GD32D I 15.03.12	GD32D II 27.04.12
DEP	0.900 ± 0.027	0.900 ± 0.012
FEP 1.6 MeV	0.181 ± 0.036	0.101 ± 0.007
SEP	0.142 ± 0.032	0.059 ± 0.004
FEP 2.6 MeV	0.217 ± 0.035	0.077 ± 0.001
2004-2074 keV	0.464 ± 0.036	0.376 ± 0.003
1989-2089 keV	0.466 ± 0.033	0.377 ± 0.003

Table 3.7: Comparison of PSD efficiencies before(I) and after(II) reprocessing of GD32D. The calibration with GD32D II ^{228}Th was not corrected for uncertainties due to low statistics in the DEP.
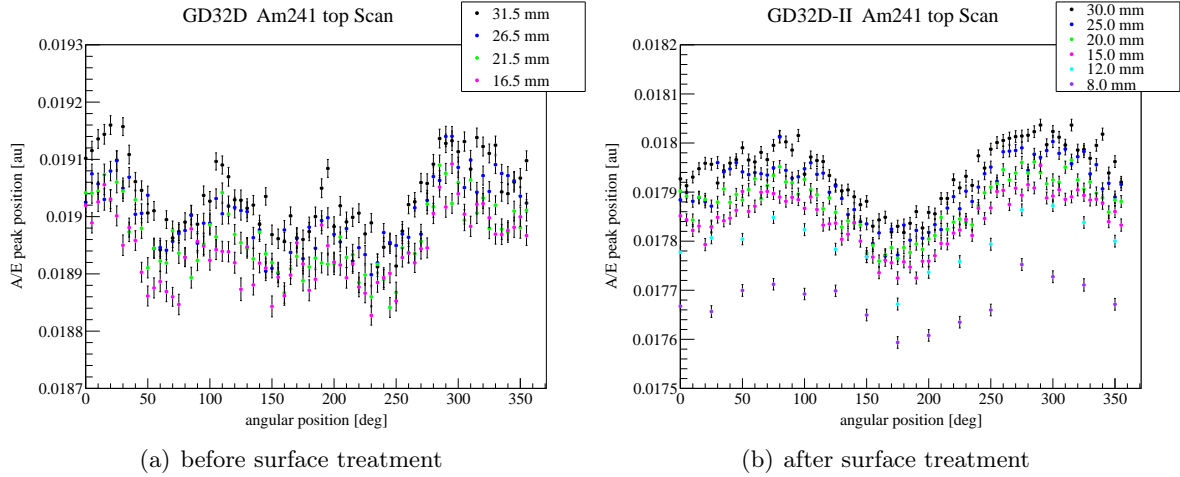

(a) before surface treatment   (b) after surface treatment

Figure 3.9: A/E peak position as a function of angular position measured for GD32D before and after reprocessing. Angles of GD32D I and GD32D II do not correspond.

position showed a 90° angular dependence, whereas afterwords the dependence is 180°.

For GD32D II additional measurement points were taken at a radius of 8 mm. The A/E values in this inner ring are lower in comparison to A/E values in higher radii. This confirms the assumption in Section 3.1.6 that the spread in A/E values is larger than the spread observed for GD32B and GD35B.

The mechanical and chemical treatment of the detector's surface showed an improvement in pulse shape performance. This is a strong hint that the so-called "A/E Anomaly'" is related to surface disturbances. The deterioration in PSD efficiency might partly originate in effects on the surface, such as charges in the groove.

However, in the case of GD23C, the reprocessing was not successful. After the surface treatment the detector showed a high leakage current and could not be operated in vacuum cryostat any further.

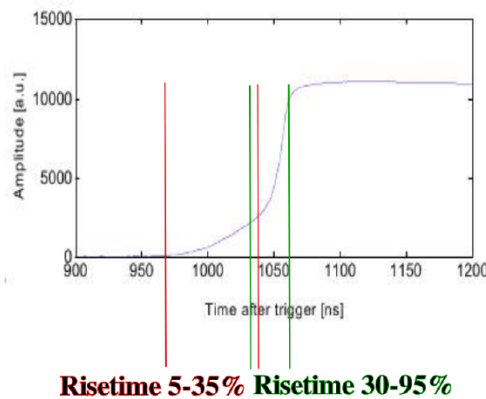### 3.1.8 Investigation of Risetime

Figure 3.10: The pulse's risetime is divided into two intervals: In red the time which is needed for the pulse to rise from 5 % to 35 % of its total height, in green from 30-95 % respectively. The risetime 5-35 % is sensitive to the drift through the main part of the crystal, whereas the risetime 30-90 % is more sensitive to the drift in strong weighting potential near the read-out electrode.

Besides the position-dependence of the pulse shape performance, the [241]Am surface scans from Section 3.1.6 can be used for further investigation of the crystal structure and the distribution of slow pulses as described in Section 1.2.3. Therefore, the rising pulse, the risetime was split into intervals defined by the height of the pulses' amplitude as in Figure 3.10:

1. Risetime 5-35 %, which is most sensitive to the crystal structure: It represents the main drift path through the crystal from the interaction point towards the middle slice of the crystal.

2. Risetime 30-95 % which presents the drift from the middle slice to the read-out electrode. It is most sensitive to charges which arrive delayed in strong weighting potential, i.e in the middle of the crystal, with respect to the bulk: Slow pulses.
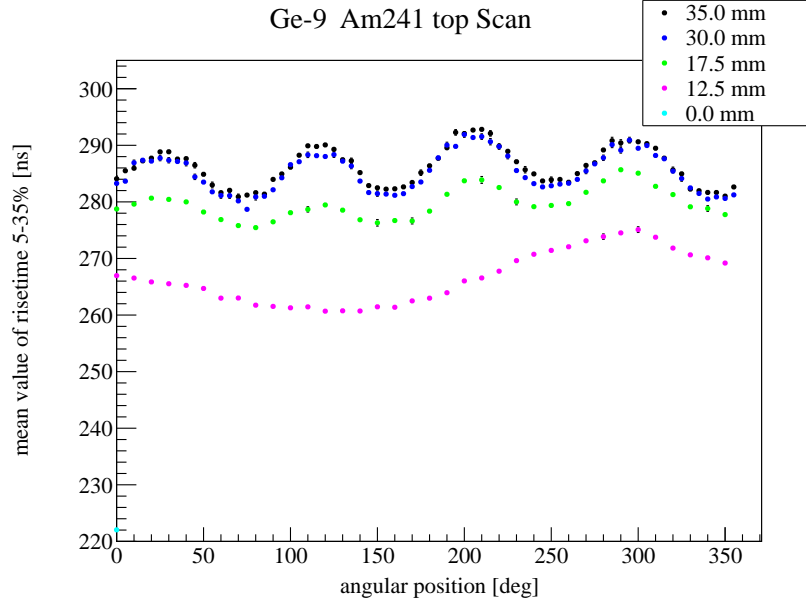
Risetime 5-35 %: Crystal Structure

Figure 3.11: Mean risetime 5-35 % in the 59.5 keV peak as a function of angular position measured with the ^{depl}Ge-9 BEGe detector.

To investigate the crystal structure the position dependence of the mean risetime 5-35 % in the 59.5 keV peak region was determined. Figure 3.11 shows exemplarily the mean risetime 5-35 % as a function of angular position measured with the ^{depl}Ge-9, the results for the enriched detectors and ^{depl}DD BEGe can be found in the Appendix B. The error bar is given by the mean error, i.e. $\frac{\sigma}{\sqrt{N}}$, where N is the number of events in the 59.5 keV peak region.

The radial dependence of Risetime 5-35 %
The mean risetime 5-35 % shows a strong radial dependence: It increases with increasing radius. This is expected as with increasing radii the drift length to the middle slice increases.

The angular dependence of Risetime 5-35 %
The mean risetime 5-35 % shows an angular dependence: In most of the detectors a clear 90 ° oscillation is observed which becomes less strong with decreasing distance to the center (top scans) or close to the read-out electrode (vertical scans). For the innermost rings in the top scan a weaker sinusoidal dependence with rather 360 ° period is observed.
The 90 ° oscillation in the mean risetime 5-35 % is due to the crystal axis [Aea10]. As shown in 3.11, the charge carriers' drift is influenced by the crystal structure. Germanium has a face cubic structure, i.e. three perpendicular crystal axis. The drift along the crystal axis is fastest if the electric field is parallel to a crystal axis. Thus, for a constant radius the risetime shows a sinusoidal angular dependence with a period of 180 °. The orientation of the axis coincides with the maximal in the risetime 5-35 % versus angle distributions. However, for a more precise determination more detailed investigation are necessary.
Some detectors do not show a clear sinus. This could be a hint, that the detectors are aligned

incorrectly. If the circles are not perfectly centered the drift length of the charge carriers is significantly different. Thus, would effect the mean risetime 5-35 % as it is very sensitive to the drift path of the charge carriers which are bend towards the middle of the crystal.
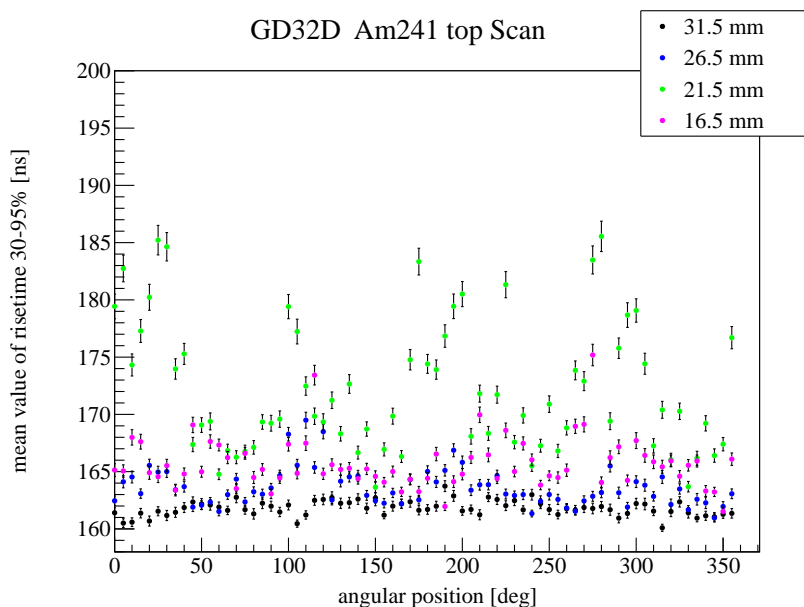

Figure 3.12: Mean risetime 30-95 % in the 59.5 keV peak of GD32D as a function of angular position.

Risetime 30-95 %: Slow Pulses

In order to study slow pulses the detailed ^{241}Am surface scans were analyzed for the position-dependence of risetime 30-95 %. In Figure 3.12 mean risetime 30-95 % of the 59.5 keV is shown exemplarily for GD32D. The risetime is represented by its mean value. The error bar is given by the mean error, i.e. $\frac{\sigma}{\sqrt{N}}$, where N is the number of events in the 59.5 keV peak region. A summary of the results for all detectors can be found in the Appendix B.

In GD32D particularly high risetimes are observed in some locations compared to the mean risetime of all measured positions. These points of high risetimes are mainly found in the ring at 21.0 mm radius to the center.

The A/E Distribution in Regions of High Risetime

The A/E distribution in regions with compatibly high risetime 30-95 % was investigated. Figure 3.13 (a) shows the A/E distribution in such a position: In addition to the main A/E peak, a second peak at lower A/E values is observed. Similar A/E distributions are found in all measured positions of GD32D, with variating strength of the satellite peak .

Investigation of the main and satellite A/E peaks show that they originate from two different population of pulses: "Normal" and slow pulses. Figure 3.13 (b) shows the risetime 30-95 % distribution corresponding to the marked A/E ranges in Figure 3.13 (a). In blue the risetime distribution of events in the main A/E peak are shown. The red risetime distribution of events in the satellite peak shows that the A/E satellite peak originates from slow pulses.

Similar high fraction of slow pulses present in the 59.5 keV peak was found for GD35A and
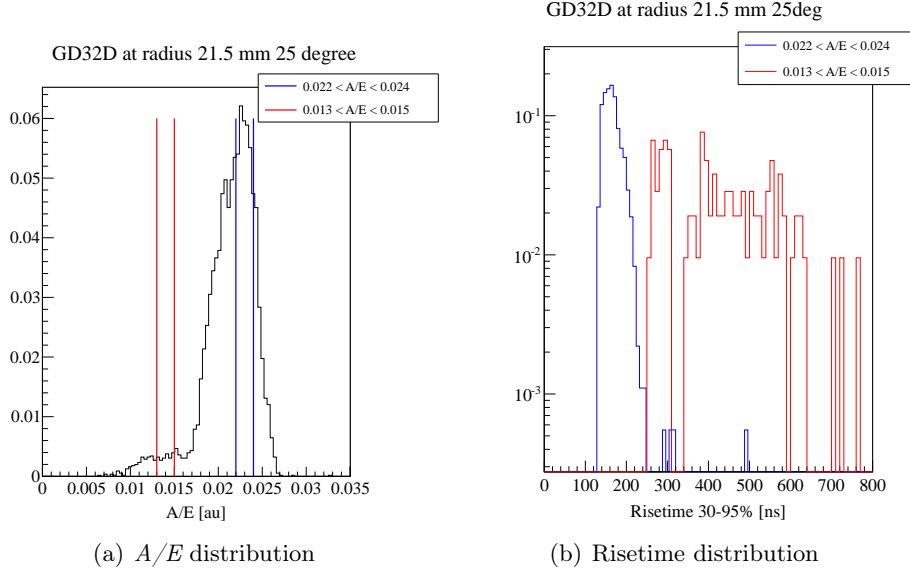
(a) A/E distribution

(b) Risetime distribution

Figure 3.13: (a): A/E distribution in the 59.5 keV peak of GD32D with the collimated source at 21.5 mm radius and $25\,°$ on top of the detector. Only events in a $4.5\,\sigma$ range of the 59.5 keV are taken into account. (b): Corresponding risetime 30-95 % distribution for the two indicated A/E ranges. The integrals of the A/E and risetime 30-95 % distributions are normalized to unity.

GD35B as well.

The behavior of is GD32D, GD35A and GD35B is unexpected, as a high number of slow pulses should be shifted towards lower energies, thus should not be present in the full energy peak. Further investigation of the unusual amount of slow pulses involved

- the position-dependence of the dead layer thickness, represented by the count rate, and

- the energy distribution of the slow pulses.

The Eventrate in the 59.5 keV peak

Regions of high risetime show an increasing event rate. The correlation is shown in Figure 3.14 for GD32D. Therefore, positions with a high fraction of slow pulses in the 59.5 keV peak should have a thinner dead layer than other positions in the crystal.

The Energy Distribution of Slow Pulses

The energy distribution of the slow pulses was investigated in order to answer the question why in some regions a high fraction of slow pulses is observed in the FEP. The risetime 30-95 % as a function of uncalibrated energy for a position that shows only few slow pulses in the 59.5 keV peak is shown in Figure 3.15(a). The energy and risetime distribution of slow pulses is rather continuous.

On the other hand, Figure 3.15(b) shows the risetime 30-95 % as a function of uncalibrated energy in a region with a high fraction of slow pulses. The distribution is much less continuous than in Figure 3.15(a). The energy of the slow pulses is shifted towards higher energies.
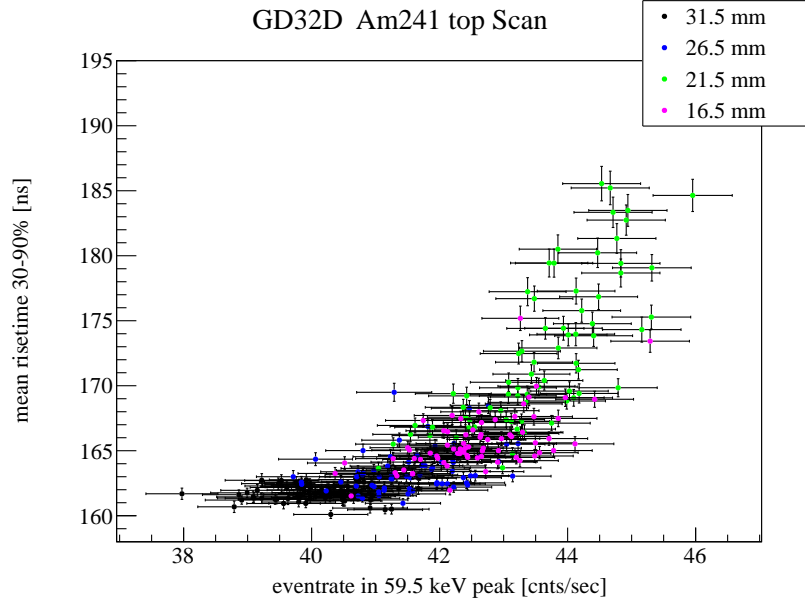
Figure 3.14: Event rate as a function of risetime 30-95 % in the 59.5 keV peak for GD32D. The detector shows a compatibly high fraction of slow pulses in the peak.

Moreover, the dependence of the energy from the risetime seems less strong than for the measurement in (a).

The denser concentration of risetime every 140 ns is due to noise at this period.

Figure 3.16 shows the energy distributions of the slow pulses corresponding to Figures 3.15 (a) in blue and (b) in red. The slow pulses have been selected by a cut on the risetime which was determined by fitting the risetime distribution of the 59.5 keV peak and choosing the cut to be the mean value plus 2σ of the Gaussian. The blue distribution is constant before the beginning of the peak whereas the red distribution rises towards the peak.

The investigation of the energy distribution of the slow pulses leads to the assumption that in some positions of the detector slow pulses loose less energy in the transition layer. Therefore, the slow pulses are observed in the 59.5 keV peak [Sal12].

Similar behavior has been found for GD35A and GD35B, which show a high fraction of slow pulses in the 59.5 keV peak.

The results obtained from investigation of slow pulses in the ^{241}Am surface scans might be an indication that the dead layer is thinner in the regions with a high fraction of slow pulses in the peak. However, this is still under investigation. Detailed Monte Carlo Simulation are needed for further conclusion and understanding of the origin.

(a) less amount of slow pulses in FEP

(b) high fraction of slow pulses in FEP
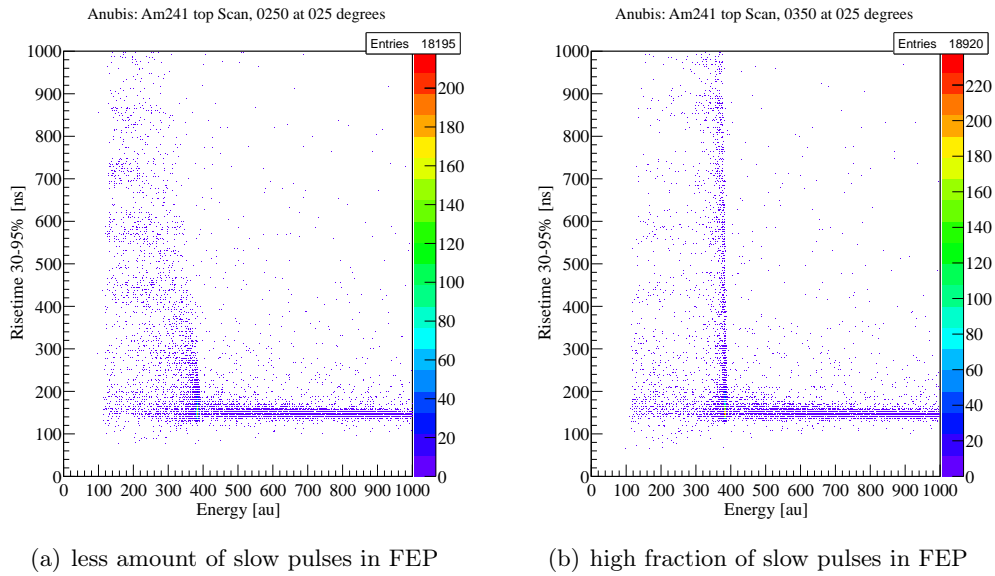
Figure 3.15: The risetime 30-95 % as a function of uncalibrated energy is shown measured in a position (a) with a few slow pulses in the FEP and (b) a high fraction of pulses in the FEP.
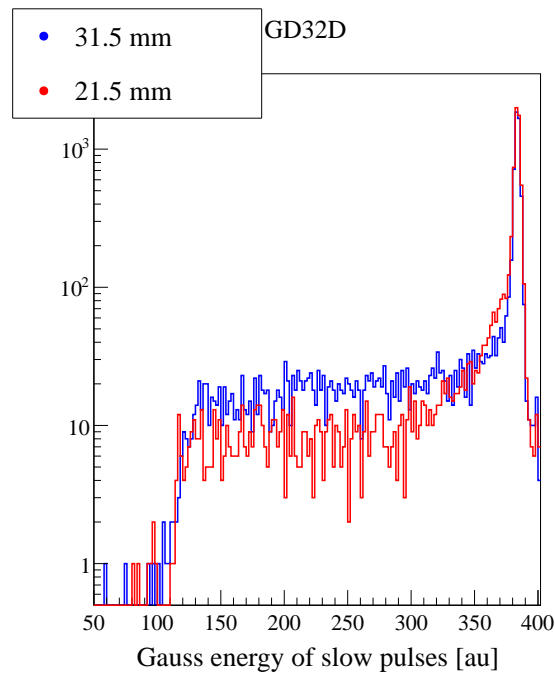

Figure 3.16: The energy distribution of the slow pulses from Figure 3.15 (a) and (b). The red distribution represents a position with a high fraction of slow pulses in the 59.5 keV peak.

3.1.9 Summary of Pulse Shape Performance in Vacuum Cryostat

The PSD efficiencies obtained in Section 3.1.1 show that the A/E analysis as developed in [Bud09] is a working active background suppression technique for the new enriched GERDA Phase II BEGe diodes.

Two out seven enriched BEGe detectors,GD32B and GD35B, show pulse shape discrimination efficiencies compatible to the depleted prototype BEGe detectors. The discrimination efficiency in the single escape peak (SEP) is 5.4 % on average, in the ROI 32.2 %, respectively. Five out of seven enriched diodes show a deteriorated pulse shape discrimination efficiency in comparison to the prototype BEGe diodes. On average the PSD efficiency in the SEP is 10.5 %, in the region (2039±50) keV it is 42.0 % for these five diodes, compared to a discrimination efficiency of 5.7 % in the SEP and 32.4 % in the region (2039±50) keV achieved with the prototypes.

The deterioration of pulse shape performance is be related to the A/E distribution. Three of the enriched BEGe detectors, GD32A, GD32D and GD35A, with worse PSD performance show significantly broader A/E distributions in the DEP compared to depleted BEGe diodes. Two detectors with deteriorated PSA performance, GD32C and GD35C, show a double structure in the A/E distribution.

Investigation of the DAQ, electronics and analysis chain lead to the conclusion that the observed "A/E Anomaly" originates from the diodes themselves, i.e. from the distortion of the intrinsic electric field which would lead to a position-dependence of the A/E values. The leading working hypothesis are surface charges, e.g. in the passivation layer of the groove, which would change the electric field inside the diode. Furthermore, local differences in impurity concentration, undepleted spots or defects in the crystals might distort the intrinsic electric field of the diode.

In surface scans with a collimated ^{241}Am source the position-dependence of A/E was investigated. It is observed that detectors with better pulse shape performance, have position-dependence of A/E smaller than 1 %. The five detectors with compatibly worse pulse shape performance show a stronger dependence of A/E on the position of energy deposition.

In high voltage scans with collimated ^{241}Am source the hypothesis of undepleted spots which could lead to a position-dependence of A/E was investigated. However, in the HV scans no hint is found that the diodes are not fully depleted.

However, no correlation between the position-dependence of A/E and the structure of the A/E distribution in the DEP is found.

In the attempt to improve pulse shape performance, two diodes were sent to the manufacturer Canberra for mechanical treatment of the surface. The passivation layer was renewed in order to remove possible charges in the groove that could distort the intrinsic electric field of the diodes. The chosen diodes were GD32D and GD32C. For GD32D a significant improvement in pulse shape performance is observed. The discrimination efficiency in the SEP improved from 14.2 % to 5.9 %, in the region of interest of $Q_{\beta\beta}$ of ^{76}Ge at 2039 keV from 46.5 % to 37.7 %.

This is a strong hint that the observed "A/E Anomaly" originates at least to some extend from surface effects. However, GD32C showed high leakage current after the surface treatment such that the diode could not be operated any longer in vacuum cryostat.

So far, there is no clear picture why only two out of seven enriched BEGe detectors operated in vacuum cryostats have a compatible PSD performance as depleted prototype BEGe detectors. There is no doubt that the deteriorated pulse shape performance is related to the observed "A/E Anomaly" which in turn is related to the position-dependence of A/E. All investigation indicate that the "A/E Anomaly" originates in surface effects, however, further contributions from intrinsic effects cannot be rejected. The origin of the observed structures in the A/E distribution in vacuum cryostat is still under investigation. For further understanding detailed Monte Carlo simulations are needed. This should help to interpret the observed A/E distributions.

In further investigation of the deterioration of pulse shape performance by surface effects, measurements of the enriched BEGe detectors operated in LAr with and without passivation were performed. The results will be presented in Section 3.2.

Independently from the A/E studies, the detailed ^{241}Am surface scans were investigated in terms of the pulse's risetime. If the detectors are aligned correctly, the orientation of the crystal axis can be determined by the drift time of the charge carriers. Furthermore, three enriched BEGe diodes show a high fraction of slow pulses in the FEP. Indications are found that the dead layer of these three detectors is thinner in some regions of the diode surface. Future Monte Carlo simulation shall give a better understanding of the observed.

3.2 Performance in LAr

For investigation of the influence of possible surface charges in the groove on the pulse shape performance, the passivation was removed for two enriched BEGe diodes. The diodes were tested in GDL at LNGS. The results obtained in GDL with the two enriched BEGe diodes on pulse shape performance will be presented in Section 3.2.1 and compared to the performance in vacuum cryostats.

Furthermore, five enriched BEGe detectors were installed into GERDA. The main goal was to check for any contamination of the new diodes as well as the overall performance in the LAr cryostat. At this stage the passivation layer was not removed from the groove. This will be done before the beginning of GERDA Phase II as tests in the past showed that removing the passivation layer from the diodes suppresses leakage current that might appear during the operation in LAr [Hei09]. The PSA performance of the enriched BEGe detectors in the GERDA cryostat is studied and compared to the performance in vacuum cryostat in Section 3.2.2. Finally, in Section 3.2.3 the feasibility of the pulse shape cut for active background suppression in GERDA will be demonstrated.

3.2.1 Performance with and without Passivation Layer

(a) enriched BEGe diode GD32A

(b) enriched BEGe diode GD35A
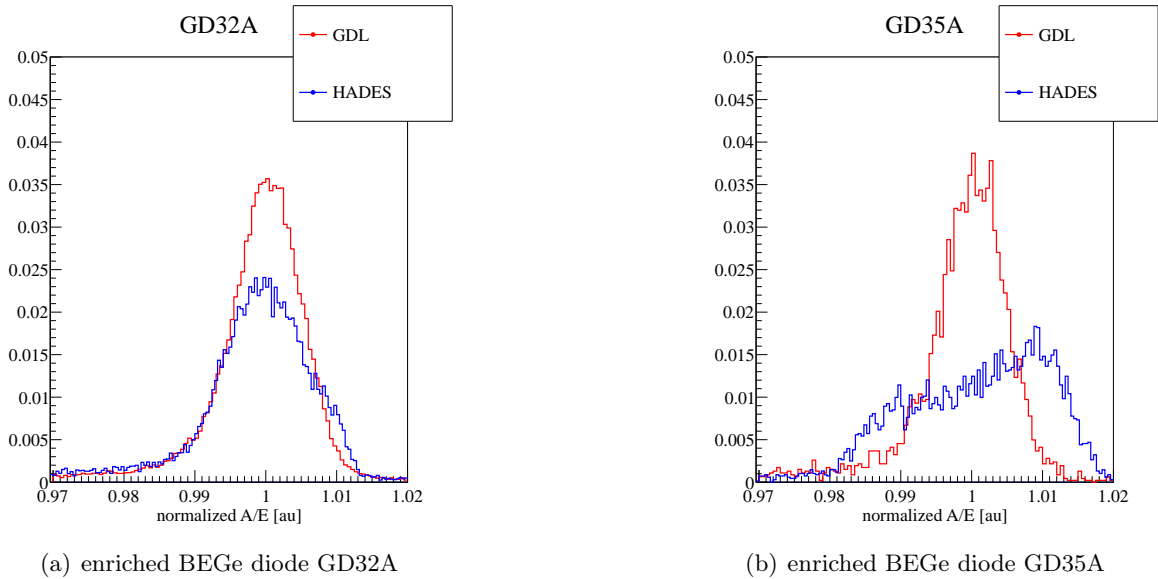
Figure 3.17: Comparison of the A/E distributions measured in LAr with passivation layer (HADES) and in vacuum cryostat without passivation layer(GDL) for GD32A and GD35A. A/E peak positions are normalized to 1, the integrals to unity.

D. Budjas and K. Gusev performed measurements with three BEGe detectors in LAr in the Germanium Detector Laboratory (GDL) at LNGS:

- GD32A without passivation layer

- GD35A without passivation layer

- BEGe 13050: natural BEGe detector with thin passivation layer

Figure 3.18: Comparison of the A/E distributions in the DEP of the enriched BEGe detectors GD32A and GD35A without passivation layer and the natural BEGe 13050 with thin passivation layer. A/E peak positions are normalized to 1, the integrals to unity.

The natural BEGe detector was used for a direct comparison of PSA performance with and without passivation layer using the same electronics and DAQ system.

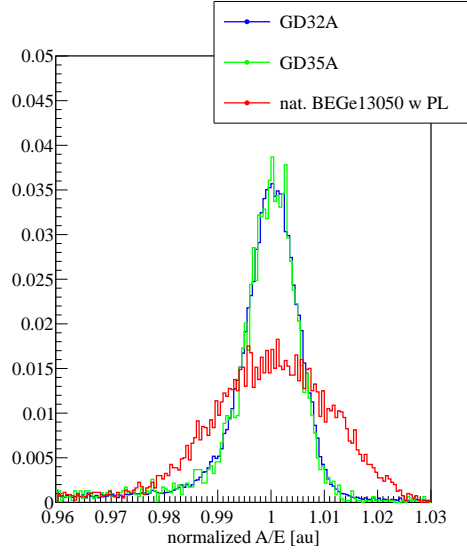### A/E distributions with thin and without Passivation Layer

Figure 3.17 shows the direct comparison of the A/E distributions of GD32A and GD35A with passivation layer operated in vacuum cryostat and without passivation layer operated in LAr. A clear improvement is observed when the passivation layer is removed. With passivation layer (i.e. measured at HADES in vacuum cryostat) the A/E resolution of GD35A was determined to 2.20 %, without passivation the A/E resolution is 1.17 %, see Table 3.8. In the case of GD32A, the A/E resolution improved from 1.46 % to 1.21 %.

This observation is further strengthened by the fact that the A/E distribution of the BEGe detector with thin passivation is significantly broader than the A/E distribution of the BEGe detector without passivation layer (compare Figure 3.18 and Table 3.8). As all three diodes were tested under the same measurement conditions, the difference in A/E distributions with and without passivation layer is a strong hint that the surface might effect the A/E parameter, i.e. pulse shape performance.

PSD Efficiencies with and without Passivation Layer

The PSD efficiencies with (HADES) and without (GDL) passivation layer for GD32A and GD35A are compared in Table 3.9. For GD32A a clear improvement in pulse shape performance without passivation layer is observed.

In the case of GD35A the collected statistics in the ^{228}Th measurement was very low, such that no clear statement about the PSD efficiency can be made. However, the A/E resolution is improved by the removal of the passivation layer, thus, an improvement in PSD efficiency is expected as well.

	PL	Resolution of	
		energy in 2.6MeV [keV]	A/E in DEP [au]
		BEGe1350	
GDL	w	3.9 keV	2.61%
		GD32A	
GDL	w/o	3.9 keV	1.21%
HADES	w	2.4 keV	1.46%
		GD35A	
GDL	w/o	4.2keV	1.17%
HADES	w	2.4 keV	2.20%

Table 3.8: A/E resolution for the enriched BEGe detectors GD32A and GD35A measured in HADES (i.e. with passivation layer in vacuum cryostats) and GDL (i.e. without passivation layer in LAr). For comparison the A/E resolution of a natural BEGe detector with thin passivation layer was measured in GDL. All three detectors are measured with the same electronics and DAQ. The A/E resolution is given as the FWHM/(A/E peak position) which is estimated by a Gaussian fit of the A/E distribution. The energy resolution is the peak sigma in keV.

PSD efficiencies for GD32A		
	GDL	HADES
DEP	0.900 ± 0.024	0.900 ± 0.013
FEP 1.6 MeV	0.150 ± 0.032	0.180 ± 0.020
SEP	0.082 ± 0.015	0.121 ± 0.012
FEP 2.6 MeV	0.115 ± 0.011	0.163 ± 0.012
2004-2074 keV	0.380 ± 0.031	0.427 ± 0.019
1989-2089 keV	0.380 ± 0.030	0.427 ± 0.018

PSD efficiencies for GD35A		
	GDL	HADES
DEP	0.900 ± 0.048	0.900 ± 0.023
FEP 1.6 MeV	0.195 ± 0.209	0.128 ± 0.013
SEP	0.085 ± 0.208	0.078 ± 0.013
FEP 2.6 MeV	0.116 ± 0.268	0.132 ± 0.012
2004-2074 keV	0.415 ± 0.210	0.400 ± 0.021
1989-2089 keV	0.410 ± 0.212	0.395 ± 0.020

Table 3.9: Comparison of the PSD efficiencies obtained with (HADES) and without (GDL) passivation layer. In the case of GD35B the uncertainties are over estimated.

3.2.2 Performance in GERDA LAr Cryostat

To derive the pulse shape performance of the enriched BEGe diodes in the GERDA LAr cryostat the ^{228}Th calibration in Table 2.2 are investigated. No difference in A/E or energy was observed in calibration no.1 and no.2. Therefore, the two measurements were combined in order to increase statistics.

Unfortunately, A/E is not stable in time over a long period. Figure 3.20 shows the A/E distributions of the BEGe detectors for the first five ^{228}Th calibrations in GERDA. The A/E peak positions are different for different calibrations. The highest shift is observed in the topmost detector, GD32B. In Appendix C the A/E peak positions and the relative shift of the calibrations are summarized in a table.

If the drift in A/E peak position originates in the DAQ, the same behavior should be observed
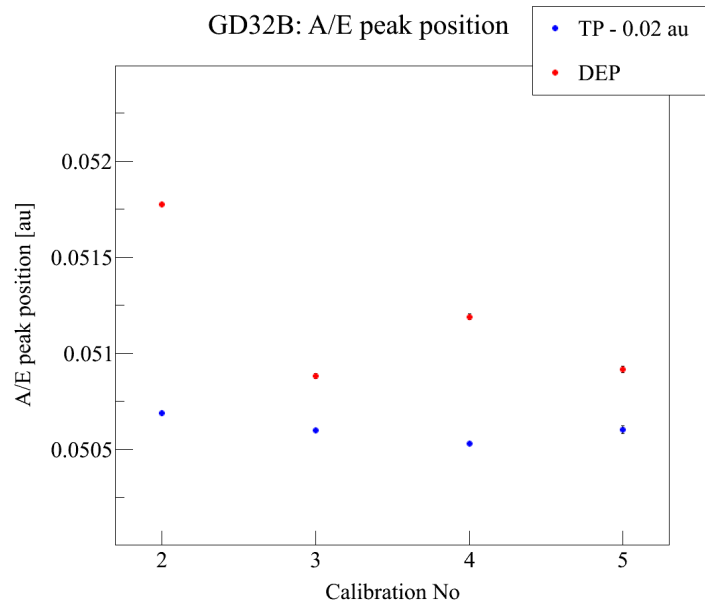

Figure 3.19: A/E peak position of the test pulse (TP) and the DEP measured with GD32B for the first five calibrations in GERDA, see Table 2.2. the first two calibrations are combined as no shift was observed.

in the A/E of the test pulse (TP) which is connected to the detector's read-out electronics. Figure 3.19 shows exemplary for GD32B the A/E peak position of the DEP compared to the A/E of the TP. It is observed that the A/E of the TP changes in time but the shift is not correlated to the detector's drift in A/E peak position. The same behavior is observed for the other four BEGe detectors.

Due to the unknown origin of the shift, the PSA performance in LAr was investigated using only the combined calibrations 1 and 2 from Table 2.2.

The A/E distributions

Figure 3.21 shows the comparison of the A/E distributions measured in vacuum cryostat (HADES) and in LAr (GERDA). The figure demonstrates that the A/E distribution in the LAr is different compared to the A/E distribution measured in vacuum cryostat:
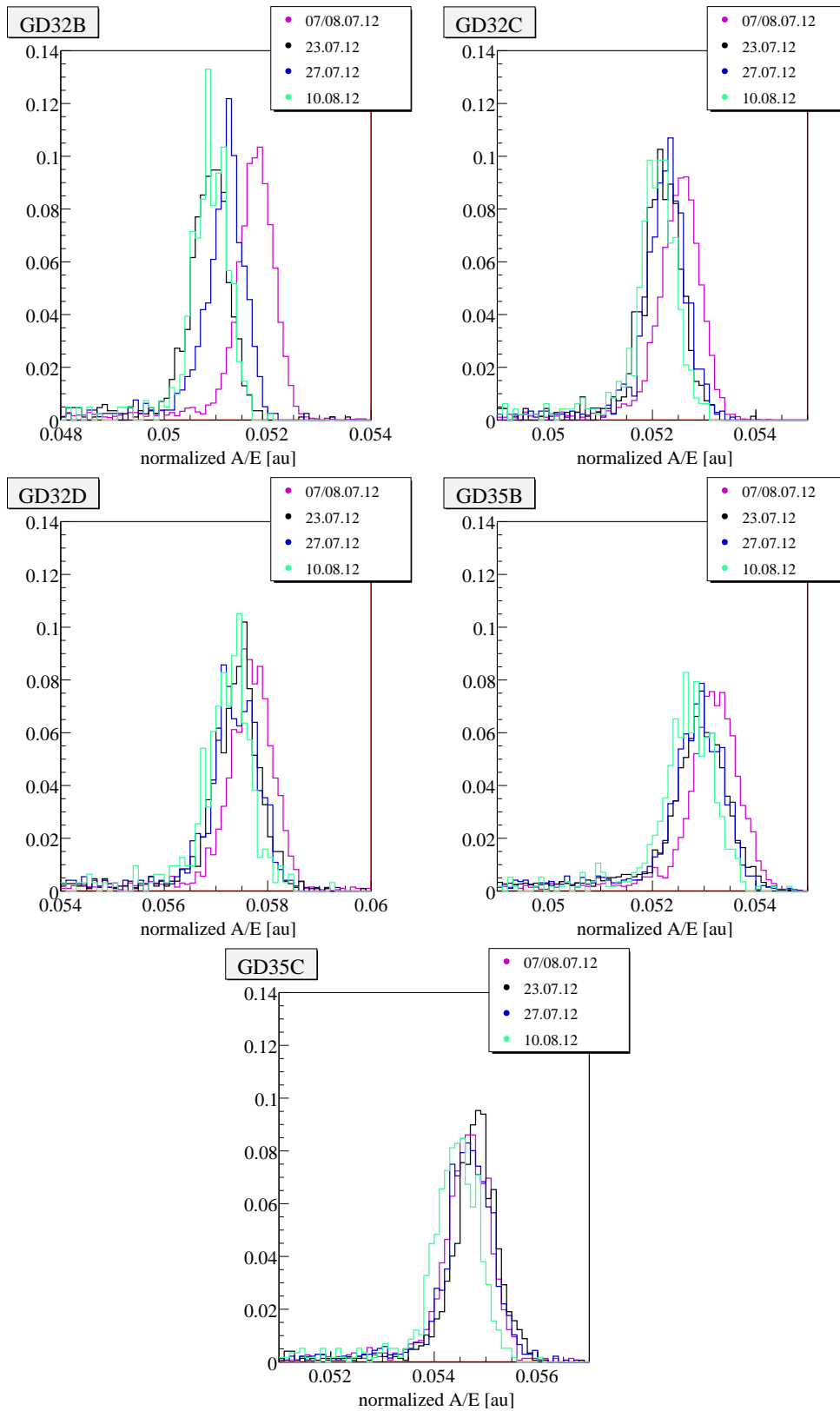
Figure 3.20: *A/E* distributions of the first five ^{228}Th calibrations taken with the enriched BEGe detectors in the GERDA LAr cryostat. The integral of the *A/E* distributions are normalized to unity. the first two calibrations were combined.

Detector	A/E resolution in DEP		FWHM at 2.6 MeV [keV]	
	GERDA	HADES	GERDA	HADES
GD32B	1.5 %	0.8 %	2.94 ± 0.02	2.04 ± 0.02
GD32C	1.7 %	1.3 %	2.85 ± 0.02	2.46 ± 0.01
GD32D	1.6 %	1.6 %	3.00 ± 0.03	2.41 ± 0.02
GD35B	1.9 %	0.6 %	3.99 ± 0.04	2.45 ± 0.02
GD35C	1.7 %	1.7 %	3.22 ± 0.04	2.41 ± 0.02

Table 3.10: Comparison of the A/E distributions in the DEP and the energy resolution in the FEP 2.6 MeV for measurements in vacuum cryostat (HADES) and LAr (GERDA). The A/E resolution is given as the FWHM/peak position where width and peak position are estimated by a Gaussian fit.

1. The two BEGe detectors, which showed a double structure in the A/E distribution in vacuum cryostat, GD32C and GD35C, do not show such behavior in LAr.

2. Furthermore, the A/E distributions of all five BEGe detectors are similarly broad in LAr.

Table 3.10 expresses this in numbers: The A/E as well as the energy resolution is worse in LAr (GERDA) than in vacuum cryostat (HADES). The reason for the lower PSA performance is partly due to the higher level of noise in GERDA compared to HADES which is reflected in the relatively poorer energy resolution in GERDA. However, the A/E distribution might additionally be influenced by surface charges.

The PSD Efficiencies
Table 3.11 summarizes the PSD efficiencies for the first two calibrations of the BEGe detectors in the GERDA LAr cryostat. All five BEGe detectors show poorer pulse shape performance in LAr than in vacuum cryostat: In the case of GD32B, for example, the PSD efficiency in the SEP deteriorated from (5.1 ± 1.1) % to (11.0 ± 4.3) %. The discrimination efficiency in the region around $Q_{\beta\beta}$, 2039 keV was in vacuum cryostat (32.3 ± 2.1) %, in LAr it is determined to be (43.5 ± 6.9) %.

Pulse Shape Discrimination Efficiencies in LAr		
	GD32B	GD32C	GD32D
DEP of 2.6 MeV	0.900 ± 0.035	0.900 ± 0.033	0.901 ± 0.052
FEP 1.6 MeV	0.187 ± 0.024 ± 0.045	0.146 ± 0.024 ± 0.027	0.163 ± 0.043 ± 0.031
SEP of 2.6 MeV	0.110 ± 0.012 ±0.031	0.106 ± 0.011 ± 0.027	0.108 ± 0.019 ± 0.045
FEP 2.6 MeV	0.136 ± 0.002 ± 0.055	0.131 ± 0.002 ± 0.030	0.136 ± 0.003 ± 0.061
2004-2074 keV	0.434 ± 0.008 ± 0.061	0.440 ± 0.008 ± 0.040	0.448 ± 0.011 ± 0.072
1989-2089 keV	0.435 ± 0.007 ± 0.060	0.441 ± 0.006 ± 0.040	0.449 ± 0.009 ± 0.073

Pulse Shape Discrimination Efficiencies in LAr	
	GD35B	GD35C
DEP of 2.6 MeV	0.900 ± 0.055	0.900 ± 0.059
FEP 1.6 MeV	0.168 ± 0.040 ± 0.217	0.147 ± 0.066 ± 0.114
SEP of 2.6 MeV	0.120 ± 0.020 ± 0.214	0.128 ± 0.026 ± 0.125
FEP 2.6 MeV	0.164 ± 0.003 ± 0.269	0.172 ± 0.005 ± 0.168
2004-2074 keV	0.472 ± 0.011 ± 0.192	0.475 ± 0.015 ± 0.139
1989-2089 keV	0.472 ± 0.009 ± 0.191	0.479 ± 0.012 ± 0.140

Table 3.11: Pulse Shape Discrimination efficiency for the 5 BEGe detectors obtained with combined calibration 1 and 2 of Table 2.2. The given uncertainties are over estimated.
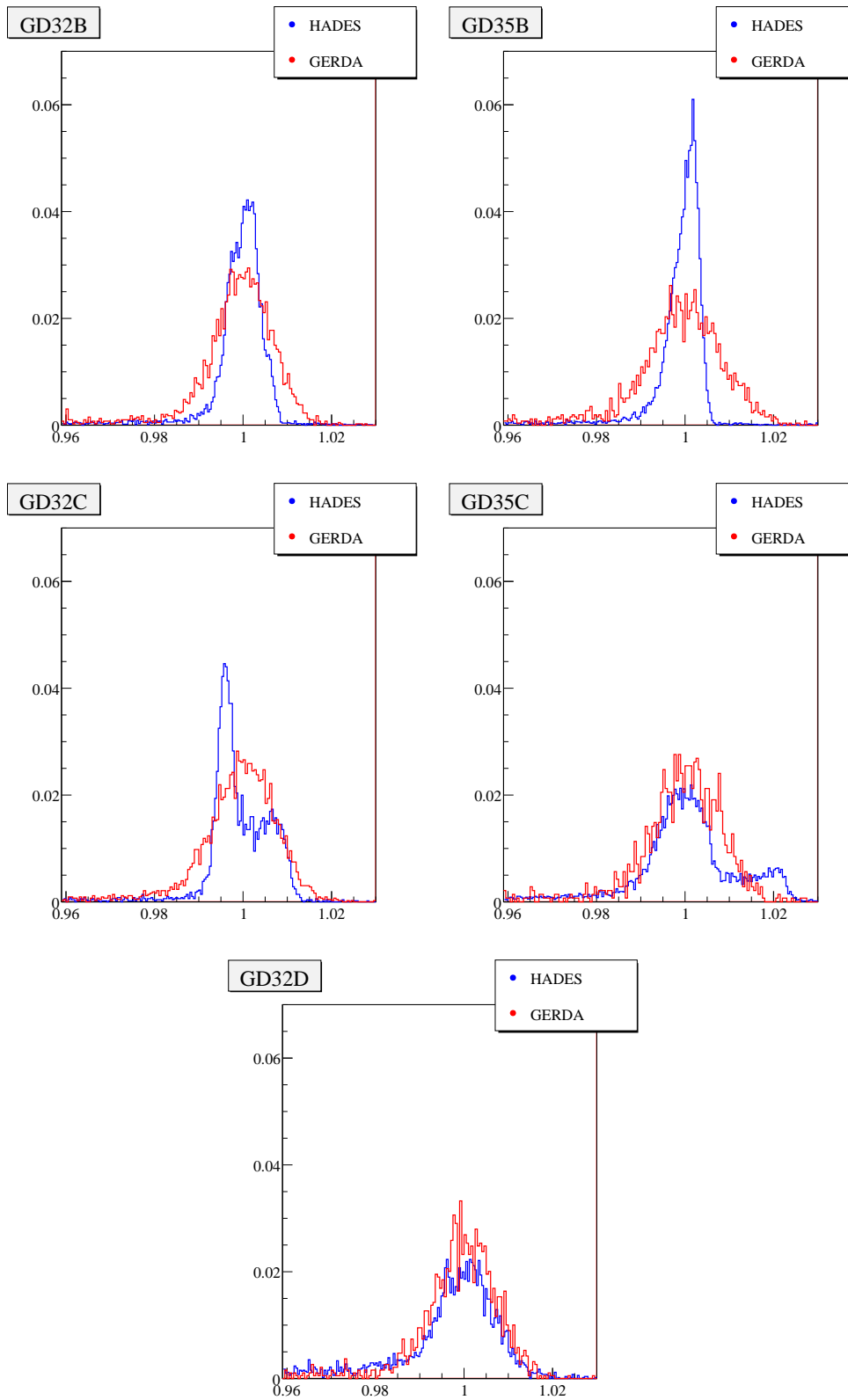
Figure 3.21: A/E distributions in vacuum cryostat (HADES) compared to the distributions measured in the GERDA LAr cryostat.

3.2.3 Application of PSA on GERDA Physics Data

The ^{228}Th calibrations in GERDA are rather short and the collected statistics respectively low (see Table 2.2). Therefore, several calibrations should be summed up in order to increase statistics in the DEP and to lower the statistical uncertainties.

In the following the ^{228}Th calibrations no.1 - no.4 of Table 2.2 are used to determine the A/E cut on GERDA physics data taken in between the calibrations. This time period corresponds to GERDA Run 35.

GD35C has been excluded from the physics analysis due to some unknown shift in energy, which gives an uncertainty of about $16\,\text{keV}$ in the ROI at $2039\,\text{keV}$. Therefore, GD35C will not be considered in the following.

Determination of the A/E cut for run 35

Figure 3.22 shows the A/E distributions in the DEP which was used for the calibration of the pulse shape cut. The distributions are slightly shifted and broadened in comparison to the A/E distributions of the first two calibrations, see Table 3.12. The corresponding acceptances in the DEP and the $Q_{\beta\beta}$ region of ^{76}Ge, $2039\,\text{keV}$, are summarized in Table 3.13.

The acceptance in the ROI is $47.1\,\%$ for GD32B, $43.9\,\%$ for GD32C, $45.5\,\%$ for GD32D and $49.1\,\%$ for GD35B. The uncertainties of the acceptances are big due to low statistics, but lowered in comparison to the uncertainties obtained with only two calibrations in Section 3.2.2.

Within the uncertainties the acceptance in the $Q_{\beta\beta}$ region are compatible with the acceptances obtained with the first two calibrations, no1. and no.2 in Table 3.11. Therefore, determining the A/E cut by a combination of Run 35 calibrations, is reasonable.

Relative resolution of A/E distribution in DEP			
	GD32B	GD32C	GD32D	GD35B
calibration 1+2	1.5 %	1.7 %	1.6 %	1.9 %
all calibrations	2.2 %	2.2 %	1.9 %	1.9 %

Table 3.12: Comparison of the A/E resolution in the DEP for the combined first two calibrations, no.1 and no.2 of Table 2.2, and the combination of the four calibrations during Run 35. The relative resolution of A/E is given as the FWHM/(A/E peak position) which are estimated by a Gaussian fit.

Comparison to the acceptance in vacuum cryostat

For GD32C and GD32D, the acceptances in the ROI obtained in Run 35 calibrations are within the uncertainties compatible to the acceptances achieved in vacuum cryostat. However, for GD32B and GD35B, the acceptances in LAr are significantly worse compared to vacuum cryostat tests: For GD32B the acceptance in the $Q_{\beta\beta}$ region in Run 35 calibrations was $47.1\,\%$ whereas in vacuum cryostat the obtained PSD efficiency was $(32.3\pm2.1)\,\%$. In the case of GD35B, in the GERDA LAr cryostat the acceptance in the ROI was $49.1\,\%$ compared to $(32.2\pm2.4)\,\%$ in vacuum cryostat.
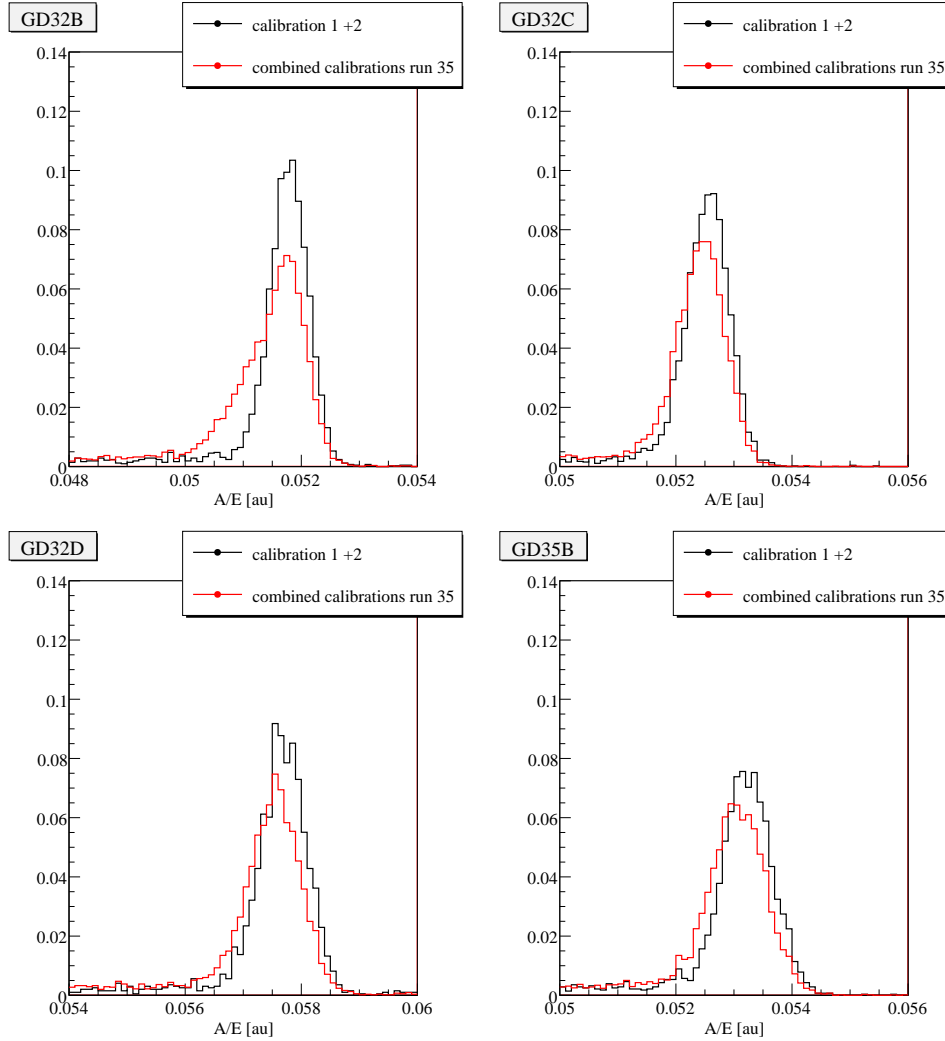
Figure 3.22: A/E distributions in the DEP for the combined Run 35 ^{228}Th calibrations in comparison to the first calibration in GERDA. GD35C has been excluded from the physics analysis. The integrals are normalized to unity.

Application of the A/E Cut on Physics Data in Run 35

Figure 3.23 shows in black the background spectrum which was measured with the four enriched BEGe detectors during Run 35 after applying the muon-veto-cut, the anti-coincidence-cut and quality cuts on the data using the software framework GELATIO [Aea11a].

In blue the black spectrum with an additional cut on low A/E values as determined in the pulse shape analysis introduced in Section 1.3 is shown. In red an additional cut on p$^+$-contact events with high A/E values was applied to the blue spectrum.

The comparison of the spectra with and without applied A/E cuts shows that a notable background suppression is achieved by pulse shape analysis.

The observed A/E distribution in the individual detectors is shown in Figure 3.25. For each BEGe diode the spectrum with corresponding A/E cuts and SSE line is shown.

determined acceptance from combined calibrations of Run 35			
	GD32B	GD32C	GD32D	GD35B
DEP	0.900 ± 0.030	0.901 ± 0.029	0.900 ± 0.040	0.900 ± 0.043
ROI	0.471 ± 0.039	0.439 ± 0.031	0.452 ± 0.067	0.487 ± 0.175

Table 3.13: Acceptance in the DEP and the ROI, (2039 ± 50) keV, obtained by the combination of the Run 35 ^{228}Th calibrations with the four BEGe detectors. GD35C has been excluded from the physics analysis. Uncertainties are probably overestimated.

Figure 3.24 shows the spectrum around the $Q_{\beta\beta}$ value of ^{76}Ge in a range of (2039 ± 400) keV. Before application of the A/E cut six events are observed within this region. Five of these events have A/E values well above or below the SSE line. The event with compatibly high A/E value is a possible ^{210}Po α-event, wheres the events with lower A/E values might be ^{42}K β-particles or multiple Compton scattered γ-rays (see discussion of PSA in LAr in Section 1.3). Five events are rejected by the A/E cut. The event at 1664 keV survives as its A/E value is close to the SSE line, i.e. the pulse shape of the event is single-event like.

Based on Poissonian statistics of six events collected in Run 35 a preliminary background index for the four enriched BEGe diodes can be determined. Before pulse shape analysis the background index in the $Q_{\beta\beta}$ region (2039 ± 360) keV including the blinded region is

$$BI = (2.000 - 10.358) \cdot 10^{-2} \frac{counts}{kg \cdot yr \cdot keV}$$

at 90 % C.L., calculated according to [Bea12].
The preliminary background index at 90 % C.L. estimated from Run 35 after applying the A/E cut is[3]

$$BI^{PSA} = (0.089 - 3.544) \cdot 10^{-2} \frac{counts}{kg \cdot yr \cdot keV} \quad .$$

The pulse shape discrimination technique clearly reduces the preliminary background index. However, statistics are very low and in a narrower energy range a significantly lower background index is expected. A further background suppression is expected by the LAr light instrumentation (see Section 1.1.2).

After the pulse shape analysis the given preliminary background index BI^{PSA} is within the GERDA Phase II design background index of $10^{-3} \frac{counts}{kg \cdot yr \cdot keV}$.

---

[3]we assume a loss in sensitivity of about 10 % according to the acceptance of 90 % in the DEP
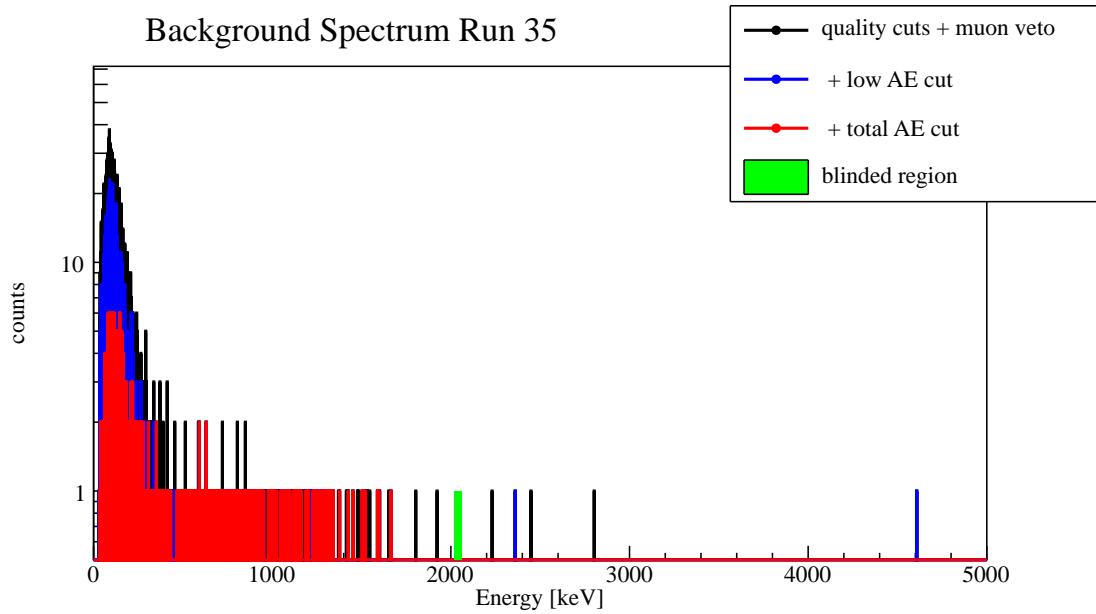
Figure 3.23: Energy spectrum obtained with the four BEGe detectors in GERDA Run 35: In black the spectrum of the events after application of the muon-veto, quality and anti-coincidence cuts is shown. To the blue spectrum the pulse shape cut on low A/E values was applied and the red an additional cut on high A/E values, i.e. p^+ contact events, respectively.
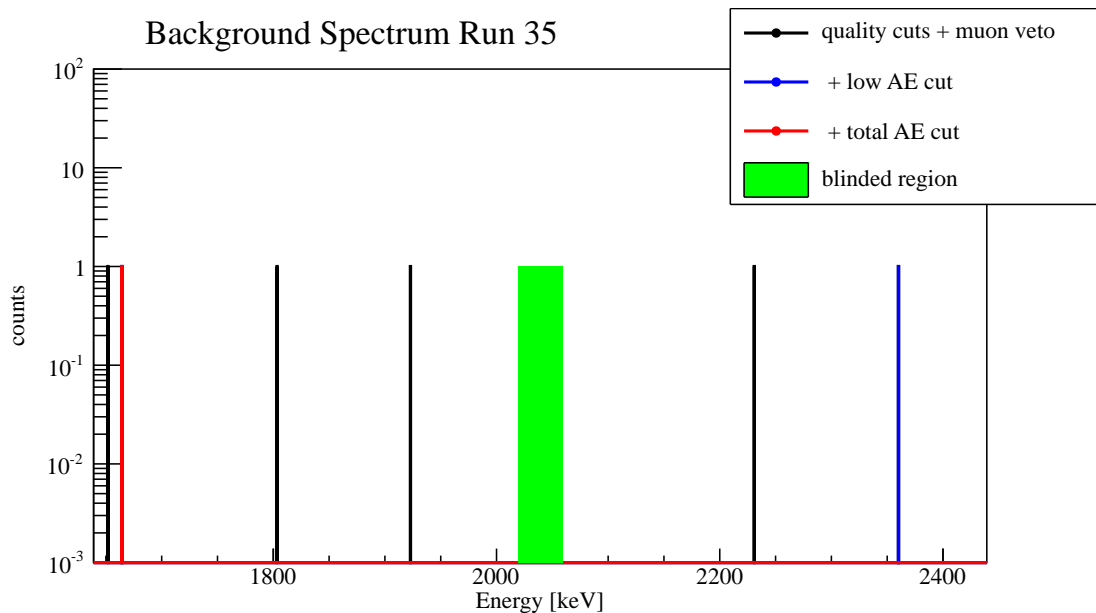

Figure 3.24: The energy spectrum shown in Figure 3.23 with selected energy range (2039 ± 400) keV. The data in the window (2039 ± 20) keV are blinded, i.e. not available for analysis.
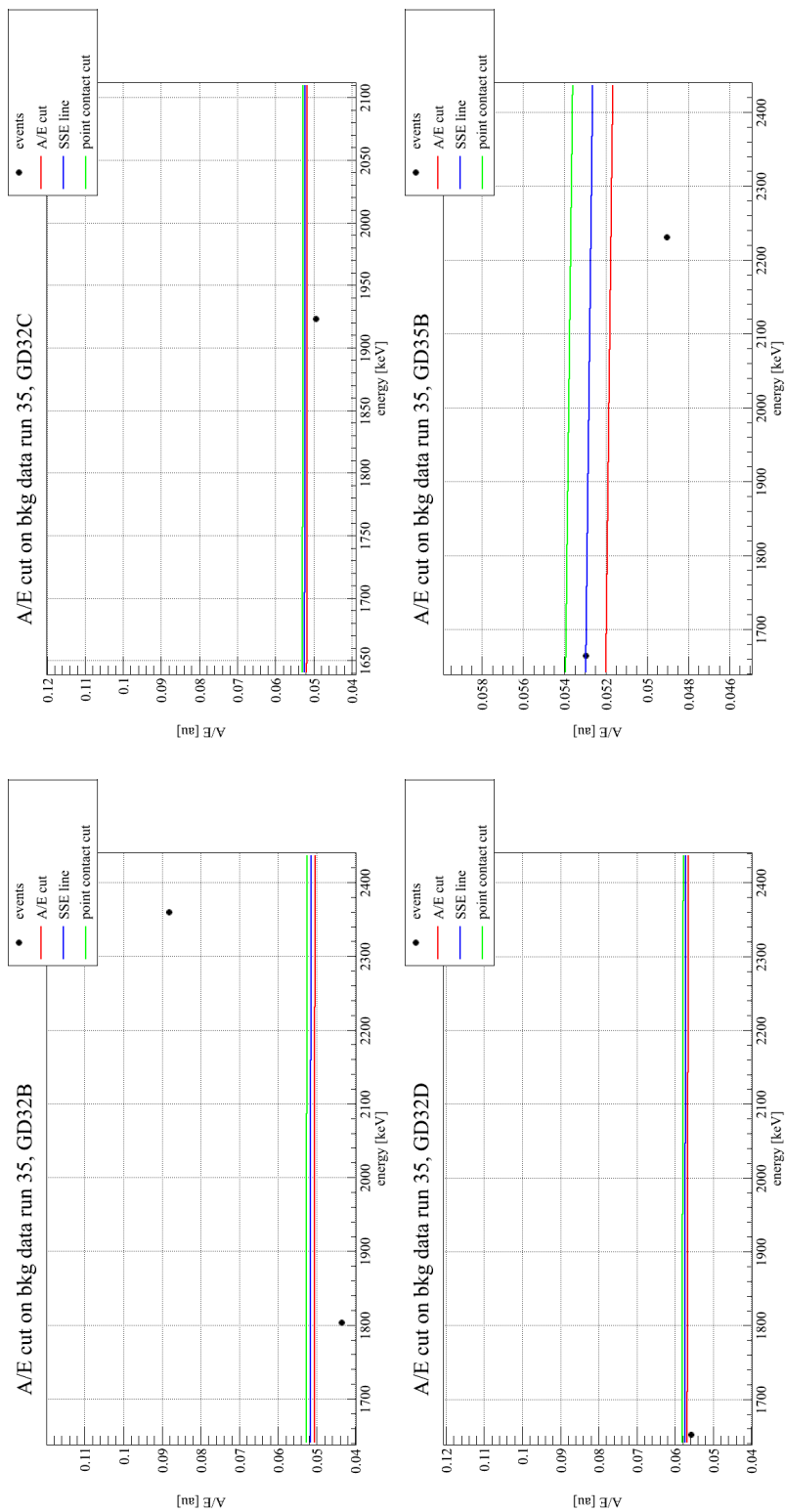
Figure 3.25: A/E distributions of the detected events in the region (2039 ± 400) keV in the enriched BEGe detectors in Run 35. The SSE-line (blue), the cut on low A/E values (red) and the cut on p^+ contact events (green) are shown. GD35C was excluded from the physics data analysis.

3.2.4 Summary of Pulse Shape Performance in LAr

The five enriched BEGe detectors show in general a good performance in the GERDA LAr cryostat. No contamination of the BEGe detectors has been observed. The energy resolution of the enriched BEGe detectors operated in GERDA is slightly worse than in vacuum cryostat but still a factor of about 2 better than for the coaxial detectors of Phase I.

The energy resolution in GERDA is lower compared to the obtained resolution in HADES. In the extreme case of GD35B, the FWHM of the 2.6 MeV peak was (2.41±0.02) keV in HADES, in GERDA the energy resolution is (3.99±0.04) keV. This is a hint for a higher level of noise plus longer distance of preamplifier/signal cables.

All five enriched BEGe detectors in GERDA have similar broad A/E distributions with a relative resolution of about 1.7 % on average. In the case of GD32B and GD35B the broadening of the A/E distribution is significant compared to the performance in vacuum cryostat. For example, the A/E resolution of GD35B deteriorates from 0.6 % in vacuum cryostat to 1.9 % in the GERDA LAr cryostat. Moreover, no structure in the A/E distributions is found, the double structure of GD32C and GD35C has vanished.

The pulse shape discrimination efficiencies of the enriched BEGe diodes operated with passivation in the GERDA LAr cryostat is on average about 45.4 % in the ROI at 2039 keV. In the case of GD32B the discrimination efficiency is significantly worse compared to the PSD efficiencies obtained in vacuum cryostat.

The comparison of different ^{228}Th calibrations shows that the A/E peaks shift slightly in between calibrations. The shift does not correlate with the drift of the A/E of the test pulse.

Finally, the pulse shape cut was applied to the GERDA physics data taken in Run 35. Six events are observed in an 800 keV window around the $Q_{\beta\beta}$ value of ^{76}Ge, 2039 keV. All events but one are rejected by the A/E cut. This demonstrates the capability of the A/E analysis to reject background events, especially for possible p^+ and n^+ events.

However, to reach a more effective suppression of β particles from ^{42}K and especially of γ-rays, the pulse shape performance of the BEGe detectors needs to be improved. The shift of A/E in time as well as the electronics broaden the A/E distributions. For a better pulse shape performance that is capable of rejecting events closer to the SSE line, a sharper A/E distribution is needed as well as sufficient statistics in the DEP by performing longer calibration runs or using stronger ^{228}Th sources.

The preliminary background index obtained for the four enriched BEGe detectors in Run 35, improves from

$$BI = (2.000 - 10.358) \cdot 10^{-2} \frac{counts}{kg \cdot yr \cdot keV} \quad \text{to}$$

$$BI^{PSA} = (0.089 - 3.544) \cdot 10^{-2} \frac{counts}{kg \cdot yr \cdot keV} \quad .$$

The preliminary background index with applied PSA cut is compatible with the design value of Phase II, $10^{-3} \frac{counts}{kg \cdot year \cdot keV}$. However, the background index is expected to decrease with increasing statistics and a smaller energy window.

Finally, results from measurements with enriched BEGe detectors in GDL give hints that the pulse shape performance in LAr can be even improved after removal of the passivation layer.

Chapter 4

Conclusions

In this diploma thesis the properties of the new GERDA Phase II diodes including their pulse shape performance was shown. Within the characterization campaign at HADES underground laboratory , the pulse shape discrimination efficiency of the new enriched BEGe diodes operated in vacuum cryostat was determined. It was shown that the pulse shape analysis based on the A/E parameter as developed in [Bud09] is a successful method for active background suppression with the new Phase II detectors.

However, unexpected differences among the new enriched diodes in pulse shape performance were found. Only two out seven enriched BEGe detectors, GD32B and GD35B, showed pulse shape discrimination efficiencies comparable to the previously tested depleted prototype BEGe detectors. The discrimination efficiency in the single escape peak (SEP) was 5.4 % on average, in the ROI 32.2 % respectively, while the residual five enriched BEGe diodes showed an efficiency of 10.5 % in the SEP and 42.0 % in the region (2039±50) keV.

This deterioration could be related to broadened or multi-structured A/E distributions as two enriched detectors with worse PSD efficiencies showed a double structure in the A/E distribution of the DEP, whereas three enriched diodes had a significantly broader A/E distribution respectively. The five enriched BEGe diodes with deteriorated pulse shape performance showed a relative resolution in A/E of the DEP larger than 1 %, whereas the two enriched BEGe detectors with compatible PSA performance as the prototype detectors showed A/E resolutions below 1 % respectively.

Surface scans with a collimated ^{241}Am source confirmed that the deteriorated pulse shape performance is related to a larger position-dependence of the A/E value. In previous scans with depleted prototype BEGe diodes it was found that the A/E peak position in the 59.5 keV peak should not differ more than 1 % from the A/E position in the center of the diode. This result was confirmed by the two detectors with compatibly good PSA performance. The five BEGe diodes with deteriorated pulse shape performance showed a stronger position-dependence in the A/E value. A broadened A/E distribution might be a superposition of such position-dependent A/E values.

It was found that at least to some extend surface effects influence the pulse shape performance. The passivation layer of two detectors with deteriorated pulse shape performance, GD32D and GD232C, was renewed in a mechanical and chemical treatment of the surface. For GD32D a significant improvement in pulse shape performance was observed. The discrimination efficiency in the SEP improved from 14.2 % to 5.9 %.

However, the surface treatment was not successful for GD32C which showed a high leakage current after the procedure.

In further investigation of the pulse shape performance the passivation layer was removed for two detectors with deteriorated pulse shape performance, GD32A and GD35A, and tested in GDL in a LAr cryostat. It was observed that the pulse shape performance enhances without passivation layer: In the case of GD32A, the PSD efficiency in the SEP was $8.2\,\%$ without passivation layer compared to $12.1\,\%$ with passivation layer. In the ROI the PSD efficiency improved from $42.7\,\mathrm{keV}$ to $38.0\,\%$. For GD35A the uncertainties in the PSD efficiencies are high, but an improvement in pulse shape performance was observed as well, as the A/E resolution in the DEP improved from $2.2\,\%$ with passivation to $1.17\,\%$ without.

After the successful characterization, five of the seven enriched BEGe detectors were installed into the GERDA LAr cryostat. At this stage, the passivation layer was not removed, as the main goal was to check for contamination of the diodes. No surface contamination was found. The new Phase II detectors showed a good performance in GERDA with enhanced energy resolution compared to the coaxial detectors. The energy resolution of the BEGe detectors is on average $3.2\,\mathrm{keV}$ in the $2614\,\mathrm{keV}$ peak.

No big differences in pulse shape performance among the BEGe diodes was observed, i.e. all A/E distributions in the DEP showed a single peak. However, the A/E resolution with $1.7\,\%$ on average is poor in comparison to the resolution of prototype BEGe detectors operated in vacuum cryostat ($0.5\,\%$). The pulse shape discrimination efficiencies of the enriched BEGe diodes operated in GERDA was determined to about $45.4\,\%$ on average in the ROI at $2039\,\mathrm{keV}$. In the case of GD32B the discrimination efficiency is significantly worse compared to the PSD efficiencies obtained in vacuum cryostat.

Finally, the pulse shape cut was determined for the new enriched BEGe detectors and applied to GERDA physics data for the first time. A preliminary background index for a short time period in a $(2039 \pm 400)\,\mathrm{keV}$ window for four enriched BEGe detectors was deduced. The background index with usual quality cuts, muon-veto- cut and anti-coincidence-cut only improves from $BI = (2.000 - 10.358) \cdot 10^{-2} \frac{counts}{kg \cdot yr \cdot keV}$ to

$$BI^{PSA} = (0.089 - 3.544) \cdot 10^{-2} \frac{counts}{kg \cdot yr \cdot keV}$$

by applying the pulse shape cut.

Although, the statistics is low and the energy window is big an improvement of the background index is achieved by the A/E cut. The preliminary background index with applied pulse shape analysis is within the Phase II design value of $10^{-3} \frac{counts}{kg \cdot yr \cdot keV}$.

A further improvement in the background index is expected with increasing statistics in a smaller energy window. Moreover, the pulse shape performance is expected to enhance by the removal of the passivation layer prior to the start of Phase II.

The pulse shape performance of the enriched detectors proves that the A/E analysis is capable of rejecting background from multi-site γ-events as well as ^{42}K β-particles and ^{210}P α particles. The obtained results on pulse shape analysis are very promising that the Phase II design background index will be reached with the new enriched BEGe detectors and the LAr Compton veto.

^{228}Th Measurements for PSA

number	date	detector	life time	HV
1	09.02.2012	^{depl}Ge-9	4.0 h	4.5 kV
2	10.02.2012	^{depl}Ge-9	6.0 h	4.5 kV
3	**16.02.2012**	**GD35A**	**5.0 h**	**4.0 kV**
4	**17.02.2012**	**GD32C**	**5.0 h**	**4.0 kV**
5	22.02.2012	GD35A	3.0 h	4.0 kV
6	22.02.2012	GD32C	3.0 h	4.0 kV
7	23.02.2012	^{depl}DD	3.0 h	4.5 kV
8	23.02.2012	^{depl}Ge-9	2.8 h	4.5 kV
9	**23.02.2012**	^{depl}**Ge-9**	**6.0 h**	**4.5 kV**
10	24.02.2012	GD32A	3.0 h	3.0 kV
11	27.02.2012	GD32D	3.0 h	4.0 kV
12	28.02.2012	GD32C	3.0 h	4.0 kV
13	06.03.2012	GD35C	3.0 h	3.5 kV
14	**07.03.2012**	**GD35C**	**8.0 h**	**3.5 kV**
15	**08.03.2012**	**GD35B**	**8.0 h**	**4.0 kV**
16	**09.03.2012**	**GD32B**	**7.0 h**	**4.0 kV**
17	14.03.2012	GD35B	3.0 h	4.0 kV
18	14.03.2012	GD32D	12.0 h	3.0 kV
19	14.03.2012	GD32D	2.8 h	4.0 kV
20	15.03.2012	GD32D	1.9 h	3.5 kV
21	**15.03.2012**	**GD32D**	**2.7 h**	**4.0 kV**
22	15.03.2012	GD32D	2.7 h	4.5 kV
23	**26.03.2012**	**GD32A**	**14.0 h**	**3.0 kV**
24	29.03.2012	GD32C	3.0 h	4.0 kV

Table A.1: Part of ^{228}Th measurements performed in HADES. The main measurements used for the calculation of PSD efficiency are printed in bold type. Ge-9 and DD are produced of germanium crystals which are depleted in ^{76}Ge whereas all others are isotopically enriched in ^{76}Ge at a 86 % level. All measurements were performed at the high voltage recommended by the manufacturer Canberra, except for measurements no. 18, 20 and 22.

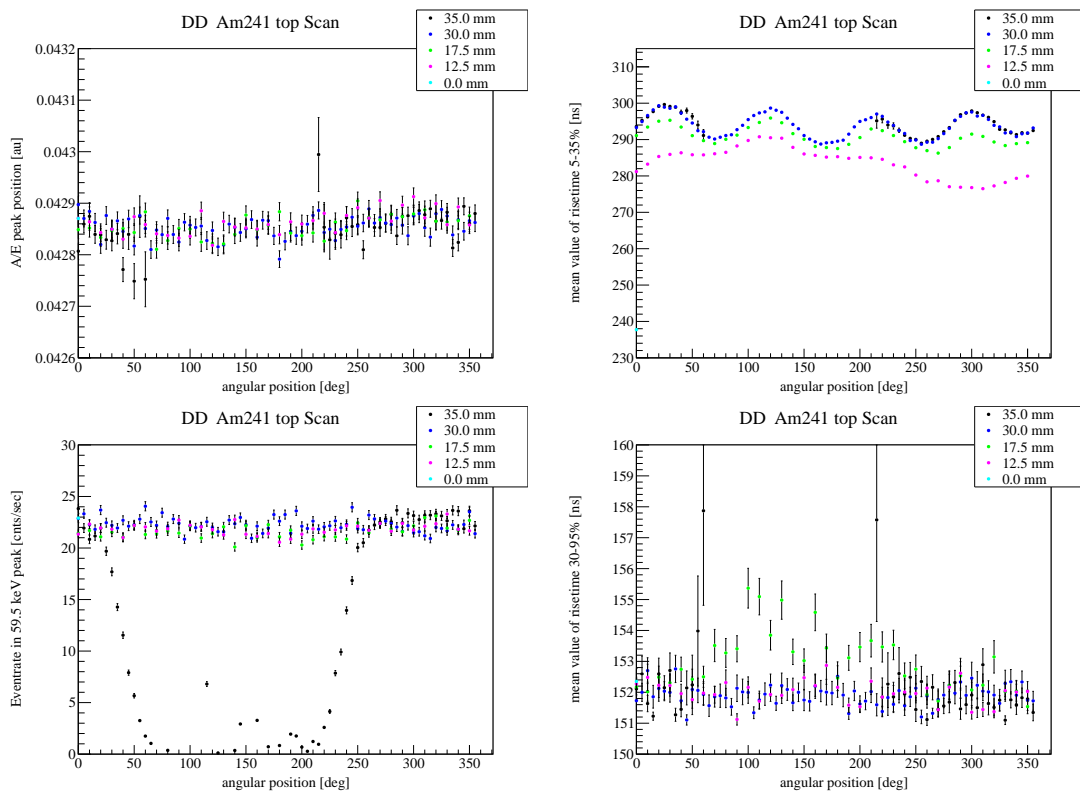# Appendix B

Results from Detailed ^{241}Am Surface Scans

Figure B.1: Results from detailed ^{241} Am Scans for ^{depl}DD BEGe detector. The active diameter of the crystal is $74\,\text{mm}$
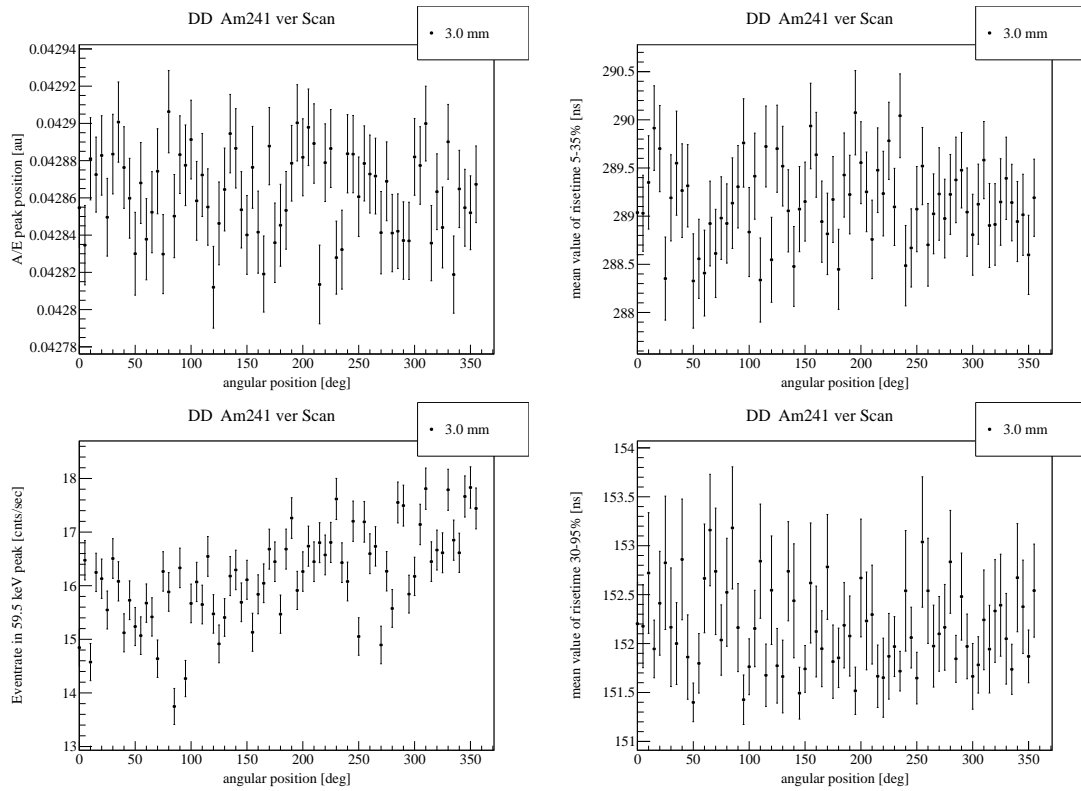
Figure B.2: Results from detailed ^{241}Am Scans for ^{depl}DD BEGe detector. The diode is 32 mm thick.
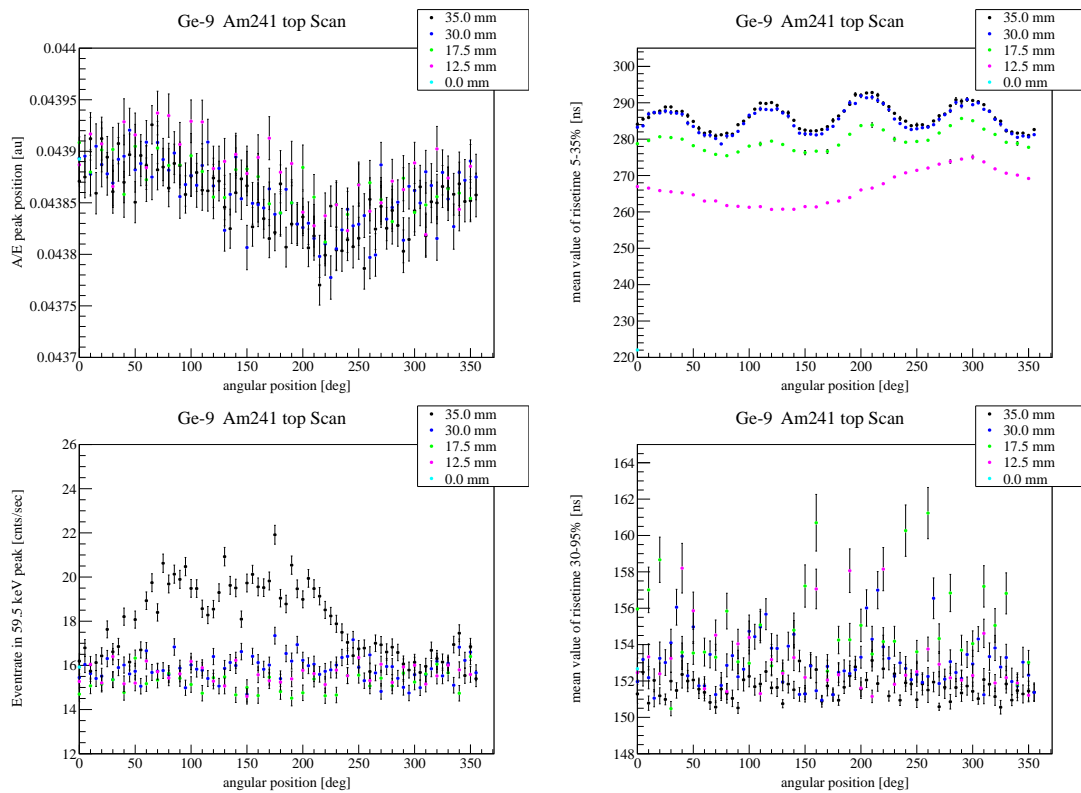
Figure B.3: Results from detailed ^{241}Am Scans for ^{depl}Ge-9 BEGe detector. The active diameter of the crystal is 75.4 mm.

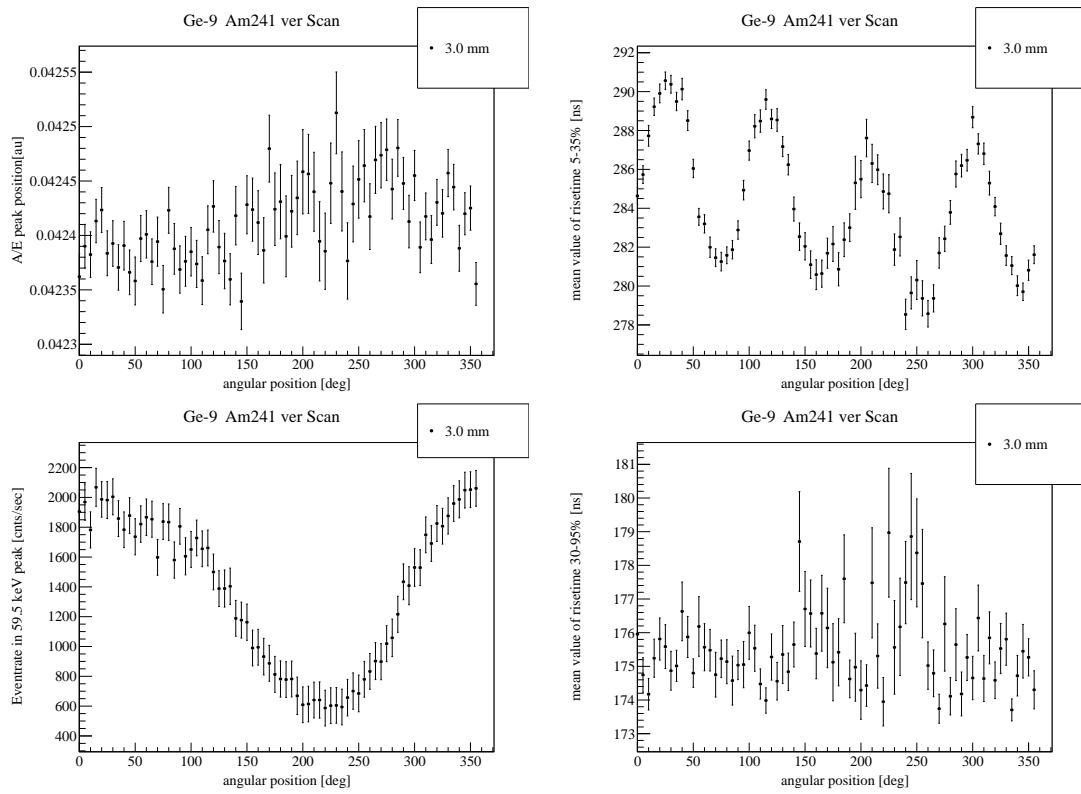**Figure B.4:** Results from detailed ^{241}Am Scans for ^{depl}Ge-9 BEGe detector. The diode is 31 mm thick.

Figure B.5: Results from detailed ^{241}Am Scans for GD32B. The active diameter of the crystal is 71.8 mm.
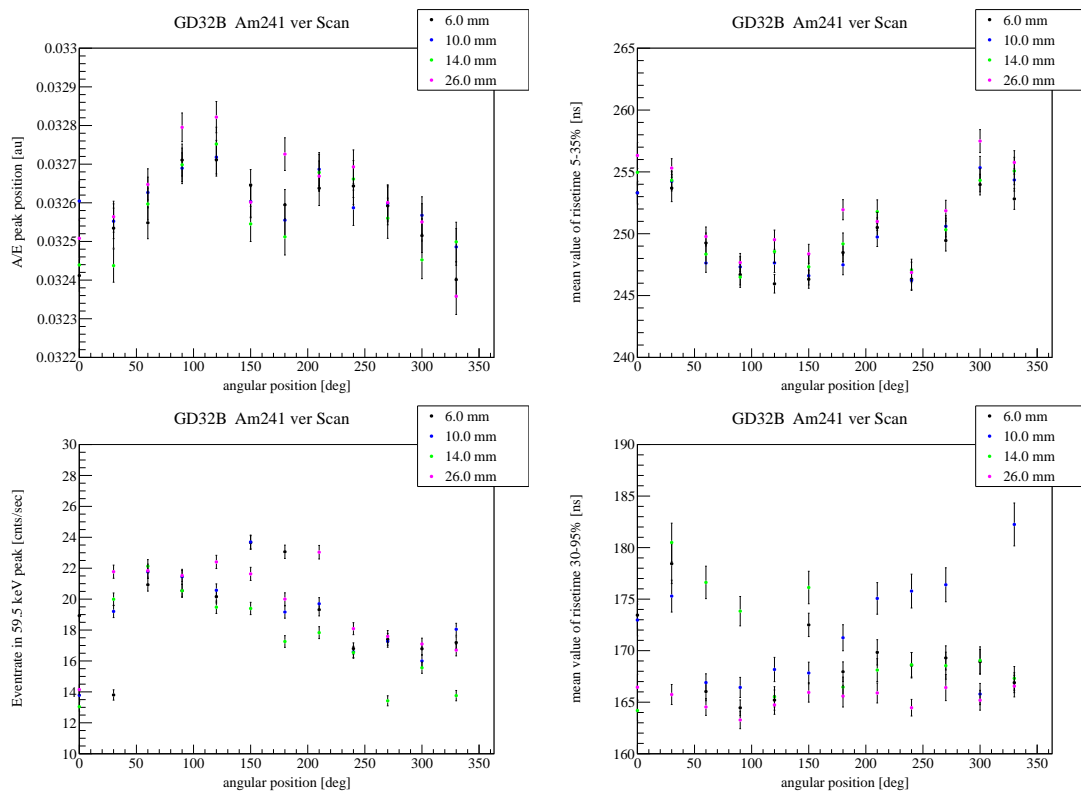
Figure B.6: Results from detailed ^{241}Am Scans for Ge-9. The diode is 32.2 mm thick.
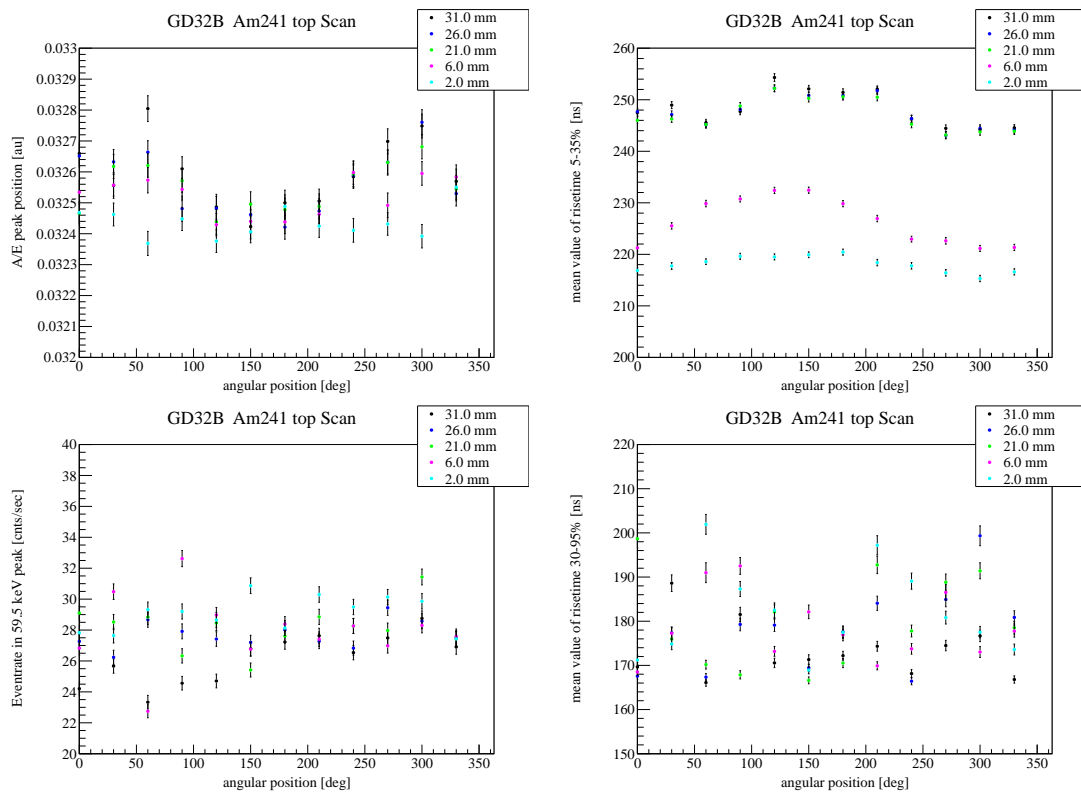
Figure B.7: Results from detailed ^{241}Am Scans for GD32C. The active diameter of the crystal is 72 mm.

Figure B.8: Results from detailed ^{241}Am Scans for GD32D. The active diameter of the crystal is 72.2 mm.

Figure B.9: Results from detailed ^{241}Am Scans for GD32D. The diode is 32 mm thick.
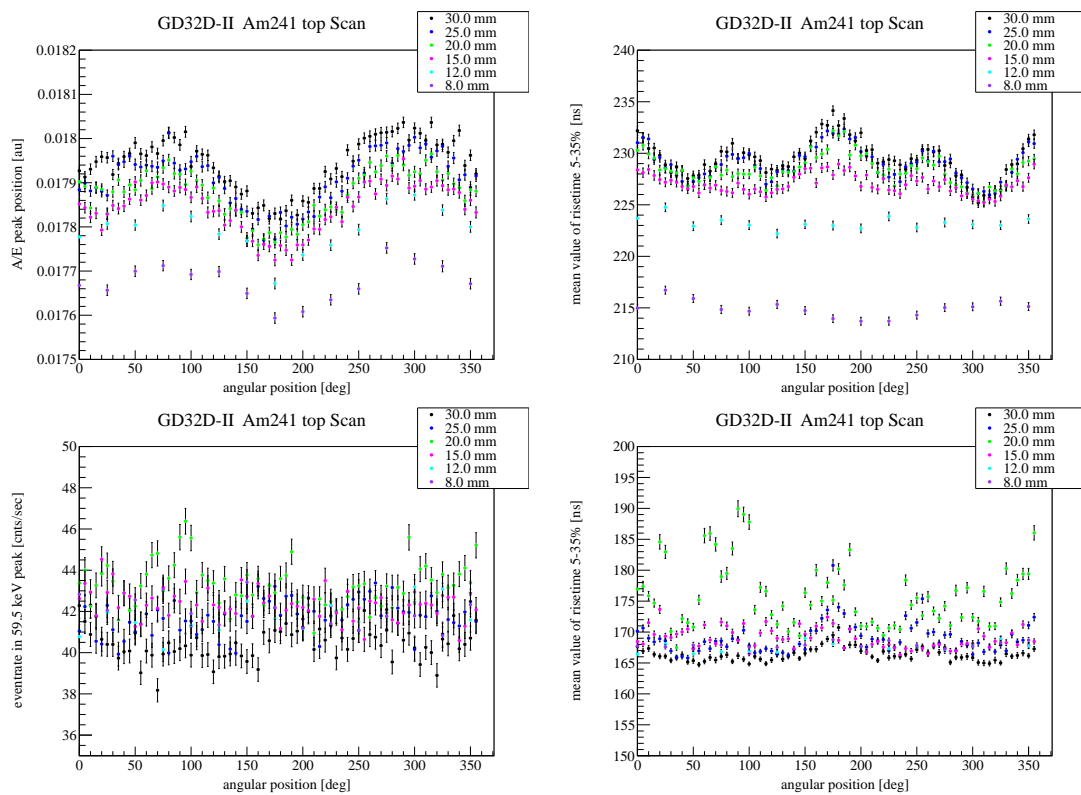
Figure B.10: Results from detailed ^{241}Am Scans for GD32D II (after reprocessing). The active diameter of the crystal is 72.2 mm.

Figure B.11: Results from detailed ^{241}Am Scans for GD32D II (after reprocessing). The diode is 32 mm thick.
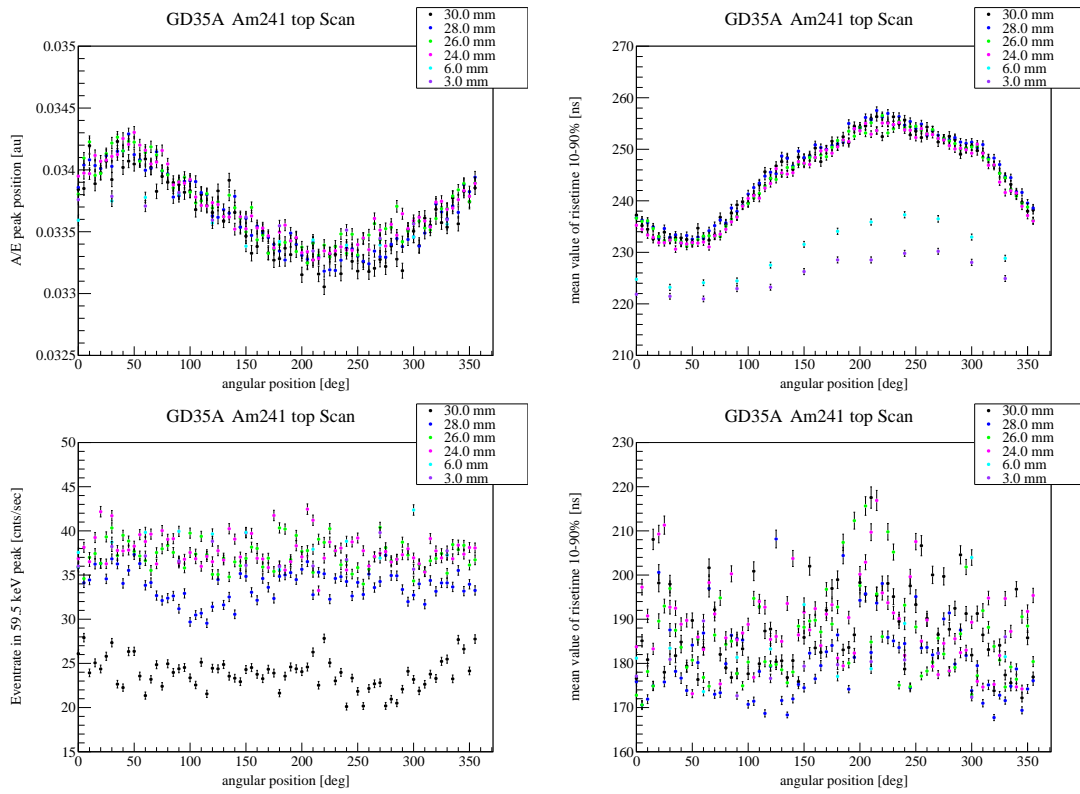
Figure B.12: Results from detailed ^{241}Am Scans for GD35A. The active diameter of the crystal is 73.6 mm,.

Figure B.13: Results from detailed ^{241}Am Scans for GD35A. The diode is 35.3 mm thick.
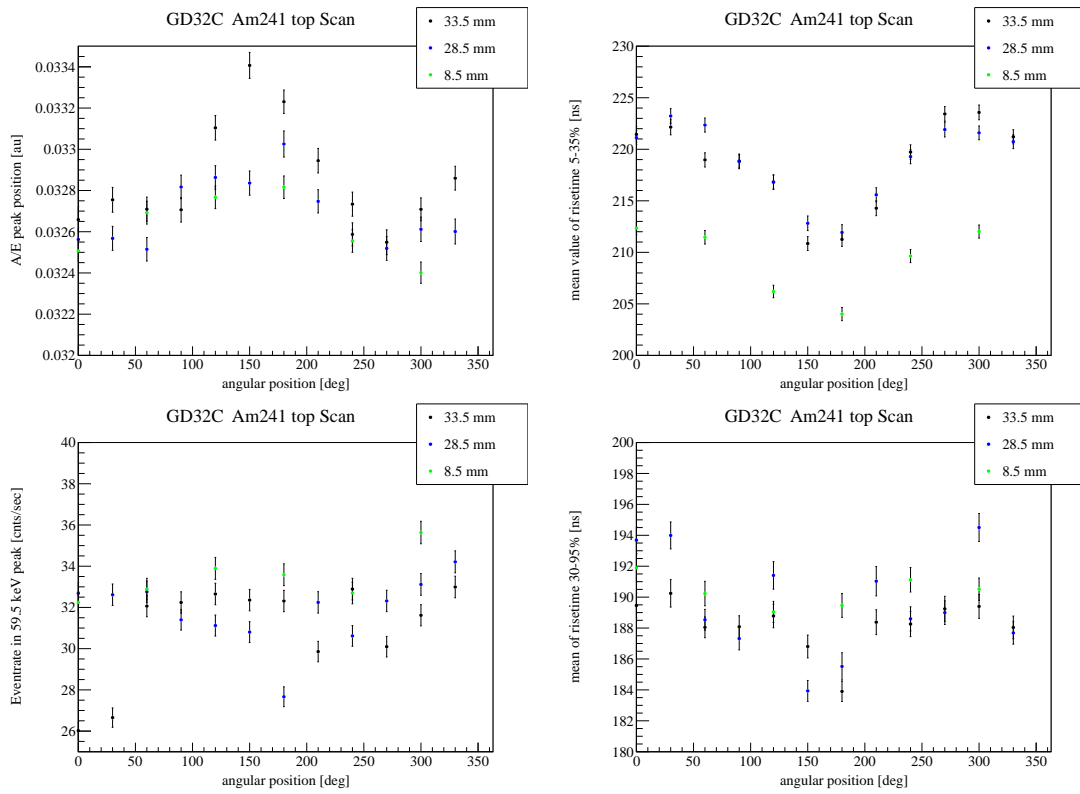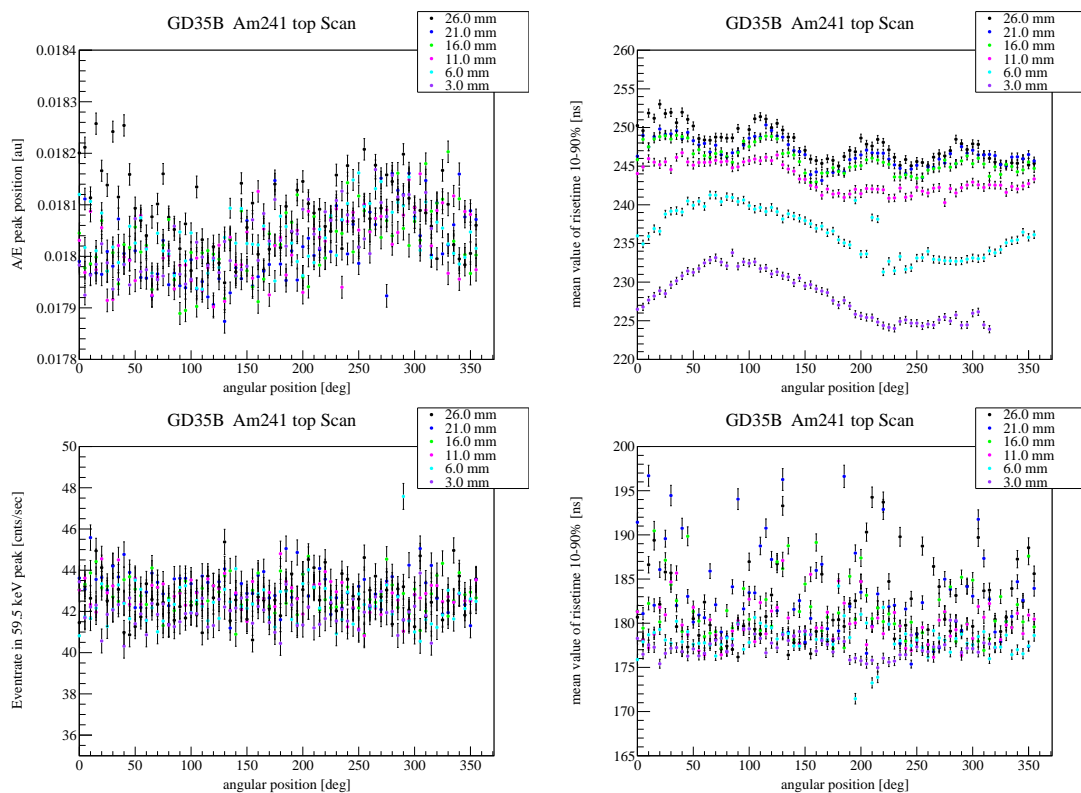
Figure B.14: Results from detailed ^{241}Am Scans for GD35B. The active diameter of the crystal is 76.6 mm.

Figure B.15: Results from detailed ^{241}Am Scans for GD35B. The diode is 32 mm thick.
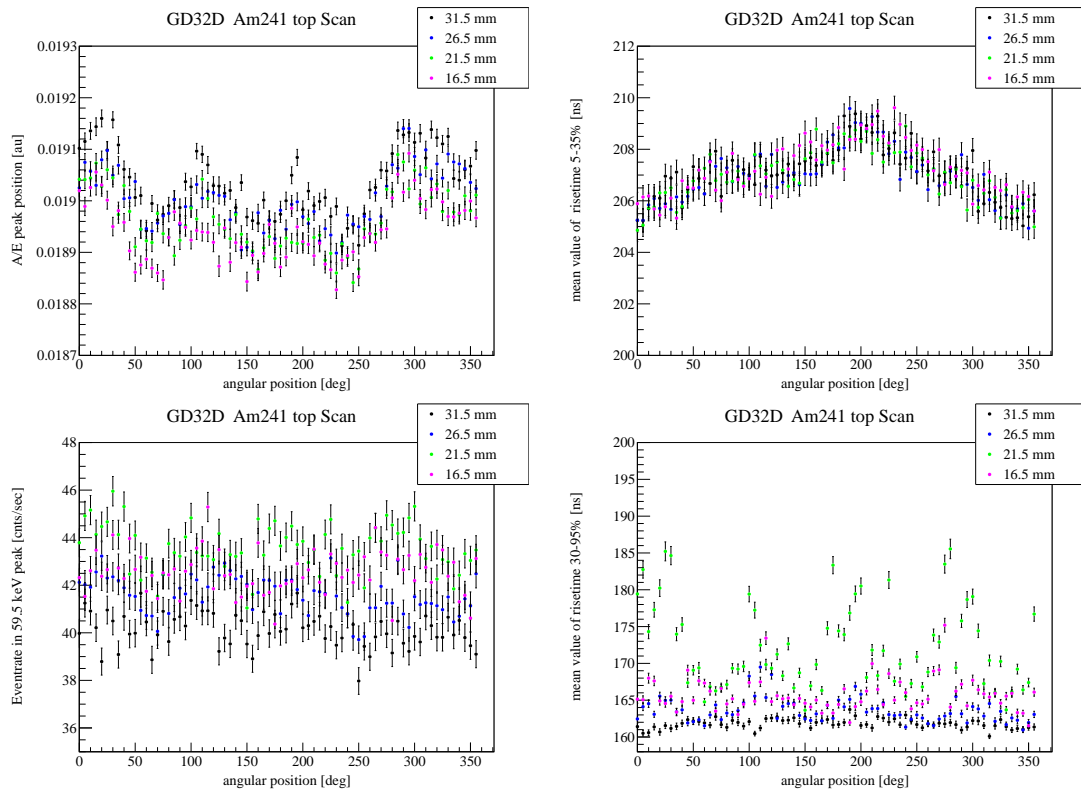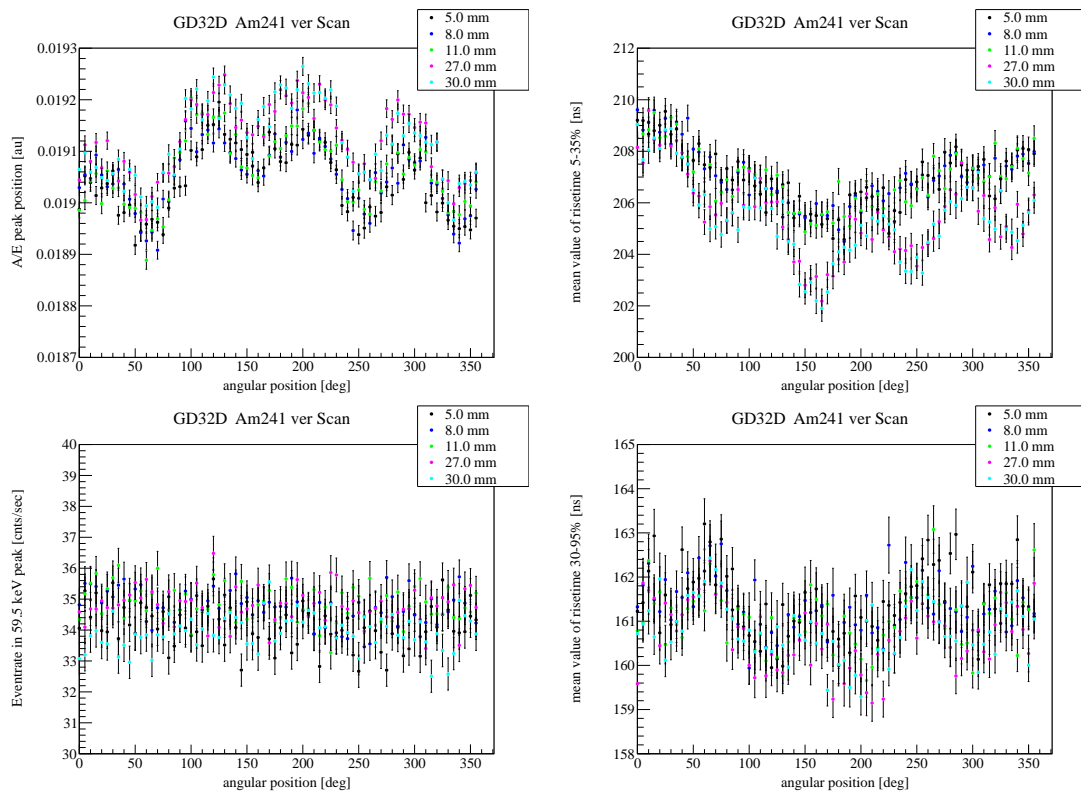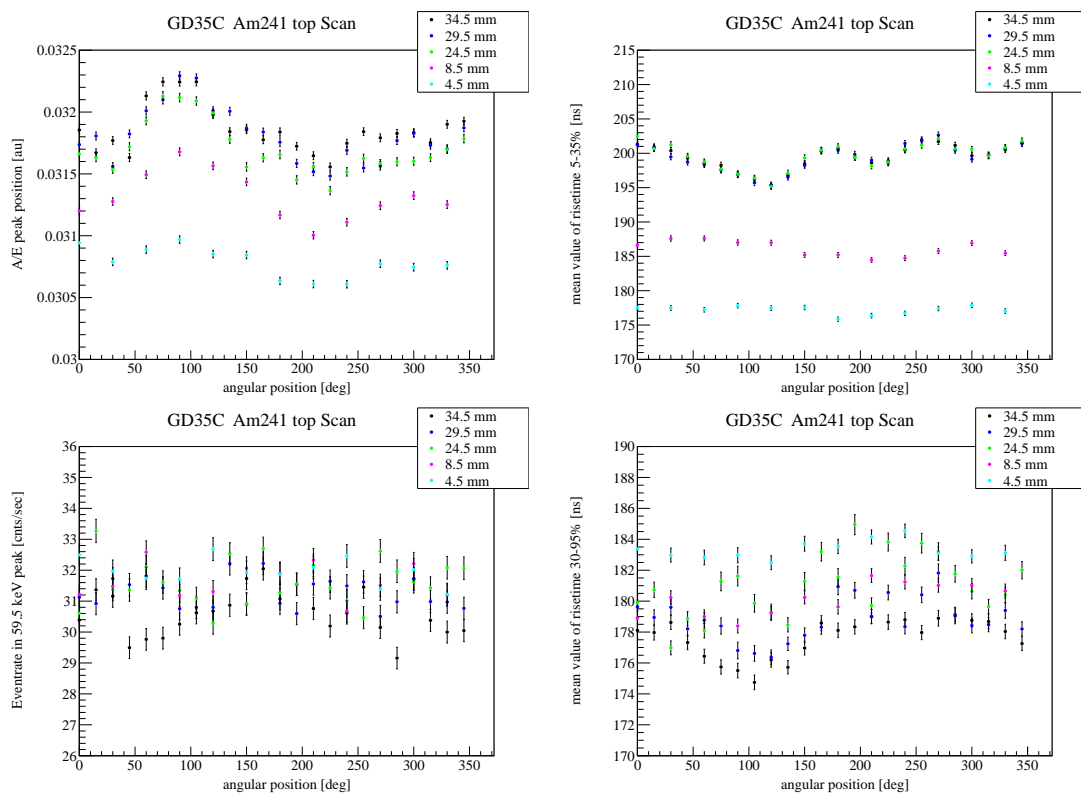
Figure B.16: Results from detailed ^{241}Am Scans for GD35C. The active diameter of the crystal is 74.8 mm.

Figure B.17: Results from detailed ^{241}Am Scans for GD35C. The diode is 26.4 mm thick.

Appendix C

Development of A/E Distribution in Time for GERDA Run 35

Detector	A/E peak position			
	Calibration 1+2	Calibration 3	Calibration 4	Calibration 5
GD32B	0.05178	0.05088	0.05119	0.05092
GD32C	0.05254	0.05220	0.05229	0.05213
GD32D	0.05768	0.05741	0.05738	0.05725
GD35B	0.05322	0.05294	0.05290	0.05273
GD35C	0.05465	0.05480	0.05470	0.05445

Table C.1: Comparison of A/E positions for all Calibrations. Calibration 1 and 2 are combined. A/E peak position was estimated by a Gaussian. Uncertainties from fitting are negligible.

Detector	Difference of A/E peak position in sigma compared to:			
	Calibration 3	Calibration 4	Calibration 5	
GD32B	2.676 ± 0.036	1.755 ± 0.024	2.571 ± 0.035	Calibration 1 + 2
GD32C	0.886 ± 0.011	0.660 ± 0.009	1.084 ± 0.014	
GD32D	0.682 ± 0.013	0.747 ± 0.014	1.071 ± 0.021	
GD35B	0.646 ± 0.011	0.738 ± 0.013	1.135 ± 0.019	
GD35C	−0.396 ± 0.008	−0,145 ± 0.003	0.499 ± 0.011	
GD32B		−0.851 ± 0.028	−0.097 ± 0.003	Calibration 3
GD32C		−0.225 ± 0.009	0.198 ± 0.007	
GD32D		0.063 ± 0.002	0.377 ± 0.011	
GD35B		0.081 ± 0.001	0.434 ± 0.007	
GD35C		0.242 ± 0.006	0.864 ± 0.021	
GD32B			0.773 ± 0.029	Calibration 4
GD32C			0.444 ± 0.015	
GD32D			0.298 ± 0.011	
GD35B			0.391 ± 0.008	
GD35C			0.600 ± 0.015	

Table C.2: Deviation of A/E peak position in sigma for different calibrations. A/E peak position and sigma were estimated by a Gaussian. Calibration 1 and 2 were combined.

Appendix D

Datasheets

DETECTOR SPECIFICATION AND PERFORMANCE DATA

Specifications

Detector Model   <u>BE3830/S</u>   **Serial number**   <u>b 11123</u>
Cryostat Model   <u>7500SL</u>
Preamplifier Model   <u>2002CSL</u>

The purchase specifications and therefore the warranted performance of this detector are as follows :

Energy	5.9 keV	122 keV	1332.5 keV
Resolution eV(FWHM)			

Cryostat description or Drawing Number if special   <u>7500SL</u>

Physical Characteristics

Active Diameter	75.4	mm	Distance from window (outside)	<u>6</u>	mm
Active Area	<u>4465</u>	mm^2	Window thickness	<u>1.5</u>	mm
Thickness	31	mm	Window material	<u>AL</u>	

Electrical Characteristics

Depletion voltage   <u>(+)4000</u>   Vdc
Recommended bias voltage Vdc   <u>(+)4500</u>   Vdc
Reset rate at recommended bias   <u>/</u>   sec (PO preamp only)
Preamplifier test point voltage at recommended bias <u>-0.1</u>   Vdc (RC preamp only)

Resolution and Efficiency

With amp time constant of   <u>4</u>   μs

Isotope		^{57}Co	^{60}Co	
Energy (keV)		122	1332.5	
FWHM (eV)		648	1745	
FWTM (eV)			3211	

- Tests are performed following IEEE standard test ANSI/IEEE std325-1996

- Standard Canberra electronics used - See Germanium detector manual Section 7

Tested by :   Date : <u>April 28, 2011</u>

Approved by :   Date : <u>April 28, 2011</u>

Figure D.1: Datasheet of depleted BEGe detector Ge-9

A
CANBERRA

DETECTOR SPECIFICATION AND PERFORMANCE DATA

Specifications

Detector Model   BE5030/S   **Serial number** b 11039
Cryostat Model   7500SL
Preamplifier Model 2002CSL

The purchase specifications and therefore the warranted performance of this detector are as follows :

Energy	5.9 keV	122 keV	1332.5 keV
Resolution eV(FWHM)			

Cryostat description or Drawing Number if special 7500SL

Physical Characteristics

Active Diameter	74	mm	Distance from window (outside)	6	mm
Active Area	4300	mm²	Window thickness	1.5	mm
Thickness	32	mm	Window material	AL	

Electrical Characteristics

Depletion voltage   (+)4000   Vdc
Recommended bias voltage Vdc   (+)4500 Vdc
Reset rate at recommended bias   /   sec (PO preamp only)
Preamplifier test point voltage at recommended bias -0.1   Vdc (RC preamp only)

Resolution and Efficiency

With amp time constant of   4   μs

Isotope		⁵⁷Co	⁶⁰Co	
Energy (keV)		122	1332.5	
FWHM (eV)		556	1712	
FWTM (eV)		1017	3218	

- Tests are performed following IEEE standard test ANSI/IEEE std325-1996
- Standard Canberra electronics used - See Germanium detector manual Section 7
- Li thickness – 0.45mm

Tested by :   Date : March 24, 2010

Approved by :   Date : March 24, 2010

GDAME003/F   *12/03/2007*   *1/1*

Figure D.2: Datasheet of depleted BEGe detector DD

ARCHIMEDES

△ CANBERRA

DETECTOR SPECIFICATION AND PERFORMANCE DATA

Specifications

Detector Model   BE3830/S   Serial number b 13014 (P2432AA)
Cryostat Model   7500SL
Preamplifier Model 2002CSL

The purchase specifications and therefore the warranted performance of this detector are as follows :

Energy	5.9 keV	122 keV	1332.5 keV
Resolution eV(FWHM)			

Cryostat description or Drawing Number if special   7500SL

Physical Characteristics

Active Diameter	66.2	mm	Distance from window (outside)	6.5	mm
Active Area	3318	mm^2	Window thickness	1.5	mm
Thickness	25	mm	Window material	AL	

Electrical Characteristics

Depletion voltage   (+)2500   Vdc
Recommended bias voltage Vdc   (+)3000   Vdc
Reset rate at recommended bias   /   sec (PO preamp only)
Preamplifier test point voltage at recommended bias -1.0   Vdc (RC preamp only)

Resolution and Efficiency

With amp time constant of   4   µs

Isotope	^{55}Fe	^{57}Co	^{60}Co	
Energy (keV)	5.9	122	1332.5	
FWHM (eV)		632	1695	
FWTM (eV)		1162	3124	

- Tests are performed following IEEE standard test ANSI/IEEE std325-1996
- Standard Canberra electronics used - See Germanium detector manual Section 7

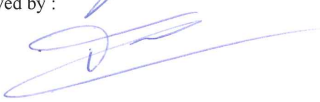Tested by :   Date : February 15, 2012

Approved by :   Date : February 15, 2012

GDAME003/F   *12/03/2007*   *1/1*

Figure D.3: Datasheet of enriched BEGe detector GD32A

AGAMENNONE

A CANBERRA

DETECTOR SPECIFICATION AND PERFORMANCE DATA

Specifications

Detector Model   BE3830/S   **Serial number** b 13015 (P2432BB)
Cryostat Model   7500SL
Preamplifier Model 2002CSL

The purchase specifications and therefore the warranted performance of this detector are as follows :

Energy	5.9 keV	122 keV	1332.5 keV
Resolution eV(FWHM)			

Cryostat description or Drawing Number if special 7500SL

Physical Characteristics

Active Diameter	71.8	mm	Distance from window (outside)	6.5	mm
Active Area	3857	mm^2	Window thickness	1.5	mm
Thickness	32.2	mm	Window material	AL	

Electrical Characteristics

Depletion voltage   (+)3500   Vdc
Recommended bias voltage Vdc   (+)4000 Vdc
Reset rate at recommended bias   /   sec (PO preamp only)
Preamplifier test point voltage at recommended bias -0.9   Vdc (RC preamp only)

Resolution and Efficiency

With amp time constant of   4   μs

Isotope	^{55}Fe	^{57}Co	^{60}Co	
Energy (keV)	5.9	122	1332.5	
FWHM (eV)		654	1747	
FWTM (eV)		1206	3266	

- Tests are performed following IEEE standard test ANSI/IEEE std325-1996
- Standard Canberra electronics used - See Germanium detector manual Section 7

Tested by :   Date : February 17, 2012

Approved by :   Date : February 17, 2012

Figure D.4: Datasheet of enriched BEGe detector GD32B

ANDROMEDA

CANBERRA

DETECTOR SPECIFICATION AND PERFORMANCE DATA

Specifications

Detector Model   BE3830/S   **Serial number** b 13020 (P2432CC)
Cryostat Model   7500SL
Preamplifier Model   2002CSL

The purchase specifications and therefore the warranted performance of this detector are as follows :

Energy	5.9 keV	122 keV	1332.5 keV
Resolution eV(FWHM)			

Cryostat description or Drawing Number if special   7500SL

Physical Characteristics

Active Diameter	72	mm	Distance from window (outside)	6.5	mm
Active Area	3914	mm^2	Window thickness	1.5	mm
Thickness	33.2	mm	Window material	Al	

Electrical Characteristics

Depletion voltage   (+)3500   Vdc
Recommended bias voltage Vdc   (+)4000   Vdc
Reset rate at recommended bias   /   sec (PO preamp only)
Preamplifier test point voltage at recommended bias -0.6   Vdc (RC preamp only)

Resolution and Efficiency

With amp time constant of   4   μs

Isotope	^{55}Fe	^{57}Co	^{60}Co	
Energy (keV)	5.9	122	1332.5	
FWHM (eV)		596	1658	
FWTM (eV)		1097	3117	

- Tests are performed following IEEE standard test ANSI/IEEE std325-1996
- Standard Canberra electronics used - See Germanium detector manual Section 7

Tested by :   Date : February 14, 2012

Approved by :   Date : February 14, 2012

GDAME003/F   12/03/2007   1/1

Figure D.5: Datasheet of enriched BEGe detector GD32C

ANUBIS

CANBERRA

DETECTOR SPECIFICATION AND PERFORMANCE DATA

Specifications

Detector Model   BE3830/S   **Serial number** b 13018 (P2432DD)
Cryostat Model   7500SL
Preamplifier Model 2002CSL

The purchase specifications and therefore the warranted performance of this detector are as follows :

Energy	5.9 keV	122 keV	1332.5 keV
Resolution eV(FWHM)			

Cryostat description or Drawing Number if special   7500SL

Physical Characteristics

Active Diameter	72.2	mm	Distance from window (outside)	6.5	mm
Active Area	3935	mm^2	Window thickness	1.5	mm
Thickness	32	mm	Window material	AL	

Electrical Characteristics

Depletion voltage   (+)3500   Vdc
Recommended bias voltage Vdc   (+)4000   Vdc
Reset rate at recommended bias   /   sec (PO preamp only)
Preamplifier test point voltage at recommended bias   - 0.6   Vdc (RC preamp only)

Resolution and Efficiency

With amp time constant of   4   µs

Isotope	^{55}Fe	^{57}Co	^{60}Co	
Energy (keV)	5.9	122	1332.5	
FWHM (eV)		639	1757	
FWTM (eV)		1172	3213	

- Tests are performed following IEEE standard test ANSI/IEEE std325-1996
- Standard Canberra electronics used - See Germanium detector manual Section 7

Tested by :   Date : February 15, 2012

Approved by :   Date : February 15, 2012

Figure D.6: Datasheet of enriched BEGe detector GD32D

ARGO

A CANBERRA

DETECTOR SPECIFICATION AND PERFORMANCE DATA

Specifications

Detector Model   BE3830/S
Cryostat Model   7500SL
Preamplifier Model 2002CSL

Serial number b 13019 (P2435AA)

The purchase specifications and therefore the warranted performance of this detector are as follows :

Energy	5.9 keV	122 keV	1332.5 keV
Resolution eV(FWHM)			

Cryostat description or Drawing Number if special   7500SL

Physical Characteristics

Active Diameter	73.6	mm	Distance from window (outside)	6.5	mm
Active Area	4094	mm^2	Window thickness	1.5	mm
Thickness	35.3	mm	Window material	Al	

Electrical Characteristics

Depletion voltage   (+)3000   Vdc
Recommended bias voltage Vdc   (+)4000   Vdc
Reset rate at recommended bias   /   sec (PO preamp only)
Preamplifier test point voltage at recommended bias -0.5   Vdc (RC preamp only)

Resolution and Efficiency

With amp time constant of   4   μs

Isotope	^{55}Fe	^{57}Co	^{60}Co	
Energy (keV)	5.9	122	1332.5	
FWHM (eV)		607	1785	
FWTM (eV)		1131	3279	

- Tests are performed following IEEE standard test ANSI/IEEE std325-1996
- Standard Canberra electronics used - See Germanium detector manual Section 7

Tested by :   Date : February 14, 2012

Approved by :   Date : February 14, 2012

GDAME003/F   12/03/2007   1/1

Figure D.7: Datasheet of enriched BEGe detector GD35A

ACHILLES

DETECTOR SPECIFICATION AND PERFORMANCE DATA

Specifications

Detector Model   BE3830/S   **Serial number**   b 13017 (P2435BB)
Cryostat Model   7500SL
Preamplifier Model   2002CSL

The purchase specifications and therefore the warranted performance of this detector are as follows :

Energy	5.9 keV	122 keV	1332.5 keV
Resolution eV(FWHM)			

Cryostat description or Drawing Number if special   7500SL

Physical Characteristics

Active Diameter	76.6	mm	Distance from window (outside)	6.5	mm
Active Area	4441	mm^2	Window thickness	1.5	mm
Thickness	32	mm	Window material	Al	

Electrical Characteristics

Depletion voltage   (+)3500   Vdc
Recommended bias voltage Vdc   (+)4000   Vdc
Reset rate at recommended bias   /   sec (PO preamp only)
Preamplifier test point voltage at recommended bias -0.8   Vdc (RC preamp only)

Resolution and Efficiency

With amp time constant of   4   μs

Isotope	^{55}Fe	^{57}Co	^{60}Co	
Energy (keV)	5.9	122	1332.5	
FWHM (eV)		642	1748	
FWTM (eV)		1181	3260	

- Tests are performed following IEEE standard test ANSI/IEEE std325-1996
- Standard Canberra electronics used - See Germanium detector manual Section 7

Tested by :   Date : February 16, 2012

Approved by :   Date : February 16, 2012

Figure D.8: Datasheet of enriched BEGe detector GD35B

ARISTOTELES

A CANBERRA

DETECTOR SPECIFICATION AND PERFORMANCE DATA

Specifications

Detector Model   BE3830/S   **Serial number**   b 13016 (P2435CC)
Cryostat Model   7500SL
Preamplifier Model   2002CSL

The purchase specifications and therefore the warranted performance of this detector are as follows :

Energy	5.9 keV	122 keV	1332.5 keV
Resolution eV(FWHM)			

Cryostat description or Drawing Number if special   7500SL

Physical Characteristics

Active Diameter	74.8	mm	Distance from window (outside)	6.5	mm
Active Area	4254	mm^2	Window thickness	1.5	mm
Thickness	26.4	mm	Window material	Al	

Electrical Characteristics

Depletion voltage   (+)3000   Vdc
Recommended bias voltage Vdc   (+)3500   Vdc
Reset rate at recommended bias   /   sec (PO preamp only)
Preamplifier test point voltage at recommended bias -0.4   Vdc (RC preamp only)

Resolution and Efficiency

With amp time constant of   4   μs

Isotope	^{55}Fe	^{57}Co	^{60}Co	
Energy (keV)	5.9	122	1332.5	
FWHM (eV)		618	1643	
FWTM (eV)		1137	3031	

- Tests are performed following IEEE standard test ANSI/IEEE std325-1996
- Standard Canberra electronics used - See Germanium detector manual Section 7

Tested by :   Date : February 16, 2012

Approved by :   Date : February 16, 2012

GDAME003/F	*12/03/2007*	*1/1*

Figure D.9: Datasheet of enriched BEGe detector GD35C

Appendix E

Lists

E.1 List of Figures

E.2 List of Tables

Appendix F

Bibliography

[Aea02a] C. E. Aalseth et al. Comment on "evidence for neutrinoless double beta decay". *Mod. Phys. Lett. A*, 17:1475–1478, 2002.

[Aea02b] C. E. Aalseth et al. The igex ge-76 neutrinoless double-beta decay experiment: Prospects for next generation experiments. *Phys. Rev. D*, 65:092007, 2002.

[Aea10] I. Abt et al. Pulse shape simulations for segmented true-coaxial hpge detector. *Eur. Phys. J. C*, 68:609–618, 2010.

[Aea11a] M. Agostini et al. Gelatio: a general framework for mudular digital analysis of high purity ge detector signals. *JINST 6 P08013*, 2011.

[Aea11b] M. Agostini et al. Signal modeling of high-purity germanium detectors with a small read-out electrode and application to neutrinoless double beta decay search in ge-76. *JINST 6 P03005*, 2011.

[And12] E. Andreotti. Characterization of bege detectors in the hades underground laboratory in view of their application to neutrinoless double beta decay searches. 2012.

[Bar11] A.S. Barabash. *Phys. Atom. Nucl*, 74:603, 2011.

[Bea00] L. Baudis et al. Genius-tf: a test facility for the genius project. *arXiv:hep-ex/0012022*, 2000.

[Bea12] J. Beringer et al.(PDG). 36. statistics. *PR D86*, page 010001, 2012.

[Bud09] D. Budjas. Germanium detector studies in the framework of the gerda experiment. *Dissertation, Universtity of Heidelberg*, 2009.

[Bud12a] D. Budjas. private communication, 2012.

[Bud12b] D. Budjas. Active background suppression in gerda phase ii. 2012.

[Col04] The GERDA Collaboration. Letter of intent. *arXiv:hep-ex/0404039*, 2004.

[Gar12] A. Garfagnini. 241am scanning table overview and status. `http://www.mpi-hd.mpg.de/gerdawiki/index.php/Agenda`, 2012.

[He01]   Zhong He. Review of the shockley-ramo theorem and its application in semiconductor gamma-ray detectors. *Instruments and Methods in Physics Research A*, 463:250–267, 2001.

[Hea10]   M. Barnabe Heider et al. Operation and performance of bare broad-energy germanium detectors in liquid argon. *JINST 5 P10007*, 2010.

[Hei09]   M. B. Heider. *Performance and stability tests of bare high purity germanium detectors in liquid argon for the GERDA experiment.* PhD thesis, University of Heidelberg, 2009.

[Inc12]   Canberra Industry Inc. High-purity germanium (hpge) detectors. `http://www.canberra.com/products/detectors/germanium-detectors.asp`, 2012.

[KKea01]   H.V. Klapdor-Kleingrothaus et al. Latest results from the heidelberg-moscow double beta decay experiment. *Euro. Phys. J. A*, 12:147–154, 2001.

[KKea04]   H.V. Klapdor-Kleingrothaus et al. Data acquisition and analysis of the 76ge double beta experiment in gran sasso 1990-2003. *Nucl. Instrum. Meth. A*, 522:371–406, 2004.

[Kno89]   Glenn F. Knoll. *Radiation Detection and Measurements.* Wiley, New York, 1989.

[Rod11]   Werner Rodejohann. Neutrinoless double beta decay and particle physics. *Int.J.Mod.Phys. E*, 20:1833–1930, arXiv:1106.1334 [hep–ph], 2011.

[Sal12]   M. Salathe. The transition layer in a bege detector. private communication, 2012.

Acknowledgments

Erklärung:

Ich versichere, dass ich diese Arbeit selbstständig verfasst habe und keine anderen als die angegebenen Quellen und Hilfsmittel benutzt habe.

Heidelberg, den (Datum)   . . . .